Title
Characteristics and Applications of Thin Liquid Films Flowing Down High-Curvature Surfaces

Author
Sadeghpour, Abolfazl

Publication Date
2020

Peer reviewed|Thesis/dissertation

UNIVERSITY OF CALIFORNIA

Los Angeles

Characteristics and Applications of Thin Liquid Films Flowing Down High-Curvature Surfaces

A dissertation submitted in partial satisfaction

of the requirements for the degree

Doctor of Philosophy in Mechanical Engineering

by

Abolfazl Sadeghpour

2020

ABSTRACT OF THE DISSERTATION

Characteristics and Applications of Thin Liquid Films

Flowing Down High-Curvature Surfaces

by

Abolfazl Sadeghpour

Doctor of Philosophy in Mechanical Engineering

University of California, Los Angeles, 2020

Professor Yongho Ju, Chair

Thin liquid films flowing down vertical fibers present a wealth of complex and interesting interfacial dynamics, including the formation of droplets and traveling wave patterns. Such dynamics is an important consideration in various applications, such as fiber coating and direct-contact heat and mass exchangers which take advantage of extended interfacial areas and larger residence time afforded by the bead formation along the fiber. A rigorous investigation on the fluid dynamics and interfacial heat and mass transfer mechanism of liquid films flowing along vertical strings is, thus, needed to enable physics-based optimization and analysis of multi-string designs for the mentioned applications. This dissertation presents a combination of experimental, numerical, and theoretical study of liquid films flowing down a vertical fiber. Additionally, we report a first-ever combined experimental and theoretical study of the instability in thin film flows of a high–surface energy low-viscosity liquid (i.e. water) along cotton threads. Utilizing our

finding, we then adapted the multi-string configuration for novel applications, such as humidification, dehumidification, and particle capturing.

We started with a thorough experimental study of viscous liquids flowing down vertical fibers (i.e. polymer strings). Previous researchers suggested that the liquid film thickness and velocity profiles of nearly flat portion of a liquid film that precedes the onset of instability can be specified regardless of the nozzle geometry. As a result, they largely overlooked the effects of nozzle on the pattern and characteristics of the downstream flow. We performed a systematic experimental study by varying the nozzle inner diameter from 0.5 to 3.2 mm at various mass flow rates (from 0.02 to 0.08 g/s). We focused on experimental conditions within the Rayleigh−Plateau (RP) instability regime, where traveling wave solution emerges and generates uniformly-spaced drop-like liquid beads on vertical fibers. Our results emphasize the strong influence of nozzle geometry on the flow regime and the flow characteristics. We experimentally measured the thickness of the flat film portion after the nozzle, which we term the preinstability thickness, and identified it as a flow parameter which governs the size, spacing, and velocity of downstream liquid beads. We also performed a set of complementary numerical simulations that solves the full Navier-Stokes equations to predict the fluid dynamics of the downstream flow, such as the liquid velocity profile along the fiber.

To better understand the influence of nozzle diameter on the regime transition as well as the downstream bead dynamics, we performed a detailed theoretical study of viscous flow down a vertical fiber. We proposed a full lubrication model that includes slip boundary conditions, nonlinear curvature terms, and a film stabilization term, and compared the predicted film dynamics against the experimental results. Numerical simulations confirm that in addition to fiber sizes and flow rates, the downstream flow regime and characteristics are also significantly affected by the nozzle geometry. Moreover, the effect of film stabilization term on the flow pattern and bead

characteristic is studied. We also compared our results with previously studied theoretical methods, such as CM model, linear curvature model, and full curvature model.

Additionally, we leveraged our successful demonstration of stable water flow along a vertical cotton string to construct a multi-string water vapor capturing system, where a massive array traveling water beads act as the condensation interface for water vapor in the counterflowing air stream. These water beads form through intrinsic flow instability and offer high curvature surfaces to enhance the vapor condensation rate. The effects of the water flow rate and air velocity on the condensation rates are experimentally characterized. The gas-stream pressure drop of the design is also measured. The condensation rates and gas-stream pressure drop from our multi-string dehumidifier is compared with the existing dehumidifier designs. A simplified theoretical model is also presented as the starting point for further optimizing the design parameters of our device.

Finally, we extended our investigation for potential applications of the cotton-based multi-string configuration and proposed a novel string-based particle collector. Wet electrostatic precipitators (WESP) are generally highly effective for collecting fine particles in air streams from various sources such as diesel engines, power plants, and oil refineries. However, some limiting factors, such as high water usage, poses restrictions. Our new compact particle collector utilizes an array of traveling water beads on vertical cotton strings to collect the pre-charged particles in the counterflowing air stream. The experimental and numerical investigation presented in this work is performed to determine the collection efficiency and the optimal water flow rate for our new design. The unique configuration of our string-based counterflow WESP in this study exhibits high number-based collection efficiency, > 80%, for a wide range of particle diameters, 10 nm – 2.5 μm, while decreasing the water usage significantly, which can provide a basis for the design of more water-efficient WESPs.

The dissertation of Abolfazl Sadeghpour is approved.

Adrienne G. Lavine

Jeffrey D. Eldredge

Thomas G. Mason

Yongho Ju, Committee Chair

University of California, Los Angeles

2020

I would like to dedicate this dissertation to my family, especially my mother and father. I have no doubt that without their continued support, I could not have gotten this far.

TABLE OF CONTENTS

LIST OF FIGURES

Acknowledgments

It has truly been an unforgettable journey at UCLA for me and I have several people to thank for that. I would like to first express my sincere appreciation and gratitude to my advisor, Professor Yongho Sungtaek Ju, for his continuous guidance and support throughout my PhD research. I could not have asked for a better thesis supervisor. I also thank him for his insightful suggestions for my future career development.

I would like to then thank my committee members, Professor Adrienne Lavine, Professor Jeff Eldredge, and Professor Thomas Mason, for honoring me by being one of my PhD committee members as well as their valuable suggestions and encouragement in the last four years.

Professor Andrea Bertozzi has been a great pillar of support and guidance and I could not have asked for a better mentor to collaborate with. I would also like to thank Dr. Hangjie Ji and Dr. Claudia Falcon for making our collaboration so successful and for their helpful insights over that past three years.

I am indebted to my friends - Samira, Sepehr, Hamed, and many others - for keeping me sane for the last four years and collaborating with me. I am certain that they will go on to become very successful in their future careers. I am especially thankful to Mr. Navid Dehdari Ebrahimi. We joined the Multiscale Thermosciences Laboratory (MTSL) at UCLA at the same time and since then, he has been a great friend, roommate, and co-author for me. A very special thanks to Laila for proof reading my manuscripts and more importantly for her friendship and support.

Dr. Zezhi Zeng was a PhD student in the group when I joined UCLA. He was extremely supportive and taught me several things. Our collaboration resulted in several publications and I owe him my sincerest gratitude. I wish him all the best with his future career.

I would like to express my wholehearted thanks to all the former and current MTSL group members- Jinda Zhuang, Cheng Peng, Yide Wang, Chao Fan, Zhengxian Qu, Dong Hyun Ko, and Erfan Sedighi. Thank you for being such a joyful group to work with and your help during my stay at UCLA. Many thanks to the awesome administrative staff at UCLA-Ms. Marla Cooper, Mr. Abel Lebon, Ms. Evgenia Grigorova, and Lance Kono. I would like to thank Mr. Benjamin Tan and Mr. Miguel Lozano for their friendship and their contribution in device fabrication.

Last but definitely not least, I would like to thank my mother, father, and brothers for always being there for me no matter what.

VITA

2011-2015	Bachelor of Science, Mechanical Engineering Sharif University of Technology, Tehran, Iran
2015-2020	Graduate Student Researcher/Teaching Assistant Mechanical and Aerospace Engineering Department University of California, Los Angeles

PUBLICATIONS

Publications

Sadeghpour, A., Zeng, Z. and Ju, Y.S., 2017. "Effects of Nozzle Geometry on the Fluid Dynamics of Thin Liquid Films Flowing down Vertical Strings in the Rayleigh–Plateau Regime". *Langmuir*, 33(25), pp.6292-6299.

Sadeghpour, A., Zeng, Z., & Ju, Y. S., 2019. "A highly effective multi-string humidifier with a low gas stream pressure drop for desalination". *Desalination*, 449, 92-100.

Sadeghpour, A., Z. Zeng, H. Ji , N. Dehdari Ebrahimi , A. L. Bertozzi, Y. S. Ju, "Water vapor capturing using an array of traveling liquid beads for desalination and water treatment". Science Advances, 5, aav7662 (2019).

Sadeghpour, A., Ji, H., Ju, Y., & Bertozzi, A. (2020). "Influence of nozzle geometry on thin film dynamics flowing down a cylinder". Journal of Fluid Mechanics, (Under preparation)

Sadeghpour, A., F. Oroumiyeh, D. H. Ko, Y. Zhu, Y. S. Ju (2020). "Experimental study of a multi-string counterflow wet electrostatic precipitator for collection of diesel particulate matter (DPM)". Journal of the Air & Waste Management Association, (Under preparation)

Ji, H., Falcon, C., **Sadeghpour, A.**, Zeng, Z., Ju, Y., & Bertozzi, A. (2019). "Dynamics of thin liquid films on vertical cylindrical fibres". Journal of Fluid Mechanics, 865, 303- 327. doi:10.1017/jfm.2019.33

Zeng, Z., **Sadeghpour, A.**, Warrier, G. and Ju, Y.S., 2017. "Experimental study of heat transfer between thin liquid films flowing down a vertical string in the Rayleigh-Plateau instability regime and a counterflowing gas stream". *International Journal of Heat and Mass Transfer*, 108, pp.830-840.

Zeng, Z., **Sadeghpour, A.** and Ju, Y.S., 2018. "Thermohydraulic characteristics of a multi-string direct-contact heat exchanger". *International Journal of Heat and Mass Transfer*, 126, pp.536-544.

Zeng, Z., **Sadeghpour, A.** and Ju, Y.S., 2018. "Experimental study of heat transfer and pressure drop in a multistring based direct contact heat exchanger" *Proc. 16th Int. Heat Transfer Conf.*

CHAPTER 1

Introduction

1.1 Motivation

The characteristics of thin liquid films flowing down vertical strings of diameter of the order of 1 mm has attracted a lot of experimental and theoretical interest due to their wealth of new dynamics that illustrate the need for more advanced theory and their significance in fiber coating and direct-contact heat[1], [2] and mass exchangers[3], [4]. The latter has diverse applications, including dry cooling of thermoelectric power plants, thermally driven absorption/adsorption chillers, thermal energy recovery[5], and water vapor, fine particles or CO_2 capturing[6]–[9]. Past studies showed that wetted wire columns deliver comparable heat transfer performance at lower air pressure drops than packed beds[10],[11]. Rigorous fundamental understanding of liquid film flows along vertical strings is important for physics-based design and optimization of such heat and mass exchangers.

1.2 Study of liquid films flowing down highly curved surfaces

As a liquid film flows down a thin string of high curvatures, interplay among surface tension, viscous diffusion, and inertia leads to flow instability, creating periodic or aperiodic liquid beads traveling along the strings. Rayleigh described the importance of surface tension in wave formation in liquid columns[12]. A comparison between liquid film flows over a planar and a curved surface

illustrated the effects of surface curvature on velocity profiles[13]. Trifonov et al.[14] studied the nonlinear wavy regimes of viscous liquid film flows on vertical wires using integral method. Quéré observed the formation of axisymmetric drops when a wire was drawn from a liquid bath and related the liquid bead formation to mean flow advection[15], [16]. Kalliadasis et al.[17]showed that for film thicknesses larger than a threshold value, the Rayleigh-Plateau instability triggers natural disturbances of the flow, which then leads to liquid drop formation.

Previous studies largely overlooked the effects of nozzle geometry on the characteristics of liquid film flows down vertical strings. One generally considers that a liquid film has a smooth or non-wavy region that extends from the nozzle to the location of the onset of instability. The liquid velocity profile within such a non-wavy region was assumed to be given by the so-called Nusselt solution, which is not a function of axial position and nozzle geometry. This approximation may have been made in part to facilitate obtaining solutions to simplified Navier-Stokes equations. To mitigate challenges in the alignment of strings, experimental studies may also have employed large-diameter nozzles, which may have obscured the effects of nozzle geometry. With a "pre-instability" region prescribed independent of the nozzle, all parameters characterizing liquid flows, including liquid bead frequency and diameter, were considered to be independent of the nozzle radius. Our recent study [11], however, suggested that the nozzle radius does influence liquid-film flow characteristics, including the liquid bead diameter and bead frequency.

Interplay among surface tension, inertia and viscous forces governs liquid film flowing down a vertical string which has the potential to show various patterns such as regular train of drop-like beads or solitary waves (wavelike regime)[18]. Previous studies proposed flow regime maps in terms of the liquid mass flow rate, string diameter and liquid properties [19]. Figure 1. 1 shows one such regime map based on the normalized string radius R_s/l_c and the film aspect ratio α_N =

h_N/R_s. Here, R_s is the radius of the string; l_c is the capillary length of the liquid; and h_N is the Nusselt thickness or the thickness of a flat liquid film before the onset of instability. The Nusselt thickness in turn is a function of the liquid mass flow rate and the string radius but is independent of nozzle geometry.

The ratio between the growth time of RP instability, τ_g, and the time needed for the flow to displace its wave over the wavelength, τ_a, defines the saturation number β^*. The saturation number is a function of α_N and R_s/l_c and β^* is defined as:

$$\beta^* = \left[\frac{3u_N}{2u_i} \frac{\alpha}{(1+\alpha)^4} \right]^{\frac{2}{3}} \left(\frac{l_c}{R} \right)^{\frac{4}{3}} \tag{1.1}$$

The curve $\beta^* = 1$ divides the coordinate plane into an inertia-dominated region to its right and a surface tension-dominated region to its left. The curve $\beta^* = 1.507$, obtained from a dispersion analysis on traveling beads, demarks a transition between absolute and convective instability. In convective instability, liquid films exhibit disturbed noise-driven flows where liquid drops are not uniformly spaced and exhibit coalescence. In this study, we limit ourselves to flows in the RP regime with absolute instability.

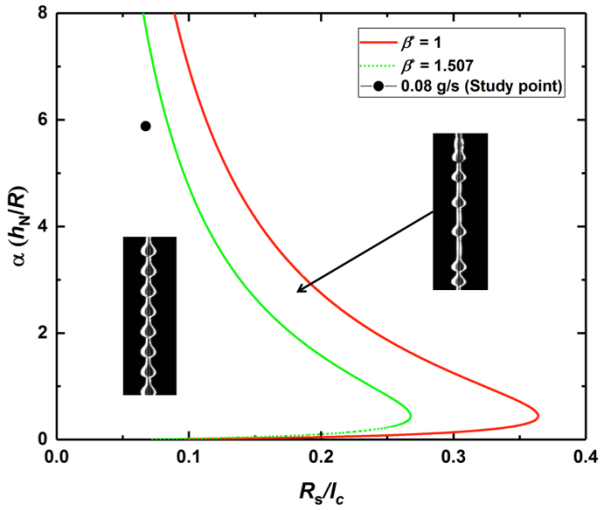

Figure 1. 1: Flow regime map for thin liquid film flows down vertical strings. The symbol represents one flow condition we investigated: silicone oil v50 with a mass flow rate Q = 0.08 g/s on a string of diameter 0.2 mm.

One limitation of this flow regime map is its inability to capture the effect of nozzle geometry. Our numerical simulation and experimental results show that cases with the same liquid mass flow rate, string diameter and working liquid can exhibit very different flow regimes (e.g., isolated droplet regime; the convective instability regime; and the Rayleigh-Plateau instability regime) depending on the nozzle diameter (see Figure 1. 2).

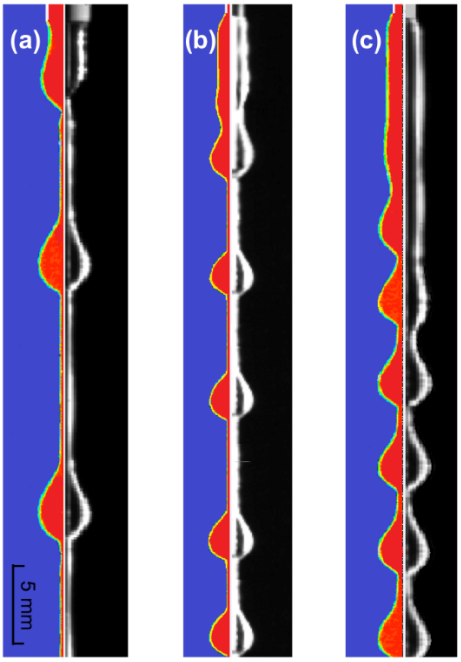

Figure 1. 2: Experimental and numerical simulation results under the flow condition specified in Figure 1. 1 for nozzles with outer diameters of (a) 2.3 mm, (b) 0.7 mm and (c) 1.06 mm

Accordingly, it is necessary to rigorously study the influence of nozzle geometry on the fluid dynamics of a thin liquid film flowing down a vertical string using experimental, numerical and theoretical modeling methods. We also need to study the water vapor or particle collection mechanism for a flow of water along a vertical cotton string to better evaluate the feasibility of developing string-based dehumidifiers and particle collectors.

1.3 Application of the liquid flow along vertical strings

The unique configuration of liquid flow along a vertical string presents intriguing advantages for heat and mass exchanger design by offering high interface-to-volume ratios, significantly lower gas-stream pressure drops, and long residence times of liquid beads for heat and mass transfer by taking advantage of the viscous shear stress exerted by the string surface, which opposes

downward sliding motion of liquid beads. In the present work, we leverage our understanding of this configuration to propose two novel applications for the water flow along a single or multiple vertical cotton strings.

1.3.1 Water vapor capturing and desalination

Fresh water is a precious and scarce resource. Recent studies projected that severe droughts and other extreme weather events will occur at ever more increasing intensities and frequencies, placing greater strains on already limited fresh water resources in many parts of the world. Researchers found that more than half of the global population live in areas with severe water scarcity condition for more than one month per year [20]. Past and on-going research efforts have led to the development and refinement of various solutions for this problem such as desalination and water treatment technologies, including reverse/forward osmosis, nano-filtration, electrodialysis, and thermal distillation. Other novel approaches, such as ambient moisture harvesting [21], [22] and fog/mist collection[23], have also received increasing attention.

Water vapor capture is an integral part of many fresh water production methods, including aforementioned ambient moisture harvesting, vapor recovery from cooling towers in thermoelectric power plants, and ambient-pressure humidification-dehumidification (HDH) desalination systems. The HDH desalination system is an intriguing desalination and water treatment approach [24], which imitates the natural rain cycle by creating humidified air (e.g., blowing dry air over a heated brine) and then condensing water vapor, using a water vapor capturing device (hereinafter referred to as “dehumidifier”), to produce distilled water. It is attractive for small-scale distributed desalination and water treatment because they are very tolerant to high salinity and can produce high-quality (distilled) water using a wide variety of feed

water streams, including industrial and agricultural wastewater, produced water from oil/gas fields, contaminated ground water, and brine discharge from reverse osmosis or membrane filtration plants.

We propose a new multi-string dehumidifier configuration where water vapor in a humidified air stream is condensed on traveling water beads. The traveling water beads themselves are generated by the intrinsic instability of thin liquid films flowing down an array of vertical threads (Figure 1. 3) without requiring the use of spray nozzles or application of electric fields. This unique dehumidifier configuration presents an intriguing model system for heat and mass transfer by leveraging the mentioned advantages of the multi-string configuration and offering efficient mass diffusion of vapor toward local curved surface features (liquid beads) that act as sinks. Despite offering high interface-to-volume ratios, the multi-string array introduces small pressure drops for gas flows in part because it provides straight, open and contiguous gas flow paths and in part because low-profile traveling liquid beads present relatively small form drag [2], [6], [3], [25].

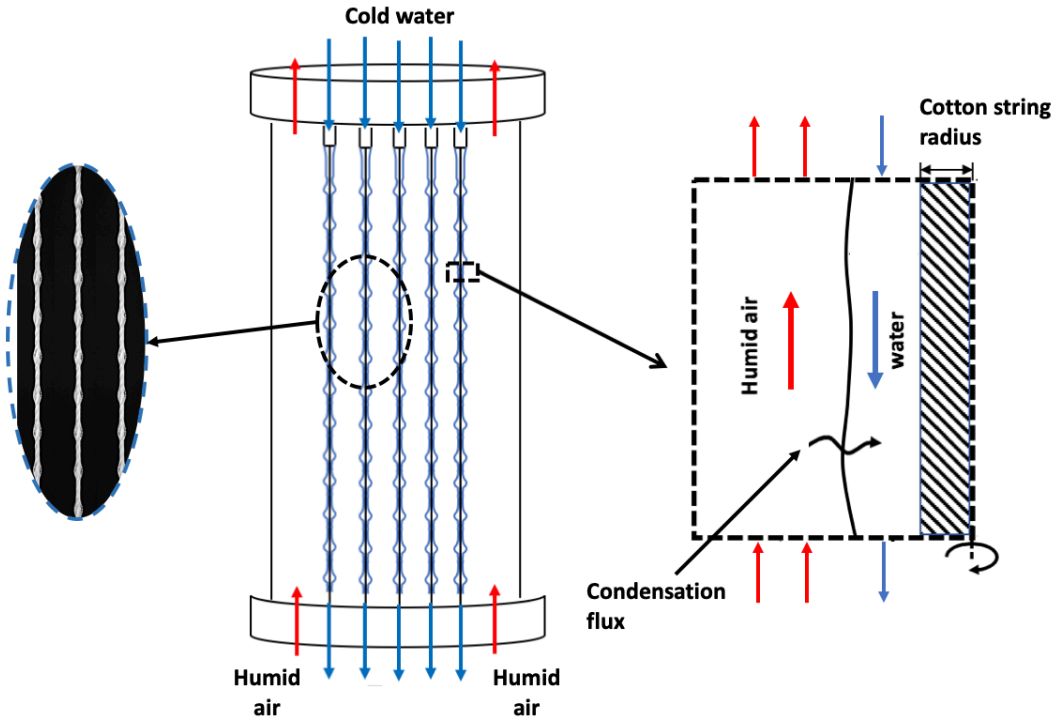

Figure 1. 3: Schematic of a multi-string dehumidifier unit used to capture water vapor content in the counterflowing air stream

1.3.2 Fine and ultrafine particle collection

Diesel engines offer superior fuel efficiency and power to their gasoline counterparts. However, they are considered one of the major particulate emitters in many urbanized and developing cities. Reducing diesel generated particulate matter (DPM) has attracted a lot of attention from researchers and governments due to its potential to cause severe health and environmental issues [26]–[32]. Current engine technologies and strict governmental regulations aim for reduction in particle emission rates of diesel engines [33]. However, the benefit of emission rate reduction remains rather elusive. Previous studies showed that the major portion of particles emitted from diesel engines are smaller than 2.5 μm in diameter, referred to as fine particles [34], [35]. Fine particles have greater impact on human health because they have elevated toxin burdens, can

penetrate deep inside the respiratory system, and translocate into the circulation system [36]–[40]. Among these fine particles, those with diameter less than 0.1 μm are referred to as ultrafine particles and can be more harmful to human respiratory and cardiovascular systems [41]–[43]. Recently, these fine and ultrafine particles are also recognized to have malevolent effects on other parts of the human body such as the kidney (Xu et al. 2018).

Electrostatic precipitators (ESPs) are widely used to collect PM from various systems, such as coal power plants and diesel engines. It utilizes high voltage electric fields and corona discharge to electrically charge particles, which are then collected on to plates of the opposite charge. Traditional electrostatic precipitators handle large volumes of gas (up to about 1900 m^3/s), maintain a low pressure drop (less than 150 Pa), operate at high gas temperatures (up to 650°C), and deliver high overall mass collection efficiencies [44]. But, they suffer from significant decrease in the collection efficiency for fine particles with minimum occurring for particles of diameters around 0.2 to 0.5 μm [45], [46], which is the size range of the majority of diesel emissions. To address this issue, two-stage ESPs have been studied to improve fine particle removal rates by separating the charging and collection chambers. However, previous studies noted that, even with two-stage ESPs, the collection efficiency of fine particles remains low due to the re-entrainment effect inherent to traditional dry-type ESPs [47].

We propose a new design for particle collection in the form of a cotton-based multi-string collector where thin films of water flow down vertical cotton strings and act as the collection surfaces. This type of particle collector, in which the collection plate is continuously washed by a liquid stream, is referred to as wet electrostatic precipitator (WESP). Our multi-string collector consists of a single cotton string (or an array of vertically aligned cotton strings) as illustrated in Figure 1. 4. Water is flown down the cotton string while making direct contact with a

counterflowing gas stream that carries the pre-charged fine and ultra-fine particles. This unique configuration presents very high residence time for the particle collection process in a compact configuration at significantly low air-stream pressure drops and water consumption rates. To enable physics-based systematic design of this unique single/multi-string particle collector, rigorous investigation of the trajectory of the collected particles and the fluid dynamics of water flowing down a vertical cotton string under the influence of gravity and an electric field is needed.

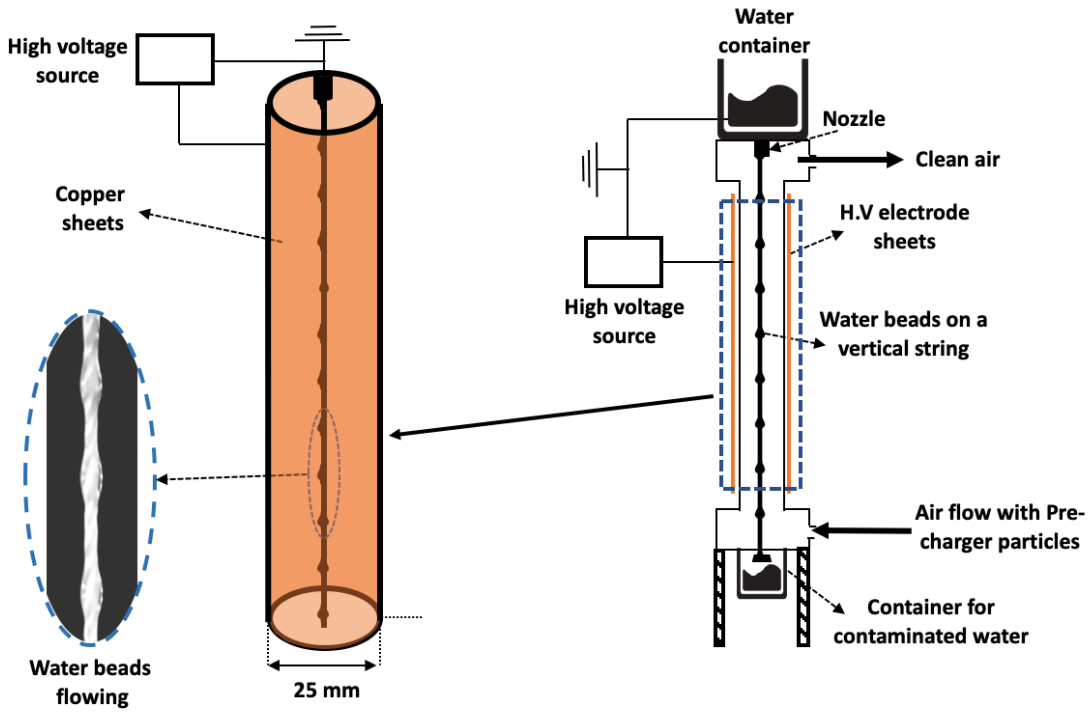

Figure 1. 4: Schematic illustrating the operation of a single-string cylindrical collector

1.4 Objectives of the present study

The present study aims to (i) present a combined experimental, numerical, and theoretical study to help identify the critical parameters governing the flow regime and the characteristics of a thin

liquid film flowing down high curvature surfaces (i.e. polymer fiber or cotton strings), such as nozzle geometry and preinstability thickness, (ii) report a first-ever combined experimental and theoretical study of the instability in thin film flows of a high–surface energy low-viscosity liquid (i.e. water) along cotton threads, (iii) experimentally study the condensation performance and the air-stream pressure drop of a novel multi-string dehumidifier and compare this design to other existing dehumidifiers in terms of performance and operational cost, (iv) construct a reliable numerical simulation framework to help interpret and predict the experimentally obtained heat/mass transfer efficiencies from the multi-string dehumidifier, and (v) conduct an experimental investigation on the performance of a new water-efficient counterflow WESP design.

1.5 Organization of the thesis

This dissertation studies the characteristics and applications of thin liquid films flowing down high curvature surfaces.

Chapter 2 presents a combined experimental and numerical study of the effect of nozzle geometry on the fluid dynamics of a liquid film flowing down a vertical sting. We performed a systematic experimental investigation by varying the nozzle inner diameter in the range of 0.5 to 3.2 mm. The experimental results are recorded using a high-speed camera and analyzed to evaluate the characteristics of the downstream flow, such as the spacing, size, frequency and travelling speed of the liquid beads. We limited our study to the Rayleigh-Plateau (RP) regime, where uniformly-spaced drop-like liquid beads flow down on a vertical fiber. To help interpret the experimental results, a set of time-dependent full Navier-Stokes equations is solved using a commercially available numerical simulation software.

Chapter 3 extends our experimental and numerical study to theoretical modeling of the effect of nozzle geometry on the dynamics of thin liquid films flowing down on vertical fibers. We proposed a full lubrication model including the slip boundary condition, various curvature terms and a film stabilization term. We analyzed the modeling results to evaluate the characteristics of the downstream flow as well as the nearly flat film region of the flow that proceeds the onset of instability. The fluid characteristics of the flow resulted from our model is then compared to that of the experiments and previously studied theoretical models.

Chapter 4 presents a highly-efficient compact multi-string dehumidifier design as a novel application for the multi-string configuration. We demonstrated a stable water flow along a vertical cotton string and constructed two 0.7 m-tall dehumidifier prototypes (52 and 96 cottons strings), where the water vapor in the counterflowing air steam is condensed on the surface of the water beads, which are flowing down along the cotton threads. We measured the axial variations in the water and air temperature and the air-stream pressure drop to examine the impact of the water and air flow rates, instability modes, and string pitch on the heat and mass transfer performance of our multi-string dehumidifier.

Chapter 5 explores the application of using the cotton-based single/multi-string configuration for particle capturing purpose. We constructed two particle collector designs, utilizing the water flow on cotton strings as the particle collection medium. We performed a combined experimental and modeling study to validate and further optimize our particle collector design. The particle collection efficiency and the water consumption of our design is experimentally measured and compared with existing particle collector designs. The effect of water and air flow rate, and applied collector voltage on the collection performance is also studied.

CHAPTER 2

Effects of Nozzle Geometry on the Fluid Dynamics of Thin Liquid Films Flowing down Vertical Strings in the Rayleigh-Plateau Regime

Thin-liquid films flowing down vertical strings undergo instability, creating wavy film profiles and traveling beads. Previous studies assumed that the liquid film thickness and velocity profiles within the healing length from a nozzle were specified by the Nusselt solution, independent of the nozzle geometry. As a result, the influence of the nozzle diameter on the flow characteristics, such as the liquid bead size, spacing, and traveling speed, was largely overlooked. We report an experimental and numerical simulation study on liquid-film flows in the Rayleigh-Plateau regime while systematically varying the nozzle diameter from 0.5 mm to 3.2 mm at different mass flow rates (0.02, 0.04, 0.06 and 0.08 g/s). We find that the nozzle diameter does have a strong influence on the flow regime as well as flow characteristics. We identify the thickness of a nearly flat portion of a liquid film that precedes the onset of instability, which we term the pre-instability thickness, as a critical flow parameter that govern the size, spacing, and frequency of liquid beads that develop downstream. By defining the liquid film aspect ratio α in terms of the pre-instability thickness, we capture a flow transition from the Rayleigh-Plateau (RP) instability regime to the

isolated droplet regime. An improved understanding of the flow regimes and characteristics assists a systematic design and optimization of a wide variety of processes and devices, including fiber coating and direct contact heat and mass exchangers.

2.1 Background

Early theoretical and experimental studies of liquid film flows down vertical wires employed highly viscous liquids and thin fibers to reduce the effects of gravity. They observed the existence of a dominant wavelength and the formation of uniformly-spaced beads[48]. A later study[49] investigated flows under similar conditions and developed a creeping-flow model to predict flow characteristics.

Lin et al.[50] took the gravitational force into account for the stability problem of the free coating and concluded that any flow in this configuration, regardless of the liquid Reynolds number and string diameter, is unstable. Craster et al.[51] derived an evolution model for liquid film flows under a long-wavelength approximation for the thin-layer limit where the radius of total fluid is much smaller than the capillary lengthscale, whose prediction yielded a good agreement with experimental results. Wehinger et al.[52] conducted a numerical simulation study using the multi-fluid method to capture the sinusoidal and solitary wave limits. Grünig et al.[53] experimentally investigated the fluid dynamics of a single wetted string in the presence of significant counterflowing air and observed a limit for gas load where the beads break up into small droplets and flooding occurs.

Ruyer-Quil et al.[19] developed a two-equation evolution model for liquid film flows that accounted for the effects of viscous diffusion and inertia to predict liquid film profiles as a function of time. This and follow-up studies observed wavy flow regimes, where discrete liquid beads are

formed and travel down a string at regular or irregular intervals. Extending these studies, Duprat et al.[18] proposed a flow regime map based on a parameter set including the liquid mass flow rate, liquid properties and string diameter. Flow regimes, which are affected by the effects of viscous dispersion, inertia, flow advection and azimuthal curvature, were classified into four categories[54]. Duprat et al.[18], [19], [55] also studied the effects of controlled excitations applied at the liquid inlet reservoir.

In the present manuscript, we report our combined experimental and numerical systematic study of the effects of nozzle geometry on thin liquid films flowing down a vertical string. We limit ourselves to experimental conditions within the Rayleigh-Plateau (RP) instability regime [56]. We experimentally determine how the nozzle radius influences the flow characteristics such as the healing length, liquid bead diameter, liquid bead spacing and liquid bead spatial frequency. To help interpret experimental results, we perform sets of numerical simulations. Previous studies simulated the formation of liquid beads on vertical strings under both flowing and static conditions. Mead-Hunter et al.[57] simulated the breakup of a liquid film on a vertical string using the OpenFOAM CFD package and achieved good agreement in droplet spacing with theoretical results based on the Quere theory[16]. Hosseini et al.[9] simulated thin liquid film flows using the volume of fluid (VOF) method. Their work could qualitatively capture the experimentally obtained profiles of liquid beads but the predicted liquid bead spacing deviated from experimental results. An approximate analytical model is proposed, which relates the flow characteristics.

2.2 Experimental setup and numerical simulation

We perform a systematic experimental and numerical study to investigate the influence of nozzle geometry on the flow characteristics such as the healing length, spatial/temporal frequency of traveling beads, and their spacing and size.

2.2.1 Experimental setup

Figure 2. 1 shows a schematic of the experimental setup we use to study the effects of nozzle geometry. A syringe pump is used to pump the liquid. The liquid flow rates are varied from 0.02 g/s to 0.09 g/s. A high-speed camera is mounted on an X-Y stage to capture liquid film profiles along vertically mounted Nylon strings. A frame rate of 1000 frame/second is used for all experimental results reported here. A video zoom lens is interchangeably used to capture details of individual liquid beads. The uncertainty in the liquid bead radius and length is estimated to be ± 0.08 mm and that in the liquid bead spacing ± 0.3 mm.

We use stainless steel nozzles of inner diameters varying from 0.5 mm to 3.2 mm and wall thicknesses varying from 0.1 mm to 0.2 mm in our experiments. Nylon strings of length 0.6 m and diameters of 0.2, 0.29 and 0.43 mm are mounted vertically using a weight attached at the end. A set of two X-Y stages are used to align each string such that it is centered with respect to a nozzle. We monitor the liquid mass flow rate using a precision weight scale of resolution 0.1 g with a computer readout.

Rhodorsil silicone oil v50 (density ρ = 963 kg/m^3, kinematic viscosity ν = 50 mm^2/s, surface tension γ = 20.8 mN/m at 20 °C) and Rhodorsil silicone oil v100 (density ρ = 963 kg/m^3, kinematic viscosity ν = 100 mm^2/s, surface tension γ = 20.8 mN/m at 20 °C) are used as the liquids.

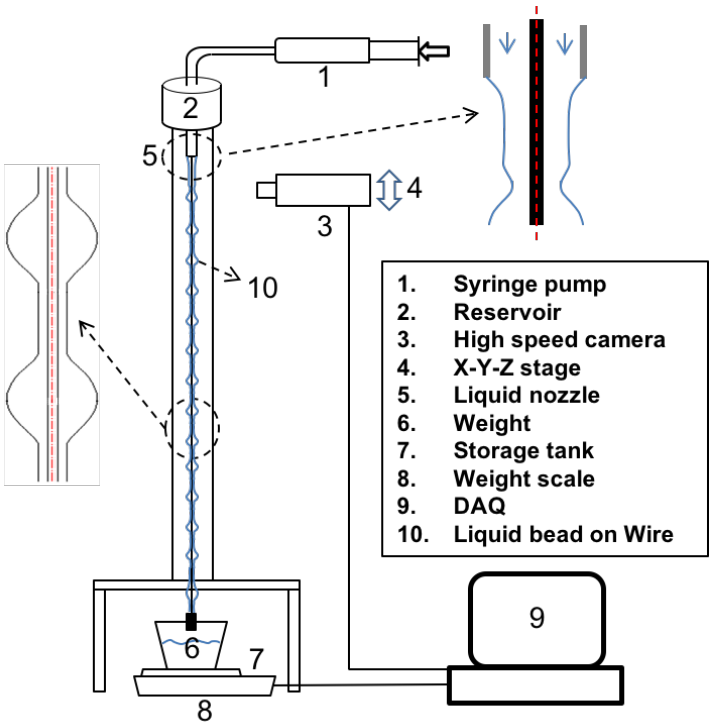

Figure 2. 1: Schematic of the experimental setup.

Using the captured video images, we extract relevant flow parameters, including the liquid bead spacing, the liquid bead temporal frequency, the liquid bead velocity, the healing length, the pre-instability thickness and the liquid bead radius (see Figure 2. 2). The first three parameters are determined from a so-called spatiotemporal diagram, which we construct by extracting a single vertical line of pixels that intersect liquid beads near their centers from each of the video frames and then juxtaposing them along the horizontal time axis. The vertical axis represents the distance from the tip of the nozzle. As for the healing length, we consider the onset of instability at the location where local perturbations exceed 4% of the mean liquid film thickness.

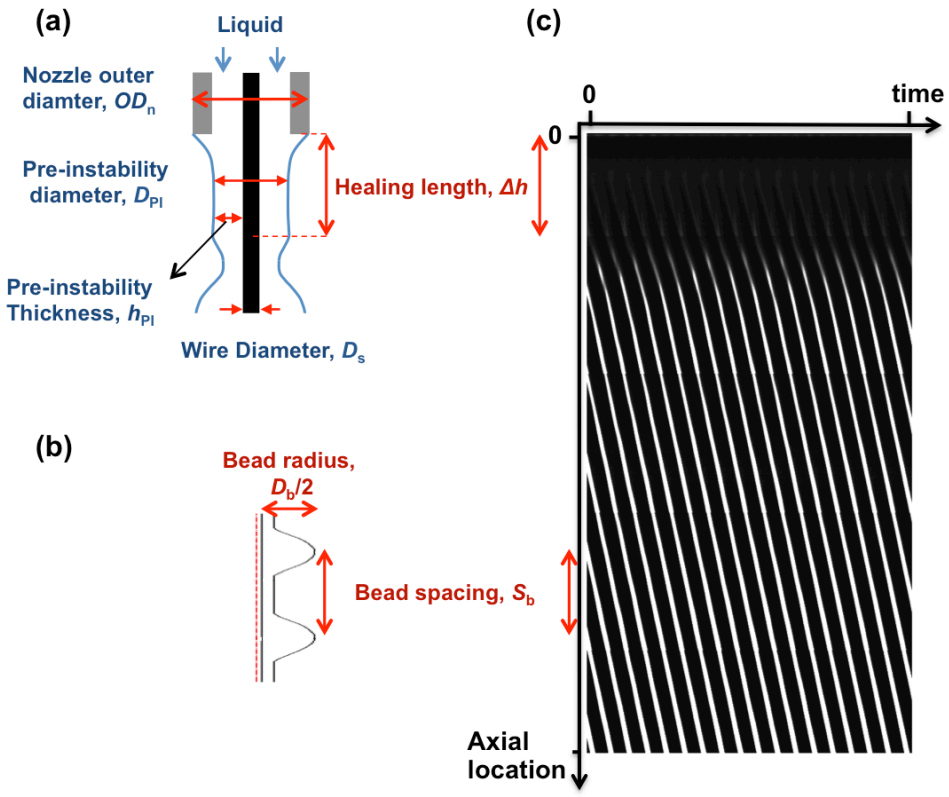

Figure 2. 2: (a-b) Schematic diagrams illustrating parameters characterizing liquid thin-film flows. (c) A representative spatiotemporal diagram experimentally obtained.

2.2.2 Numerical simulation

To help understand experimental results, we perform sets of numerical simulations. Figure 2. 3 shows the simulation domain and boundary conditions we use. We implement the volume of fluid (VOF) method within the framework of a commercial CFD package (ANSYS-Fluent) to model two-phase flows and track liquid-gas interfaces. We assume that the flows are two-dimensional and axi-symmetric. We employ an unsteady 2D solver utilizing the PISO (pressure implicit with splitting of operators) method to handle the pressure-velocity coupling. The pressure staggering option (PRESTO) is used to handle the pressure and the second-order upwind scheme is used to discretize the momentum equations. An unstructured quadratic mesh with the minimum

element size of the order of 0.01 mm and the number of mesh elements of the order of 200,000 is used in typical simulation runs. A mesh independence study is carried out to ensure that the predicted liquid flow parameters, including the liquid bead spacing and diameter, do not change by more than 2% with increasing the number of mesh elements to 400,000.

We adopt the continuum surface force (CSF) model proposed by Brackbill et al.[58], where the effect of surface tension is represented as a source term in the momentum equations. The apparent contact angle[59] is dynamically calculated based on the equilibrium of forces at each instant[60], [61]. We do not employ any artificial perturbation in our simulation but rely instead on noise inherent in numerical simulation to initiate instability.

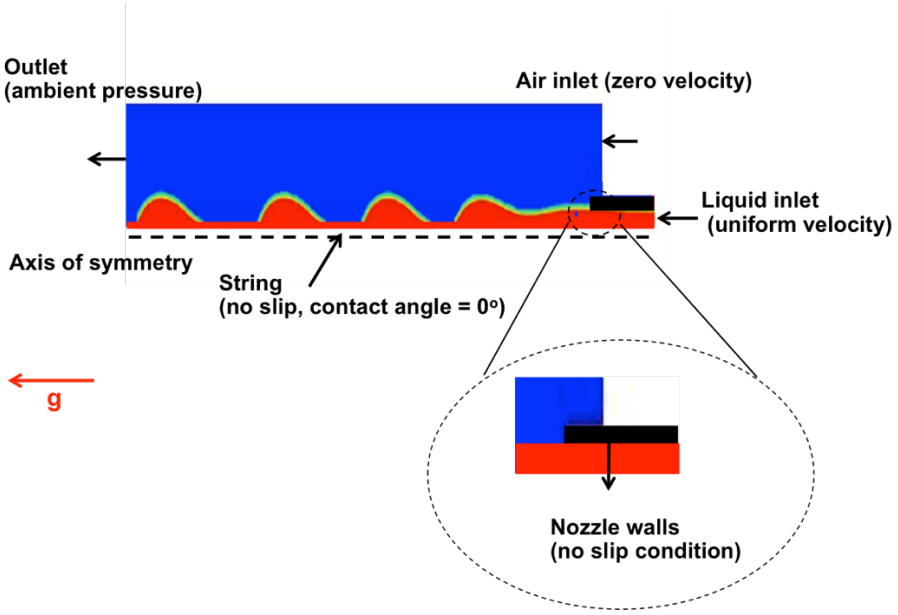

Figure 2. 3: Schematic of boundary conditions for numerical simulation

During a flow initiation stage, liquid beads formed near the nozzle spread and slide down an initially dry string. Our numerical simulation results show two liquid film profiles: (a) shortly after the beginning of a simulation run and (b) after a steady state has been established (see Figure 2. 4). The geometric characteristics of liquid beads, especially bead spacing, during this flow

initiation stage differ markedly from those under the later steady state condition. We consider that a steady-state has been reached when the spacing between 5 consecutive beads passing a fixed position varies less than 5% of their mean value. All simulation results reported later in the manuscript are obtained after such initiation stage has ended and stable liquid profiles are established.

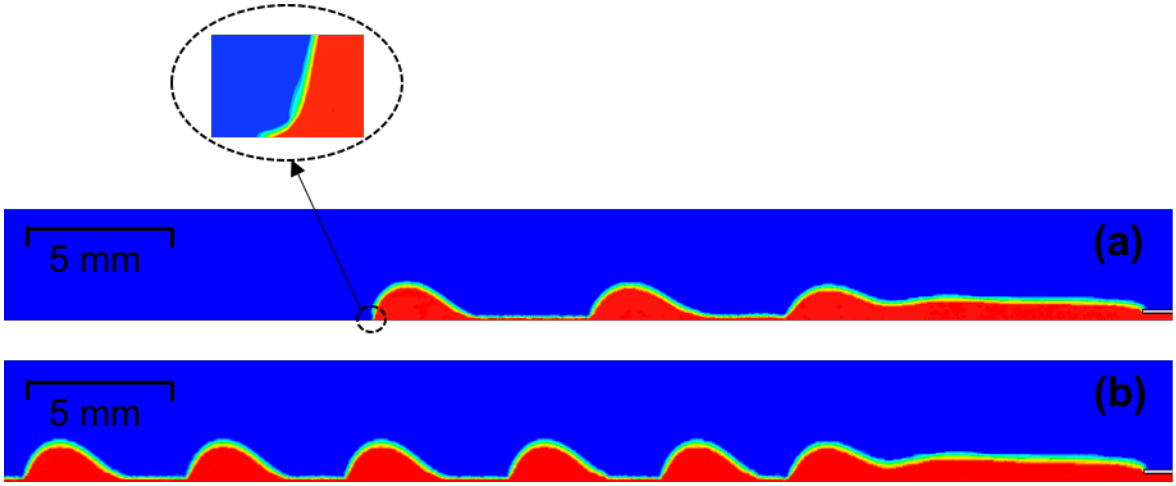

Figure 2. 4: Predicted liquid film profiles (silicone v50, Q = 0.08 g/s, nozzle outer diameter =1.06 mm) after the generation of (a) first 3 liquid beads (b) 16 beads.

2.3 Results and discussion

We first compare the relative effects of two nozzle geometric parameters: nozzle inner diameter (ID) and nozzle outer diameter (OD). Figure 2. 5 shows the predicted and measured bead temporal frequency as a function of the nozzle inner diameter. For the results shown in Figure 2. 5(a), the nozzle wall thickness is varied such that the nozzle OD is fixed. Under this condition, both the simulation and experimental results show that the flow characteristics are relatively insensitive to the nozzle ID. In contrast, the results shown in Figure 2. 5(b) are obtained from

nozzles with the same ID but different ODs. This time the bead temporal frequency (and other flow parameters) do vary appreciably with the nozzle outer diameter.

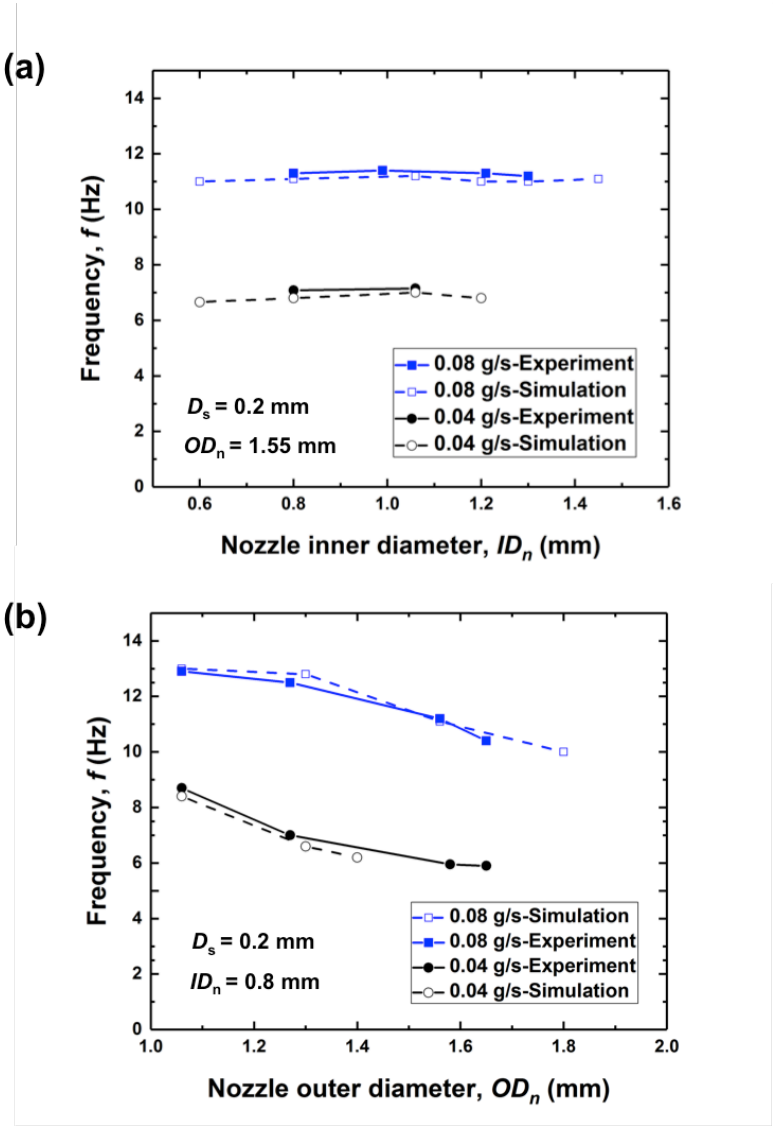

Figure 2. 5: Dependence of the liquid bead frequency on (a) the nozzle inner diameter when the nozzle outer diameter is fixed and (b) the nozzle outer diameter when the nozzle inner diameter is fixed. Two sets of data for two different liquid flow rates (Q = 0.08 g/s and 0.04 g/s) are shown. The hollow symbols correspond to our simulation results and the solid symbols correspond to our experimental results.

The above trend can be explained by considering the profile of a liquid film near the nozzle. The predicted liquid profiles for different values of the liquid contact angle illustrate that, at relatively low contact angles, as is the case for well-wetting silicone oils, the contact line remains attached to the outer nozzle surface (see Figure 2. 6 and Figure 2. 7). As a result, the liquid bead diameter and other flow parameters are governed only by the nozzle outer diameter and do not change much with the contact angle. When the contact angle exceeds a threshold value, approximately 45 degrees, the contact line recedes from the outer surface and moves towards the nozzle inner surface. The liquid bead diameter decreases more appreciably with increasing contact angle at these higher contact angles. With these results, we present all subsequent results on flow parameters as a function of the nozzle OD.

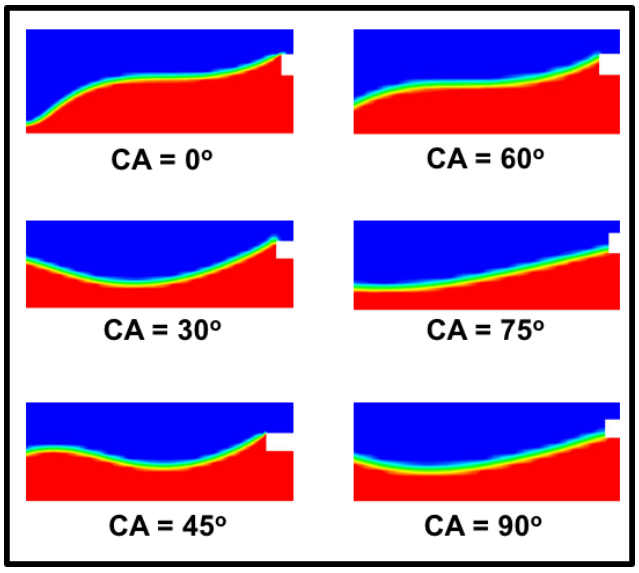

Figure 2. 6: Predicted liquid film profile near the nozzle for different contact angles at the nozzle surface. The white rectangles represent the nozzle. The red regions and the blue regions represent the liquid and the air, respectively.

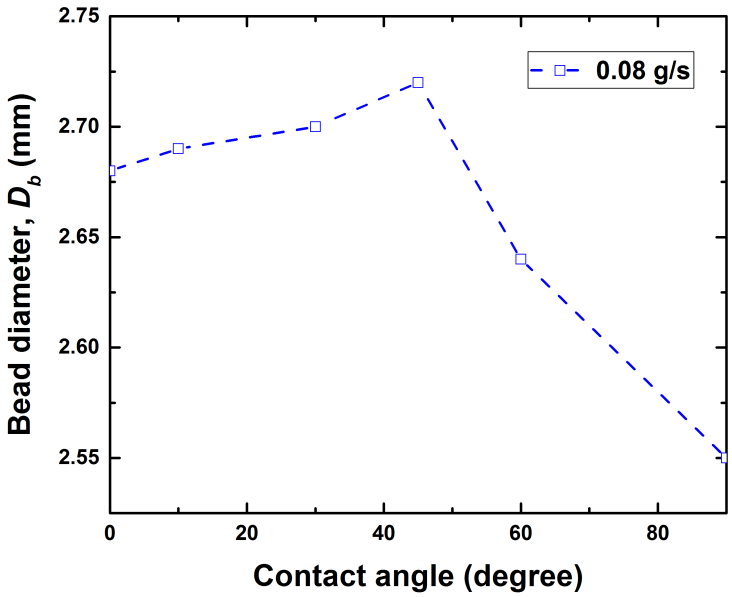

Figure 2. 7: The predicted liquid bead diameter as a function of the liquid contact angle on the nozzle surface (Q = 0.08 g/s, 0.2 mm-diameter string, nozzle OD of 2.5 mm).

Figure 2. 10 and Figure 2. 11 show two of the flow characteristics for silicone oil v50 flowing down a vertical string with a diameter of 0.2 mm at two different liquid mass flow rates of 0.04 and 0.08 g/s. The liquid bead frequency and the healing length decrease with increasing nozzle outer diameters whereas the bead spacing and the bead diameter increase with increasing nozzle outer diameters (see Figure 2. 8 and Figure 2. 9). The predicted results all agree well with the experimentally measured values.

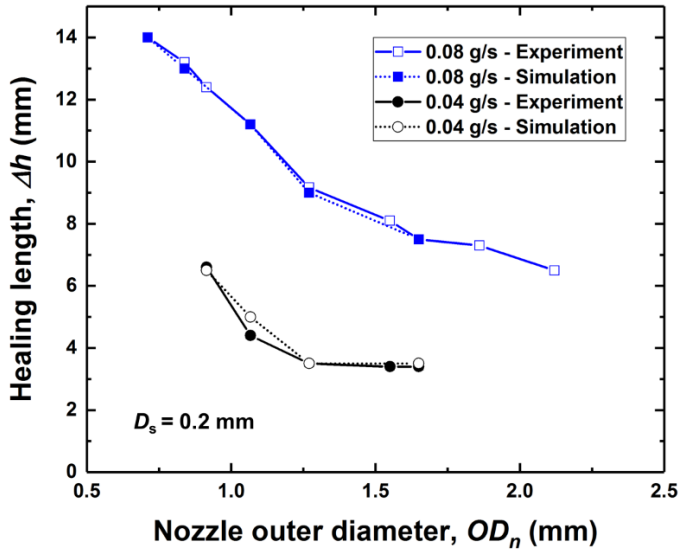

Figure 2. 8: The predicted and measured healing length as a function of the nozzle outer diameter. Two sets of results are presented for two different mass flow rates: 0.04 and 0.08 g/s.

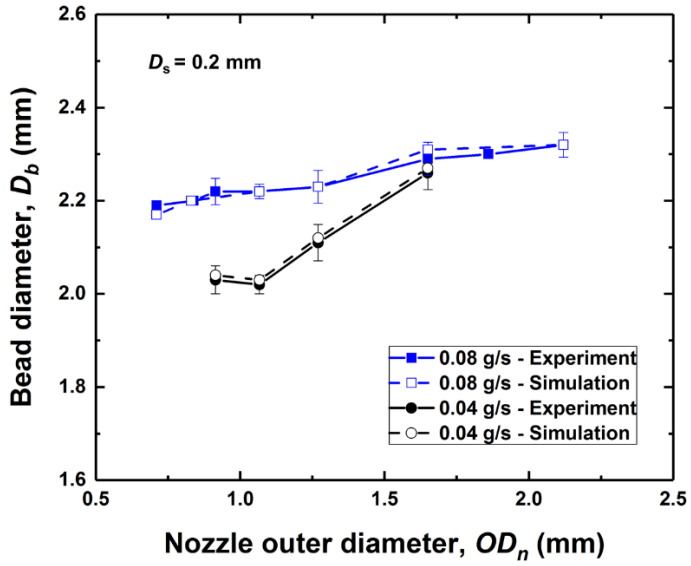

Figure 2. 9: The predicted and measured liquid bead diameter as a function of the nozzle outer diameter. Two sets of results are presented for two different mass flow rates: 0.04 and 0.08 g/s.

One noteworthy observation is that the flow regime itself can change as we change the nozzle outer diameter. Our experimental and numerical results show that the flows can transition to the isolated droplet regime, as shown in Figure 2. 10.b(III), when the nozzle outer diameter is larger than 1.6 mm (for $Q = 0.04$ g/s) or 2.1 mm (for $Q = 0.08$ g/s). At even lower liquid mass flow rates (0.025 ~ 0.04 g/s), the flows are observed to be in convective instability regime when the nozzle outer diameter is less than 0.7 mm, which is shown in Figure 2. 10.b(I). The previous flow regime map would have predicted all of these flows to be in the absolute instability regime shown in Figure 2. 10.b(II).

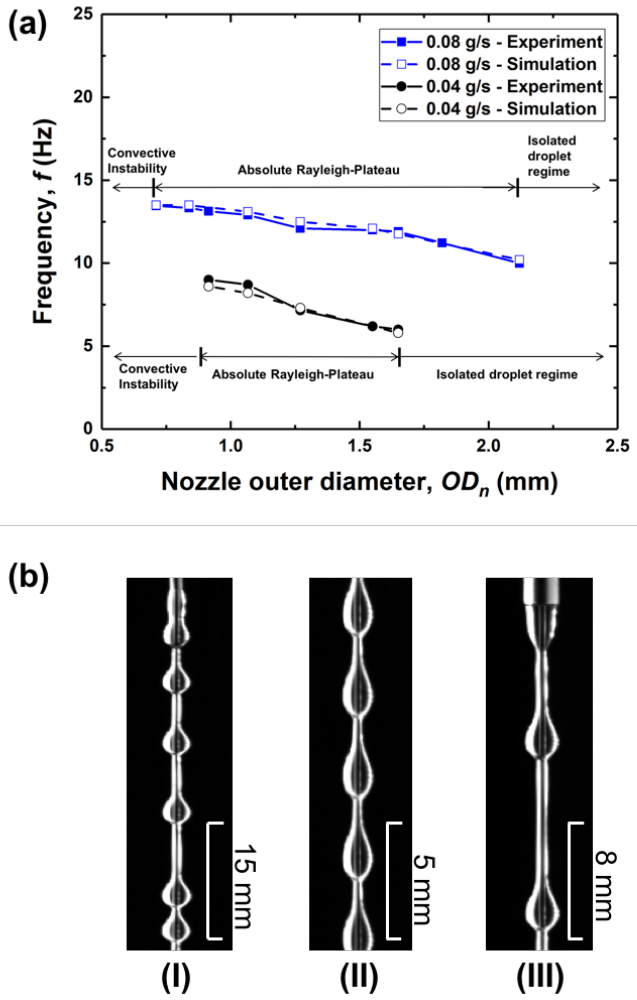

Figure 2. 10: The measured and predicted liquid bead spatial frequency as a function of the nozzle OD for RP regime in (a). Two sets of results are presented for two different mass flow rates: 0.04 and 0.08 g/s. The experimental liquid film profiles are presented for b(I) convective instability, b(II) absolute RP instability and b(III) isolated droplet regimes. Note that the experimental data shown in (a) are only for liquid film flows in the Rayleigh-Plateau regime illustrated in b(II).

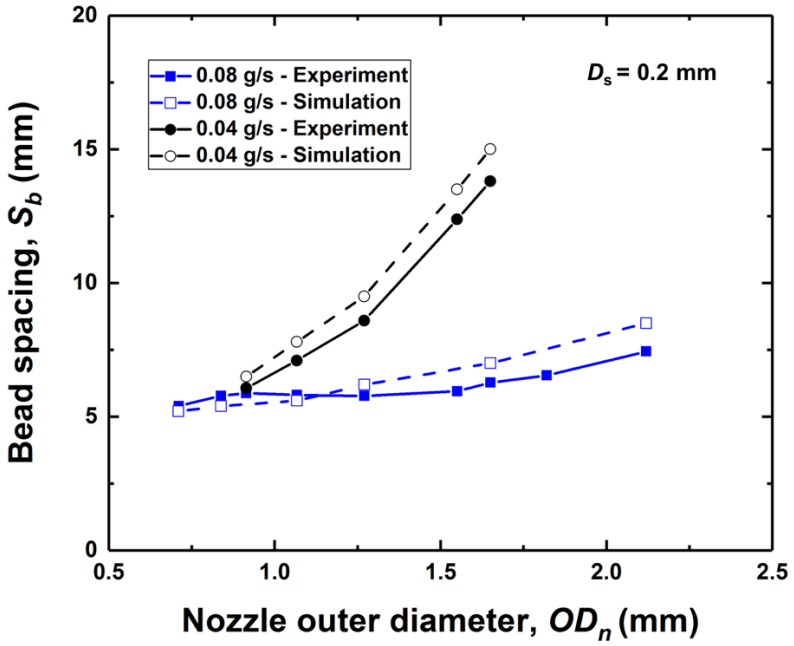

Figure 2. 11: The predicted and measured liquid bead spacing as a function of the nozzle OD. Two sets of results are presented for two different mass flow rates: 0.04 and 0.08 g/s.

We hypothesize that the pre-instability region (between the nozzle and the location of instability onset) is a key to understanding the observed dependence of the flow characteristic parameters on the nozzle outer diameter.

Figure 2. 12(a) shows the predicted liquid film profiles near two nozzles of different diameters. The flows are in the RP regime. As the liquid exits the nozzle, it develops to form (nearly) "flat" liquid-gas interfaces before any flow instability leads to the generation of a neck and subsequently discrete liquid beads. We define the thickness of this flat liquid film before the onset of the instability as the pre-instability thickness. Figure 2. 12(b) shows the predicted axial velocity profiles in the pre-instability regions at locations marked with the arrows in Figure 2. 12(a).

We note that the pre-instability thicknesses and the velocity profiles deviate from the predictions of the Nusselt model despite the fact that the string diameter and the liquid mass flow rate are kept the same for both cases.

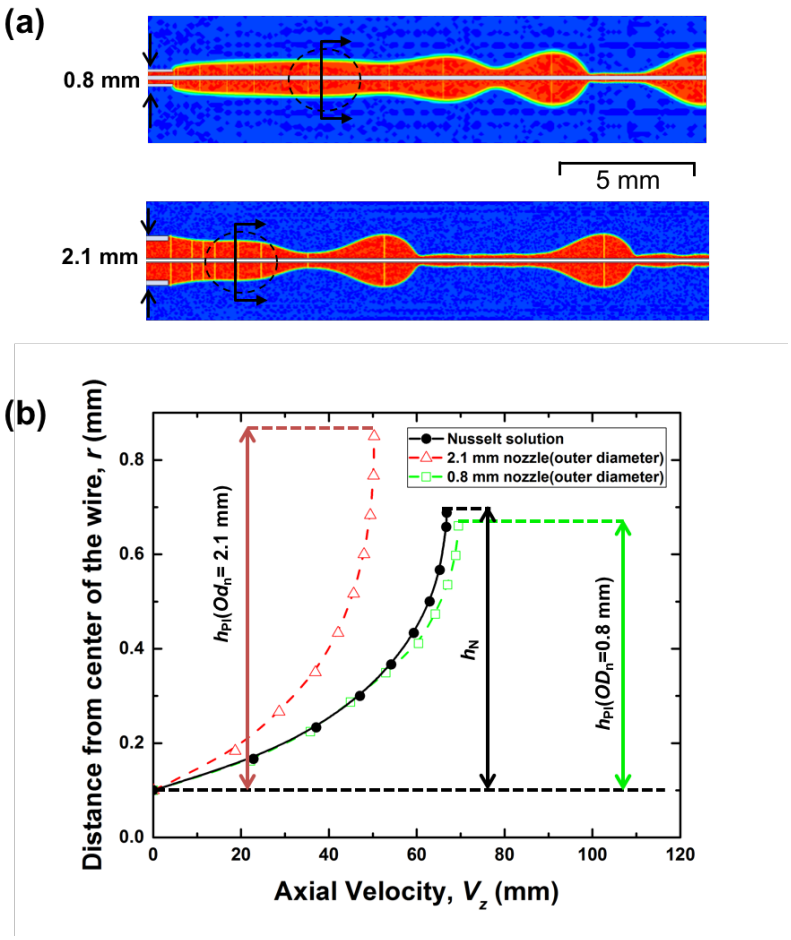

Figure 2. 12: (a) Predicted liquid film profiles near the nozzles for different nozzle outer diameters (2.1 and 0.8 mm). (b) Predicted axial velocity profiles at locations marked with arrows in the pre-instability regions. Note that the horizontal axis corresponds to the axial velocity. The hollow triangles are for OD = 2.1 mm and the hollow squares are for OD = 0.8 mm. The solid line/filled symbols correspond to the Nusselt solution.

We also examine the effect of the nozzle outer diameter on the pre-instability diameter, which is computed as the sum of the string diameter and the pre-instability thickness. We observe that the pre-instability diameter generally increases with increasing nozzle outer diameters or increasing liquid mass flow rates. These simulation results once again agree well with our experimental data (see Figure 2. 13).

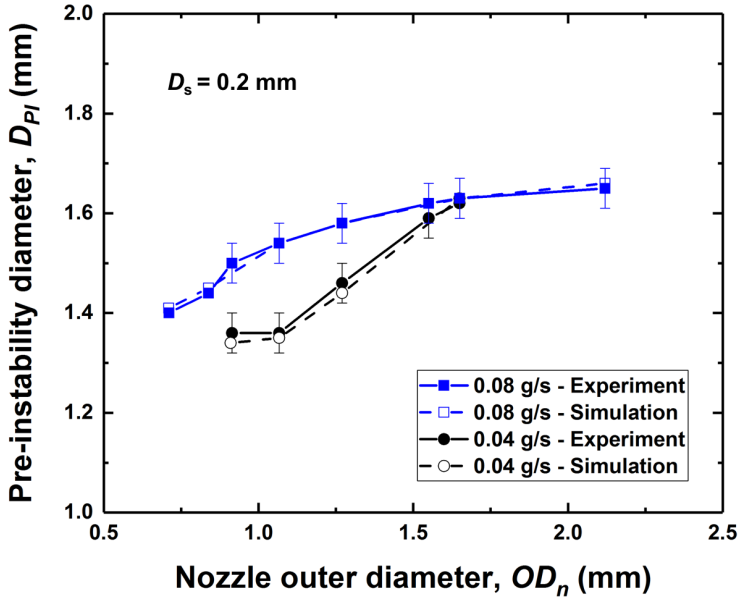

Figure 2. 13: The predicted and measured pre-instability diameter as a function of the nozzle outer diameter. Two sets of results are shown for two different liquid mass flow rates (0.04 and 0.08 g/s).

Figure 2. 14 shows the experimentally measured pre-instability diameter as a function of the nozzle outer diameter in the RP regime using strings with different diameters, different liquids with different viscosities, and different liquid mass flow rates. Once again, we observe that the pre-instability diameter increases with the nozzle outer diameter. At the higher flow rates, the pre-instability diameter approaches a limiting value of approximately 1.65 mm. At the lower liquid flow rates, the pre-instability diameter also increases with increasing nozzle outer diameters but

the flows transition into the isolated droplet regime before the pre-instability diameter reaches the limiting value. These trends are observed for both fluids and all the string diameters examined.

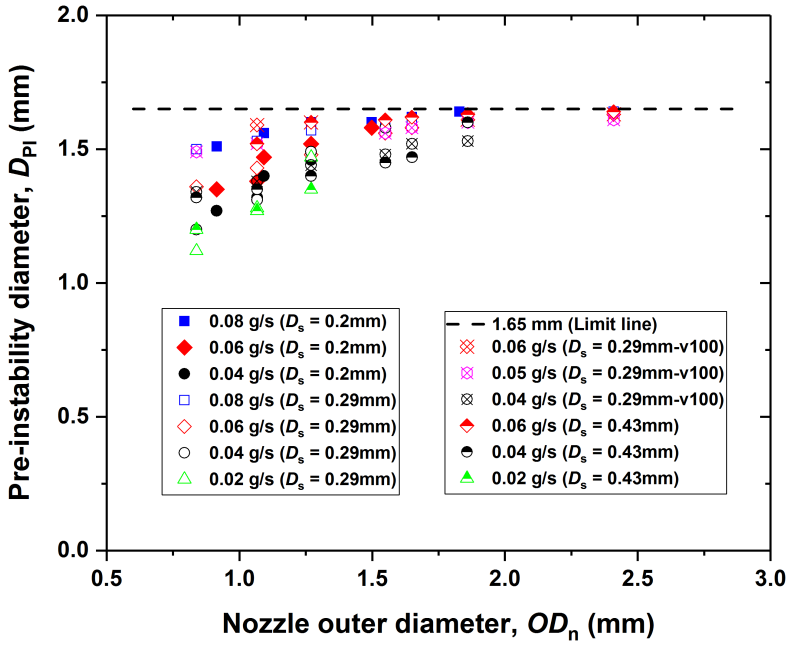

Figure 2. 14: The pre-instability diameter experimentally measured as a function of the nozzle outer diameter. Experiments are performed using two different liquids (silicone oil v50 and v100); three different string diameters (0.2, 0.29 and 0.43 mm); and four different liquid mass flow rates (0.02, 0.04, 0.06, and 0.08 g/s).

The flow regime map reported in previous studies does not have any provision to account for the effects of the nozzle geometry. We propose a modified flow regime map where we attempt to account for the influence of the nozzle outer diameter by replacing the Nusselt thickness with the pre-instability thickness in calculating the liquid film aspect ratio α.

Figure 2. 15(a) shows all of our experimental and numerical simulation conditions on the previous flow regime map. All of our cases would be in the RP regime according to this regime map. Figure 2. 15(b) shows our new flow regime map, which can now capture the transition to the isolated droplet regime. The film aspect ratios for flows in the isolated bead regime, where there is no well-defined pre-instability region, are calculated using "equivalent" pre-instability thickness values using the relation discussed later.

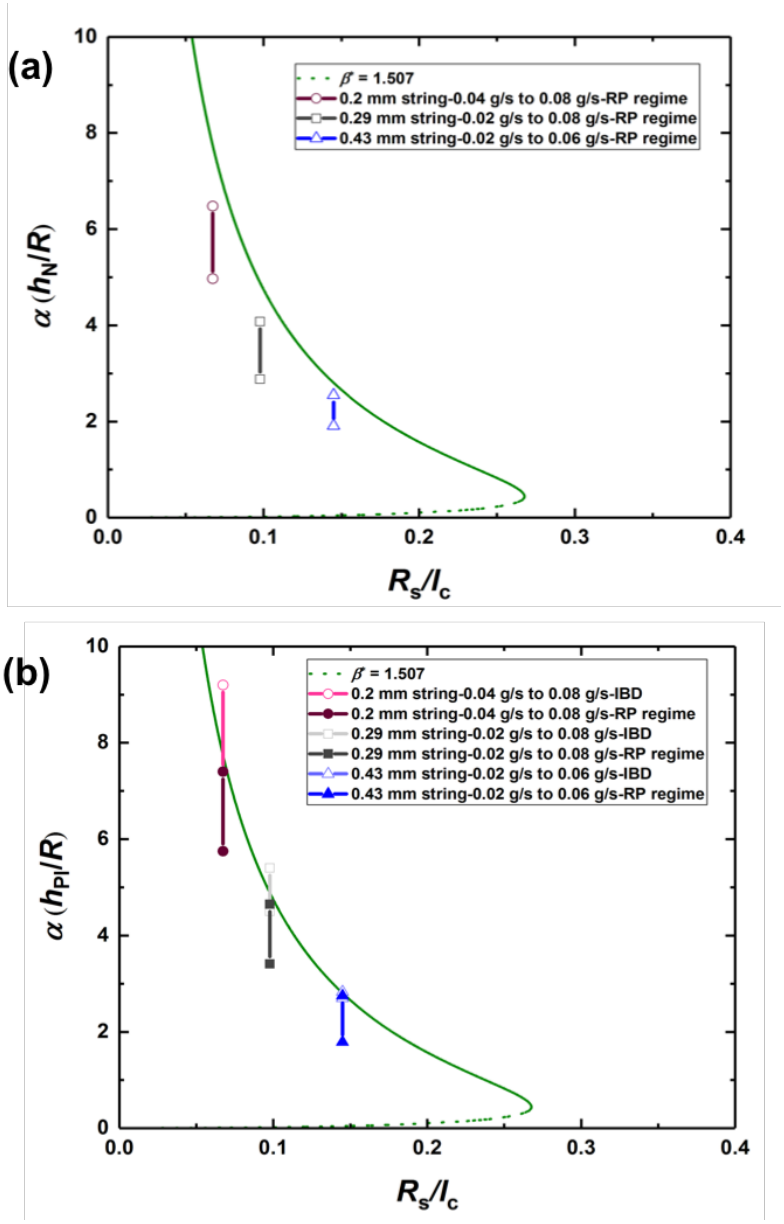

Figure 2. 15: (a) The flow regime map proposed in previous studies. The Nusselt thickness is used to define the liquid film aspect ratio α. (b) The newly proposed flow regime map. The pre-instability thickness is used instead to define α.

We propose an inter-relationship between the flow parameter. In this method, the bead diameter can be calculated using the pre-instability thickness and the bead velocity and frequency are found by the bead diameter value. The spacing, which is the division of the bead velocity and

frequency, then, can be calculated. Based on these inter-relationships and a simplified free body diagram of a liquid bead on a vertical string, we develop semi-empirical models to help calculate the flow parameters from the pre-instability thickness (see Figure 2. 16 and Figure 2. 17).

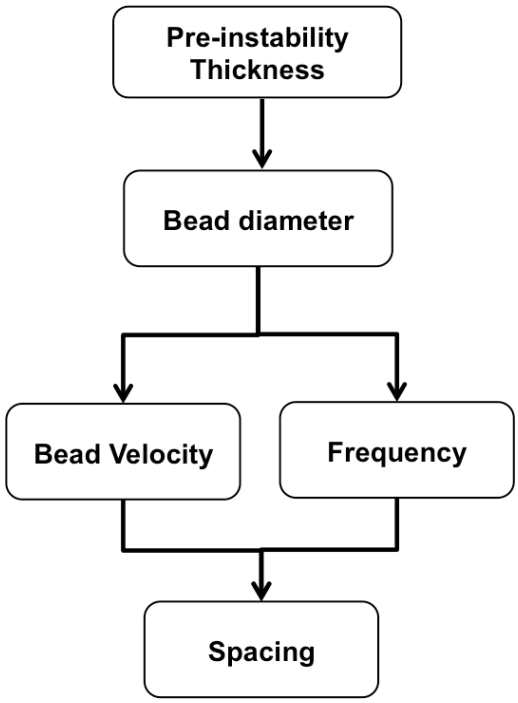

Figure 2. 16: The inter-relations between the flow parameters.

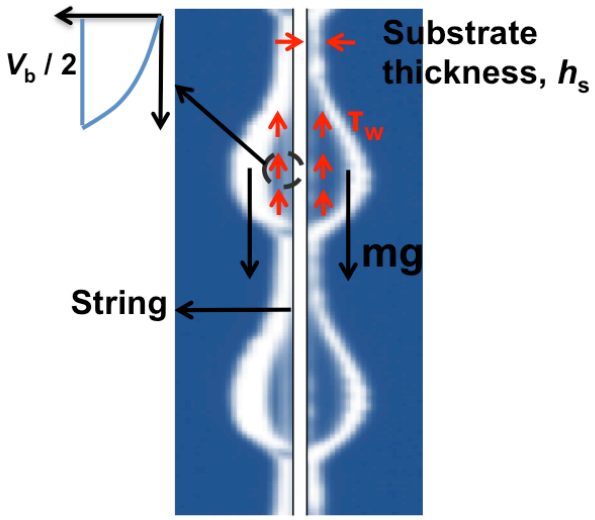

Figure 2. 17: A simplified free body diagram of a liquid bead flowing down a vertical string. Note that parts of the string between liquid beads are surrounded by thin liquid substrates.

Based on our experimental results, we first develop an empirical correlation between the liquid bead diameter D_b and the pre-instability thickness h_{PI}:

$$\frac{D_b}{2} = 1.45 h_{PI} + \frac{D_s}{2} \tag{2.1}$$

Figure 2. 18 shows that the bead diameters calculated using our empirical model agree well with the experimental data. There is an approximately linear relationship between the pre-instability thickness and the liquid bead diameter. As a result, the limiting pre-instability thickness results in a corresponding limit for the bead diameter as illustrated in Figure 2. 18.

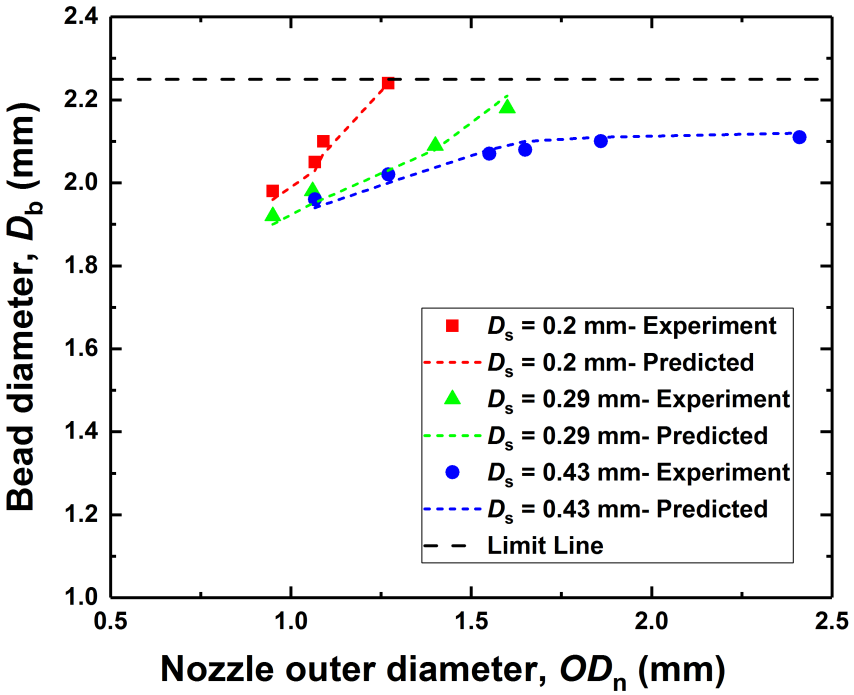

Figure 2. 18: The liquid bead diameter as a function of the nozzle outer diameter. The solid symbols represent the experimental data and the dashed lines correspond to the values calculated from the empirical model. The liquid mass flow rate is 0.06 g/s. The limit line corresponds to the limit line of pre-instability diameter.

Next, we model a liquid bead as a rigid object sliding down on a thin liquid substrate. Based on our numerical simulation results, we approximate the velocity of the liquid at the surface of the substrate as half the bead velocity, $V_b/2$, and the liquid substrate thickness as $\frac{h_{PI}}{h_N} \times R_b$. From the force balance, we then derive the following semi-empirical equation for the bead velocity, V_b :

$$V_b = \frac{h_{PI}}{h_N} \frac{\rho g R_s \left[\frac{2}{3} R_s^2 - \left(R_s \left(\frac{h_{PI}}{h_N} + 1 \right) \right)^2 \right]}{\mu R_s \left(\frac{h_{PI}}{h_N} + 1 \right)} \tag{2.2}$$

The liquid bead velocities calculated from the semi-empirical model agree well with the measured values (see Figure 2. 19). We note that, as the pre-instability diameter increases with decreasing string diameters, the bead velocity also increases. This can be explained by the fact that liquid beads formed from thicker pre-instability regions are bigger. Since the bead volume and corresponding gravity force grow faster (~ D_b^3) than the viscous force on the inner side of the sliding bead (~D_b^2), the bead velocity increases with the pre-instability thickness.

The bead frequency f can be readily calculated from the mass flow rate and the mass of an individual liquid bead. We first obtain the part of the mass flow rate contributed by liquid beads by subtracting the part of the mass flow rate contributed by the liquid substrate from the total mass flow rate. The liquid bead is assumed to be a sphere of diameter D_b. We then obtain:

$$f = \frac{Q}{\rho\left(\frac{2}{3}\pi R_b^{\,3} - 2\pi R_b R_s^{\,2}\right)} \tag{2.3}$$

The liquid bead frequency decreases with increasing pre-instability thicknesses (due to either increasing nozzle outer diameter or decreasing string diameter) because of the corresponding increase in the diameter of liquid beads and hence their mass (see Figure 2. 20). The liquid bead frequency needs to decrease to maintain the same liquid flow rate. The bead spacing can be obtained by simply dividing the liquid bead velocity by the bead frequency.

Moreover, as an increase in the bead diameter leads to an increase in the bead velocity and a decrease in the bead frequency to satisfy the mass conservation, the limiting value of the bead diameter translates into a corresponding upper limit for the bead velocity (see Figure 2. 19) and a

corresponding lower limit for the bead frequency (see Figure 2. 20). We emphasize that these limiting values represent limits for liquid film flows to stay in the Rayleigh-Plateau regime and not other physical limits.

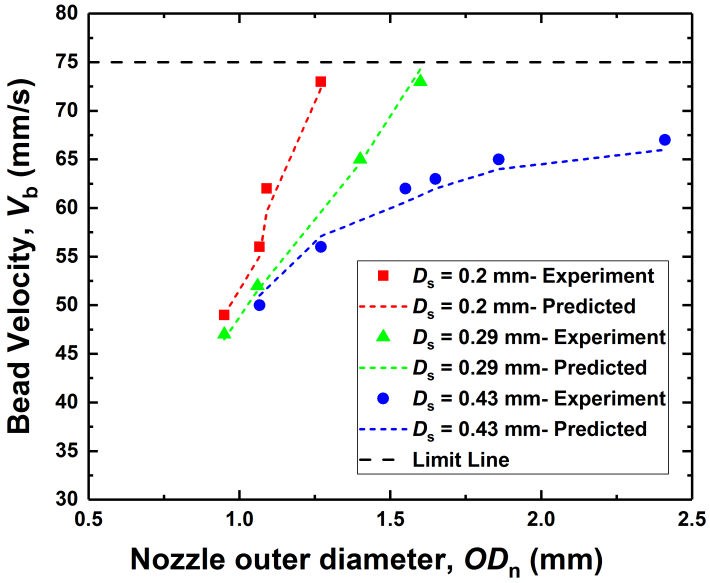

Figure 2. 19: The liquid bead traveling velocity as a function of the nozzle outer diameter. The solid symbols correspond to the experimental results obtained using three different string diameters. The dashed lines correspond to the values calculated using the semi-empirical model. The limit line corresponds to the limit line of bead diameter.

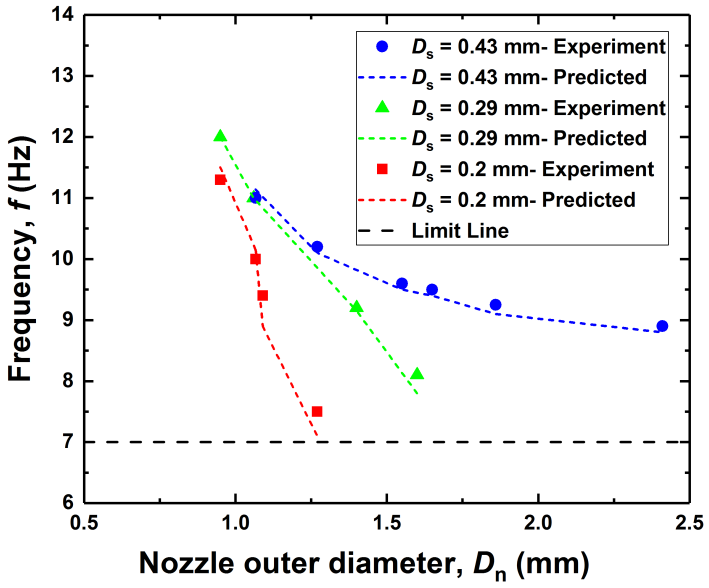

Figure 2. 20: The liquid bead frequency as a function of the nozzle outer diameter. The solid symbols correspond to the experimental results obtained using three different string diameters. The dashed lines correspond to the values calculated using the semi-empirical model. The limit line corresponds to the limit line of bead diameter.

Earlier studies[16], [62] related the liquid bead spacing to the dominant wavelength for instability, $2\pi 2^{1/2}h$, in cylindrical liquid columns. This result, however, was obtained for static liquid films whose thicknesses are much smaller than the string radius. These conditions do not strictly apply in flowing liquid films considered in the present study. The classical relationship indeed does not directly capture the relationship between the bead spacing and the flow rate ($S_b \sim Q^{-1}$) illustrated, for example, in Figure 2. 11. Our semi-analytical models (Eqs. 2.2 and 2.3), however, do suggest that the bead spacing, S_b, is linearly related to the pre-instability thickness, h_{PI}. Comparing bead spacing results in Figure 2. 11 and the corresponding pre-instability diameters, we also generally note an approximately linear dependence of the bead spacing on the pre-instability diameter (see Figure 2. 13).

2.4 Summary

We report our experimental and numerical simulation study on the effects of nozzle geometry on the characteristics of thin liquid films flowing down vertical strings with diameters of 0.2, 0.29 and 0.43 mm under the ranges of liquid flow rates (0.02, 0.04, 0.06 and 0.08 g/s) where the Rayleigh-Plateau instability is the dominant instability mechanism. The nozzle inner diameters are varied from 0.5 to 3.2 mm. We identify that the portion of a liquid film near the nozzle, which precedes the onset of the instability, as a key to the down-stream flow characteristics, such as the liquid bead size, spacing, and traveling speed. The thickness of a nearly flat part of this pre-instability region is termed the pre-instability thickness, which differs from the Nusselt thickness often presumed in the literature. We show that an increase in the nozzle diameter at a fixed mass flow rate leads to an increase in the pre-instability thickness. This in turn results in increases in the liquid bead size, spacing, and traveling velocity. With an increase in the liquid mass flow rate, a decrease in the string diameter, or an increase in the liquid viscosity, the pre-instability thickness grows, approaching a limit before the film flow transitions into a different flow regime. This transition is captured in a modified flow regime map where we replace the Nusselt thickness with the pre-instability thickness to define the film aspect ratio. Semi-empirical models are also developed for the liquid bead size, spacing, and traveling speed as a function of the pre-instability thickness.

CHAPTER 3

Influence of nozzle geometry on thin film dynamics flowing down a cylinder

We present a study of the effects of nozzle geometry on the dynamics of thin fluid films flowing down a cylindrical fiber. Recent experiments have shown that varying nozzle diameters can lead to different flow regimes and droplet characteristics in the film. Using a weighted residual modeling approach, we investigate a system of coupled equations that include inertia, surface tension effects, gravity, and a film stabilization mechanism. This model characterizes both near-nozzle fluid structure and downstream bead dynamics. We report a remarkable agreement between the predicted droplet properties and the experimental data.

3.1 Background

The dynamics of thin fluid films flowing down a cylindrical fiber plays a significant role in a variety of engineering applications, including mass and heat exchangers, desalination, and water vapor capturing. Primarily governed by the Rayleigh-Plateau instability and gravity modulation, the complex interfacial dynamics of the film involve the droplet formation, moving bead of constant speeds, and irregular wave patterns.

Three distinct flow regimes have been observed from previous experiments Kliakhandler et al. [49]: (a) convective regime where irregular wave patterns frequently lead to droplet collisions;

(b) Rayleigh-Plateau regime where stable traveling beads move at a constant speed, and (c) isolated droplet dripping regime where widely spaced traveling beads coexist with secondary small-amplitude wave patterns. These dynamical regimes have been extensively studied both experimentally and theoretically[16], [54], [63], [64] based on the flow rate, fiber radius, and the fluids used in the experiments.

A recent study by Sadeghpour et al.[65] revealed that the nozzle geometry also has a strong influence in the dynamic regime of the downstream flows. Specifically, distinct regimes of interfacial patterns were observed when only the diameter of the nozzle feeding the fluid is varied. These results motivate us to further investigate the existing models to better characterize the physics involved in the interfacial dynamics both near the nozzle and further downstream. An improved understanding of the flow regimes is also expected to assist systematic optimization of a variety of engineering applications.

For small flow rate cases, the classical lubrication theory has been widely applied to the dynamics of films flowing down vertical fibers. Under the assumption that the film thickness is much smaller than the fiber radius. Weakly nonlinear thin film equations have been extensively studied by Frenkel [66]; Chang & Demekhin [67]; Kalliadasis & Chang [17]. These single evolution equations for the film thickness characterize both stabilizing and destabilizing roles of the surface tension that originate from axial and azimuthal curvatures of the interface, respectively Craster & Matar [68]. A fully nonlinear curvature term is incorporated in Kliakhandler et al. [49] which alleviates the small-interface-slope assumption of the lubrication theory. Using a low-Bond-number, surface-tension-dominated theory, Craster & Matar [51] proposed an asymptotic (CM)model which captures the flow regimes (a) and (c).

Recently, Ji et al. [69] investigated a full lubrication model that includes slip boundary conditions, nonlinear curvature terms, and a film stabilization term. The film stabilization term brings to focus the presence of a stable liquid layer which plays an important role in the full dynamics. Compared to previous studies, the combination of these physical effects better characterizes the observed propagation speed, stability of traveling droplets, and their transition to isolated droplet regime.

For moderate flow rate cases, Trifonov et al. [14] firstly proposed a system of coupled evolution equations for the film thickness and the flow rate. This model incorporates inertia effects based on the integral boundary layer (IBL) equations for the dynamics of a falling film on inclined planes Shkadov [70]. Weighted residual integral boundary-layer(WRIBL) models developed by Ruyer-Quil et al. [19]; Duprat et al. [18]; Ruyer-Quil & Kalliadasis [54] further extended the IBL models by including contributions of the streamwise viscous diffusion.

In this study, we present a study of the influence of nozzle geometry in the dynamics of liquid films flowing down vertical fibers. Our model builds on previous studies of integral boundary-layer equations and the film stabilization mechanism, and accounts for inertia effects, gravity modulation, and surface tension. The paper is organized as follows. In section 3.2 we lay out the experimental setup. In section 3.3 a system of coupled evolution equations for the film thickness and the flow rate is formulated. Section 3.4.1 presents the stability analysis of the model and discusses the film stabilization term. Numerical results for the model and their comparison against experimental observations are presented in section 3.4.2, followed by concluding remarks in section 3.5.

3.2 Experimental setup

Figure 3. 1(A) shows a schematic of the experimental setup. This setup was designed to investigate the effect of nozzle on the flow properties as well as the flow pattern. As shown in Figure 3. 1(A), the experimental setup includes: 1) a syringe pump to control the volume flow rate of the working liquid, (2) a convertor to connect the syringe pump outlet to the nozzle, (3) a stainless steel nozzle with various diameters (*OD* = 0.84, 1.06, 1.27, 1.56, 1.86, or 2.41), (4) a transparent tube to protect the flow from noise and air disturbances, (5) a high-speed camera, set to 1000 frame/second, mounted on an adjustable stage, (6) a weight connected to the end of the polymer fiber to keep it straight and vertical during the experiment, (7) a weight scale, (8) a liquid container and (9) a data acquisition system to receive/record the information from the camera and the weight scale.

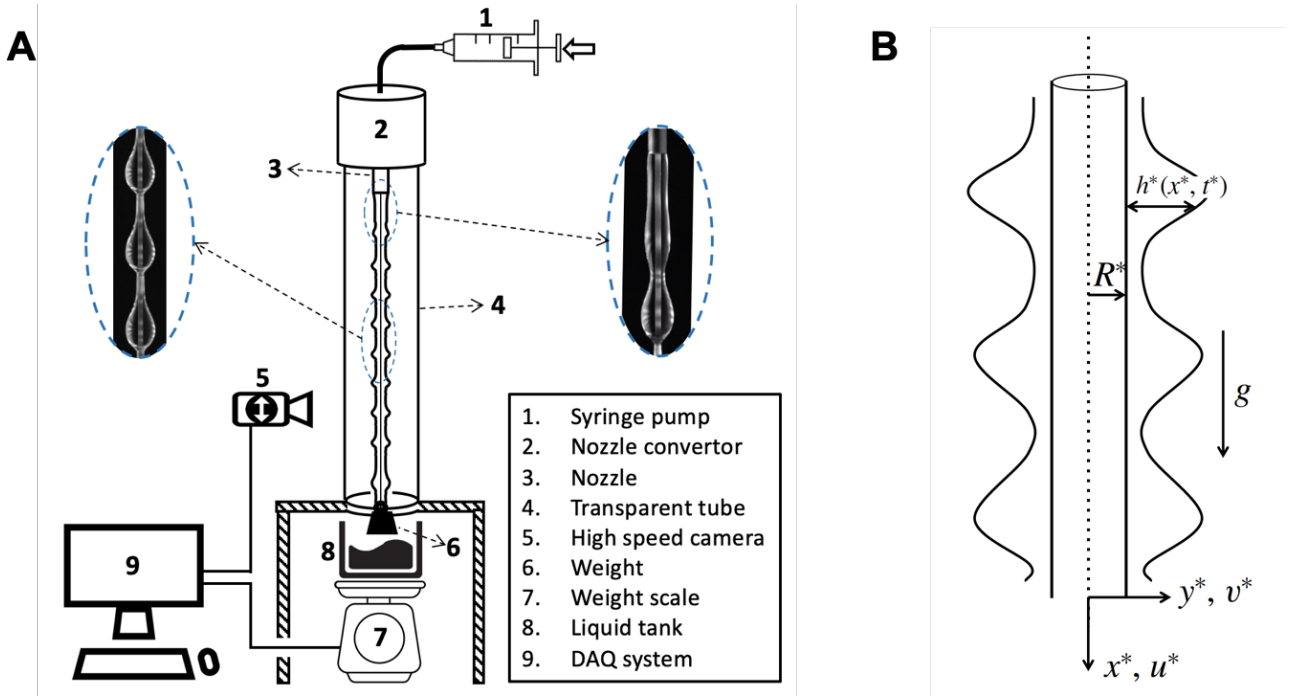

Figure 3. 1: (A) Schematic of the experimental setup with changeable nozzle to study the effect of nozzle on the fluid dynamics of the flow, and (B) schematic of a thin liquid film flowing down a vertical cylindrical fiber with variable names.

Polymer based fibers with diameters of 0.2, 0.29, and 0.41 mm were used in the experiments with the liquid mass flow rate in the range of 0.02g/s to 0.08g/s. Rhodorsil silicone oil v50, a known well-wetting liquid, with the following physical properties was used in this work: density $\rho = 963$ kg/m^3, kinematic viscosity $\nu = 50$ mm^2/s, surface tension $\gamma = 20.8$ mN/m (all at 20 °C). A summary of the experimental cases in this manuscript is presented in Table 3. 1.

Table 3. 1: A summary of the experimental cases

Fiber diameter, D_s [mm]	Nozzle outer diameter, OD [mm]	Mass flowrate, Q_m [g/s]
0.2	0.84, 1.06, 1.27, 1.56, 1.86, 2.41	0.04 0.08
0.29	0.84, 1.27, 1.56, 1.86, 2.41	0.04 0.08
0.43	0.84, 1.06, 1.27, 1.56, 1.86, 2.41	0.02 0.06

3.3 Model formulation

We consider a flow of two-dimensional axisymmetric Newtonian fluid down a vertical cylinder of radius R^* (see Figure 3. 1(B)). The liquid properties, including the surface tension, σ, density, ρ, and kinematic viscosity, ν, are all assumed to be constant. This model formulation does not include the nozzle size as a system parameter because we are interested in the flow downstream

where the nozzle does not affect the dynamics. Instead, we consider the scales for frequency and mass of the droplets, which depend on the nozzle size (Sadeghpour et al. [65]). We will discuss this dependence later in appendix B. We review below the derivation of the governing equations and boundary conditions by Ruyer-Quil et al. [19] and Craster & Matar [51] and discuss our inclusion of additional physics related to slip, curvature and wetting properties.

The dimensional Navier–Stokes equations for axisymmetric flows are:

$$u^*_{t^*} + u^* u^*_{x^*} + v^* u^*_{y^*} = -\frac{1}{\rho}\left(p^*_{x^*} + \Pi^*_{x^*}\right) + g + \nu\left(u^*_{x^*x^*} + \frac{u^*_{y^*}}{y^*} + u^*_{y^*y^*}\right) \tag{3.1}$$

$$v^*_{t^*} + v^* v^*_{y^*} + u^* v^*_{x^*} = -\frac{p^*_{y^*}}{\rho} + \nu\left(v^*_{x^*x^*} + \frac{v^*_{y^*}}{y^*} + v^*_{y^*y^*} - \frac{v^*}{y^{*2}}\right) \tag{3.2}$$

where t^* represents the time, u^* and v^* represent the axial and radial components of the velocity, p^* is the pressure and g is the gravitational acceleration.

The equation of continuity is given by

$$v^*_{y^*} + \frac{v^*}{y^*} + u^*_{x^*} = 0 \tag{3.3}$$

Along the fiber, at the interface between the solid substrate and the fluid $y^* = R^*$, we impose the Navier slip and no-penetration boundary conditions:

$$v^* = 0, \qquad u^* = \lambda^* u^*_{y^*} \qquad \text{at} \quad y^* = R^* \tag{3.4}$$

where $\lambda^* > 0$ is the slip length in standard slip models [71], [72].The no-slip boundary condition corresponds to $\lambda^* = 0$. Typical slip lengths for polymeric liquids such as silicone oil range from 1

to 10 mm [15], [73]. The normal and shear stress balances on the free surface $y^* = R^* + h^*$ are given by

$$p^* = \frac{2\mu}{1+h_{x^*}^{*2}}\left[h_{x^*}^{*2}u_{x^*}^* - h_{x^*}^*\left(v_{x^*}^* + u_{y^*}^*\right) + v_{y^*}^*\right] + \frac{\sigma}{\left(1+h_{x^*}^{*2}\right)^{3/2}}\left(\frac{1+h_{x^*}^{*2}}{R^*+h^*} - h_{x^*x^*}^*\right) \tag{3.5}$$

$$\left(1+h_{x^*}^{*2}\right)\left(v_{x^*}^* + u_{y^*}^*\right) + 2h_{x^*}^*\left(v_{y^*}^* - u_{x^*}^*\right) = 0 \tag{3.6}$$

where μ is the dynamic viscosity, and σ scales the total curvature which consists of a destabilizing azimuthal curvature term and a stabilizing axial curvature term. We then complete the system by including the kinematic boundary condition on the free surface $y^* = R^* + h^*$,

$$h_{t^*}^* + u^* h_{x^*}^* = v^* \quad \text{at} \quad y^* = R^* + h^* \tag{3.7}$$

The next step is to choose the appropriate dimensionless parameters to non-dimensionalize the model. Following Duprat et al., we choose the scales for the system as follows: the length scale in the radial direction y is $\mathcal{H}$, and the length scale in the streamwise direction x is $\mathcal{L} = \mathcal{H}/\epsilon$ [18]. The scale ratio ϵ is set by the balance between the surface tension term $\sigma h^*{}_{x^*x^*x^*}$, arising from $p^*{}_{x^*}$, and the gravity, g, and is given by $\epsilon = (\rho g \mathcal{H}^2/\sigma)^{1/3}$. This scale ratio is small (around 0.4) in typical experiments and can also be rewritten as $\epsilon = We^{-1/3}$, where the Weber number $We = \mathcal{L} = (l_c/\mathcal{H})^2$ compares the capillary length $l_c = \sqrt{\sigma/\rho g}$ to the radial length scale $\mathcal{H}$. Then the characteristic streamwise velocity is $U = (g\mathcal{H}^2)/\nu$, and the pressure and time scales are given by $\rho g \mathcal{L}$ and $(\nu\mathcal{L})/(g\mathcal{H}^2)$, respectively. In order to apply the lubrication approximation, we assume that $\epsilon \ll 1$, $\epsilon^2 \mathrm{Re} = O(1)$, where the Reynolds number $\mathrm{Re} = (U\mathcal{L})/\nu$. With these scales, we drop

the star superscripts and write the mentioned equations in new forms. The leading-order non-dimensional momentum and continuity equations are:

$$\hat{U}^2 \,\mathrm{Re}\left(u_t + uu_x + vu_y\right) = -p_x - \Pi_x + 1 + \frac{u_y}{y} + u_{yy} \tag{3.8}$$

$$0 = -p_y \tag{3.9}$$

$$v_y + \frac{v}{y} + u_x = 0 \tag{3.10}$$

Following the approach discussed in Ji et al. (2019), we include a film stabilization term $\Pi\,(h)$, which takes the functional form of the disjoining pressure widely used in characterizing wetting dynamics of thin fluid films (see Reisfeld & Bankoff [74])

$$\Pi(h) = -\frac{A}{h^3} \tag{3.11}$$

where A is a stabilization parameter. Along the fiber at $y = R$, we apply the no-slip and no-penetration conditions on the velocity

$$u = v = 0 \quad \text{at} \quad y = R \tag{3.12}$$

At the free surface, $y = h + R$, the balances of tangential and normal stresses are

$$u_y = 0 \quad \text{at} \quad y = h + R \tag{3.13}$$

$$p = \frac{\beta}{\alpha\left(1+\alpha h\right)} - h_{xx} \quad \text{at} \quad y = h + R \tag{3.14}$$

where $\alpha = \mathcal{H}/R^*$ represents the aspect ratio of the characteristic film thickness and the fiber radius, and the scaling parameter $\beta = \alpha^2/\epsilon^2$. The right-hand-side of previous equation characterizes the interaction between the destabilizing azimuthal curvature and the stabilizing streamwise curvature terms. The kinematic boundary condition at $y = h + R$ is given by

$$h_t + uh_x = v \quad \text{at} \quad y = h + R \tag{3.15}$$

Following Trifonov et al. and Duprat et al. [14], [18] we impose an assumption on the velocity profile

$$u(x, y, t) = a(x, t)u_0(y) + O(\text{Ú}) \tag{3.16}$$

where

$$u_0(y) = -\frac{1}{4}\left(y^2 - R^2\right) + \frac{1}{2}\left(h + R\right)^2 \ln\left(\frac{y}{R}\right) + O(\text{Ú}) \tag{3.17}$$

is the velocity of a uniform Nusselt flow without interfacial variance in the streamwise direction and satisfies the following two equations:

$$1 + \frac{\partial^2 u_0}{\partial y^2} + \frac{1}{y}\frac{\partial u_0}{\partial y} = 0 \tag{3.18}$$

$$\frac{\partial u_0}{\partial y} = 0 \quad \text{at} \quad y = h + R, \qquad u_0 = 0 \quad \text{at} \quad y = R \tag{3.19}$$

It is convenient to define a local flux, q, which represents the flow rate per unit circumference length, and a Nusselt flux q_0 for the flow rate of the Nusselt flow,

$$q \equiv \frac{1}{R}\frac{\partial}{\partial x}\int_R^{R+h} uy dy, \qquad q_0 \equiv \frac{1}{R}\frac{\partial}{\partial x}\int_R^{R+h} u_0 y dy = \frac{h^3}{3}\phi(\alpha h) \tag{3.20}$$

where the shape factor, ϕ, is a function defined by

$$\phi(X) = \frac{3}{16X^3}\left[(1+X)^4\left(4\log(1+X)-3\right)+4(1+X)^2-1\right] \tag{3.21}$$

Equation (3.20) is also useful in determining the characteristic length-scales. Given a dimensional volumetric mass flow rate Q_m^* and fiber radius R^*, the volumetric flow rate per circumference unit $q_0^* = Q_m^*/(2\pi\rho R^*)$. Then one obtains the characteristic axial length scale $\mathcal{H}$ for a uniform Nusselt flow from equation (3.20).

Omitting the higher-order terms in the expansion (3.16), multiplying both sides by y, we obtain the relation between the local flux, q, and the Nusselt flux, q_0, $q(x, t) = a(x, t)\, q_0$. This leads to $a(x, t) = q/q_0 = 3q/[h^3\phi(\alpha h)]$. Besides, by integrating the continuity equation across the film from $y = R$ to $y = R+h$, and using equations (3.12) and (3.15), we obtain a mass conservation equation for h in terms of the local flux, q,

$$\frac{\partial h}{\partial t} = -\frac{1}{1+\alpha h}\frac{\partial q}{\partial x} \tag{3.22}$$

Following a projection-based approach used in Ruyer-Quil et al. [19], we take the inner product of the streamwise momentum equation and $u_0(y)y$ from $y = R$ to $y = R + h$ $(x; t)$ and obtain

$$\int_R^{R+h}\left(\hat{U}\,\mathrm{Re}\left(u_t+uu_x+vu_y\right)+p_x+\Pi_x+1-\frac{u_y}{y}-u_{yy}\right)u_0 y dy = 0 \tag{3.23}$$

From (3.14) the pressure p is a function of only x and t. To simplify the averaged momentum equation (3.23), we apply the approximation for the velocity profile in (3.16), equations (3.10), (3.11) and the boundary conditions (3.12), (3.13), and (3.14).

Finally, we rescale the time and flux using $t = \tilde{t}/\phi(\alpha), q = Q\phi(\alpha)$. Using these new variables and dropping the tildes, we obtain the averaged axial momentum equation for the flux q:

$$\delta\frac{\partial q}{\partial t} = \delta\left[-F(\alpha h)\frac{q}{h}\frac{\partial q}{\partial x} + G(\alpha h)\frac{q^2}{h^2}\frac{\partial h}{\partial x}\right] + \frac{I(\alpha h)}{\phi(\alpha h)}\left[-\frac{3\phi(\alpha)}{\phi(\alpha h)}\frac{q}{h^2} + h\left\{1 - \frac{\partial}{\partial x}\left[Z(h) - \frac{\partial^2 h}{\partial x^2}\right]\right\}\right] \quad (3.24)$$

The coefficient functions in the averaged momentum equations are given below, where $b = 1 + X$:

$$\phi(X) = \frac{3}{16X^3}\left[(1+X)^4\left(4\log(1+X) - 3\right) + 4(1+X)^2 - 1\right] \quad (3.25)$$

$$I(X) = \left[64X^5\phi(X)^2\right]/\left[3F_b(X)\right] \quad (3.26)$$

$$F(X) = \left[3F_a(X)\right]/\left[16X^2\phi(X)F_b(X)\right] \quad (3.27)$$

$$G(X) = \left[G_a(X)\right]/\left[64X^4\phi^2(X)F_b(X)\right] \quad (3.28)$$

$$G_a(X) = 9b[4\ln(b)(-220b^8 + 456b^6 - 303b^4 + 6\ln(b)(61b^6 - 69b^4 + 4\ln(b)(4\ln(b)b^4 - 12b^4$$
$$+7b^2 + 2)b^2 + 9b^2 + 9)b^2 + 58b^2 + 9)b^2 + (b^2 + 1)^2(156b^6 - 145b^4 + 53b^2 - 1)) \quad (3.29)$$

$$F_a(X) = -301b^8 + 622b^6 - 441b^4 + 4\log(b)(196b^6 - 234b^4 + 6\log(b)[16\log(b)b^4 - 36b^4$$
$$+22b^2 + 3]b^2 + 78b^2 + 4)b^2 + 130b^2 - 10 \quad (3.30)$$

$$F_b(X) = 17b^6 + 12\log(b)\left[2\log(b)b^2 - 3b^2 + 2\right]b^4 - 30b^4 + 15b^2 - 2 \quad (3.31)$$

and δ is a reduced Reynolds number defined as

$$\delta = \hat{\mathrm{U}} \, \mathrm{Re}\, \phi(\alpha) \tag{3.32}$$

The functional Z consists of the azimuthal curvature term and the film stabilization term

$$Z(h) = \frac{\beta}{\alpha(1+\alpha h)} + \frac{A}{h^3} \tag{3.33}$$

The mass conservation equation (3.22) remains unchanged after the rescaling. This choice of time and flux scales leads to a normalized flux $q = 1/3$ for the flat film thickness $h = 1$.

The coupled system of evolution equations for the film thickness, h, and the flux, q, accounts for the surface tension, gravity, azimuthal instabilities and moderate inertia effects. For $A = 0$, this model is consistent with the first-order weighted residual boundary layer model studied in Ruyer-Quil et al. [19] and Duprat et al. [18] except that their model includes a fully nonlinear azimuthal curvature term $Z = Z_{\mathrm{FCM}}$,

$$Z_{FCM}(h) = \frac{\beta}{\alpha(1+\alpha h)} + \frac{\alpha h_x^{\,2}}{2\left(1+\alpha h\right)} \tag{3.34}$$

In the low Reynolds number limit, $\delta \to 0$, or by setting $\partial q/\partial t \equiv 0$, equation 3.24 gives an expression for q in terms of h. Substituting this expression into equation (3.22) leads to a single lubrication equation (3.35) for h which is equivalent to the model studied in Ji et al. [69] and Craster & Matar [51],

$$\frac{\partial}{\partial t}\left(h + \frac{\alpha}{2} h^2 \right) + \frac{\partial}{\partial x}\left(M(h)\left(1 - \frac{\partial}{\partial x}\left[Z(h) - \frac{\partial^2 h}{\partial x^2} \right] \right) \right) = 0 \tag{3.35}$$

where the $M(h) = h^3\phi(\alpha h)/[3\phi(\alpha)]$ is the mobility function. The form of $M(h)$ has also been generalized in our previous work to include Navier slip boundary conditions [69].

3.4 Results and Discussion

3.4.1 Stability analysis and film stabilization mechanism

Next, we examine the linear stability of the model (eqs 3.22-3.24), and derive the stabilization parameter A in (3.11). Similar to the film stabilization model studied in Ji et al. [69], $A > 0$ is important for the model to produce comparable downstream dynamics observed in experiments.

We perturb a uniform layer $h \equiv \bar{h}$ and its corresponding flux $q \equiv \bar{q}$ by

$$h = \bar{h} + \text{Ų}_0 H, \quad q = \bar{q} + \text{Ų}_0 \text{Q} \qquad \text{where} \quad \text{Ų}_0 \ll 1 \tag{3.36}$$

Substituting the expansion (3.36) into (3.24) leads to the $O(1)$ equation,

$$\bar{q} = \frac{\bar{h}^3 \phi(\alpha \bar{h})}{3\phi(\alpha)} \tag{3.37}$$

After obtaining a single equation for H by eliminating Q using (3.37), we apply the Fourier mode decomposition $H = H_1 exp(ikx + \lambda t)$, where the wave number k and the growth rate of the perturbation, λ, are both real. This yields the dispersion relation

$$0 = \delta\left(1+\alpha\bar{h}\right)\lambda^2 - \frac{\left(1+\alpha\bar{h}\right)I(\alpha\bar{h})}{\bar{h}^2\phi(\alpha\bar{h})}\lambda - k^2\left[\delta G(\alpha\bar{h})\frac{\bar{q}^2}{\bar{h}^2} + \frac{I(\alpha\bar{h})\bar{h}}{\phi(\alpha)}\left(\frac{\beta}{\left(1+\alpha\bar{h}\right)^2} - \frac{3A}{\bar{h}^4}\right)\right] + \frac{I(\alpha\bar{h})\bar{h}}{\phi(\alpha)}k^4 \tag{3.38}$$

Following the approach in Ji et al. [69], we select the stabilization parameter, A, based on the thickness of stable undisturbed layers obtained from experimental observations. Since the marginal stability is achieved for $\lambda = 0$ in (3.38), we derive a formula for $\tilde{A}$,

$$\tilde{A} = \frac{\beta \acute{U}_p^4}{3\left(1+\alpha \acute{U}_p\right)^2} + \frac{\delta \acute{U}_p^7 G(\alpha \acute{U}_p)\phi^2(\alpha \acute{U}_p)}{27 I(\alpha \acute{U}_p)\phi(\alpha)} \tag{3.39}$$

such that for $A = \tilde{A}$, any thin at lm of thickness less than the threshold value ϵ_p is linearly stable, that is, $\lambda < 0$, for all wave numbers. Compared to the film stabilization model introduced in our previous work [69], the formula (3.39) for $\tilde{A}$ includes a higher order term in ϵ_p.

3.4.2 Numerical studies on near nozzle dynamics

We perform numerical investigations to examine the spatio-temporal dynamics of the flow near the inlet and further downstream by solving the coupled system (3.3) for $0 \le x \le L$. To model the influence of nozzle geometry to the full dynamics, we impose Dirichlet boundary conditions on both the film thickness, h, and the flux, q, at $x = 0$: $h(0,t) = h_{IN}, q(0,t) = 1/3$, where the dimensionless inlet film thickness $h_{IN} = (0.5\,OD - R^*)/\mathcal{H}$, where OD represents the dimensional outer nozzle diameter. Following Ruyer-Quil et al. [19], we impose soft boundary conditions at the outlet by replacing the averaged momentum balance equation 3.41 with a linear

hyperbolic equation $q_t + \upsilon_f q_x = 0$ at the last two grid points near the outlet, where $\upsilon_f = 1$ is used for all the simulations.

The initial conditions are set to be a piece-wise linear profile for the film thickness, h, and a constant for the flux, q

$$q(x,0) \equiv \frac{1}{3}, \qquad h(x,0) = \begin{cases} 1, & x > x_L \\ h_{IN} + (1 - h_{IN})\, x / x_L, & 0 \le x \le x_L \end{cases} \tag{3.40}$$

where $x_L = 10$ is used for most simulations.

Centered finite differences in a Keller box scheme are used for numerically solving the model (eqs 3.22-3.24), where the coupled fourth-order PDE system is decomposed into a system of first-order differential equations:

$$\begin{aligned} & k = h_x, \qquad p = k_x, \qquad \left(h + \frac{a}{2} h^2 \right)_x + q_x = 0, \\ & \delta q_t = \delta \left(-F \frac{q}{h} q_x + G \frac{h^2}{q^2} k \right) + \frac{I}{\phi(\alpha)} \left[-3 \frac{\phi(\alpha)}{\phi(\alpha h)} \frac{q}{h^2} + h\left(1 - Z'(h) k + p_x\right) \right] \end{aligned} \tag{3.41}$$

In Figure 3. 2, we show plots of transient numerical results of model (eqs 3.22-3.24) that correspond to four experiments with varying outer nozzle diameters. Fixed flow rate $Q_m = 0.04$ g/s and fiber diameter $D_s = 0.29$ mm are used. The experimental results in Figure 3. 2(A) indicate that as the nozzle diameter increases from 0.84 mm to 1.27 mm, the droplet dynamics undergo a regime transition from the convective instability regime to a Rayleigh-Plateau regime. Moreover, within the Raleigh-Plateau regime, an enlarged nozzle diameter leads to larger spacing between the moving droplets. This regime transition is captured in the numerical simulation (see Figure 3. 2(B)) where the inter-bead spacing is in good agreement with experimental observations.

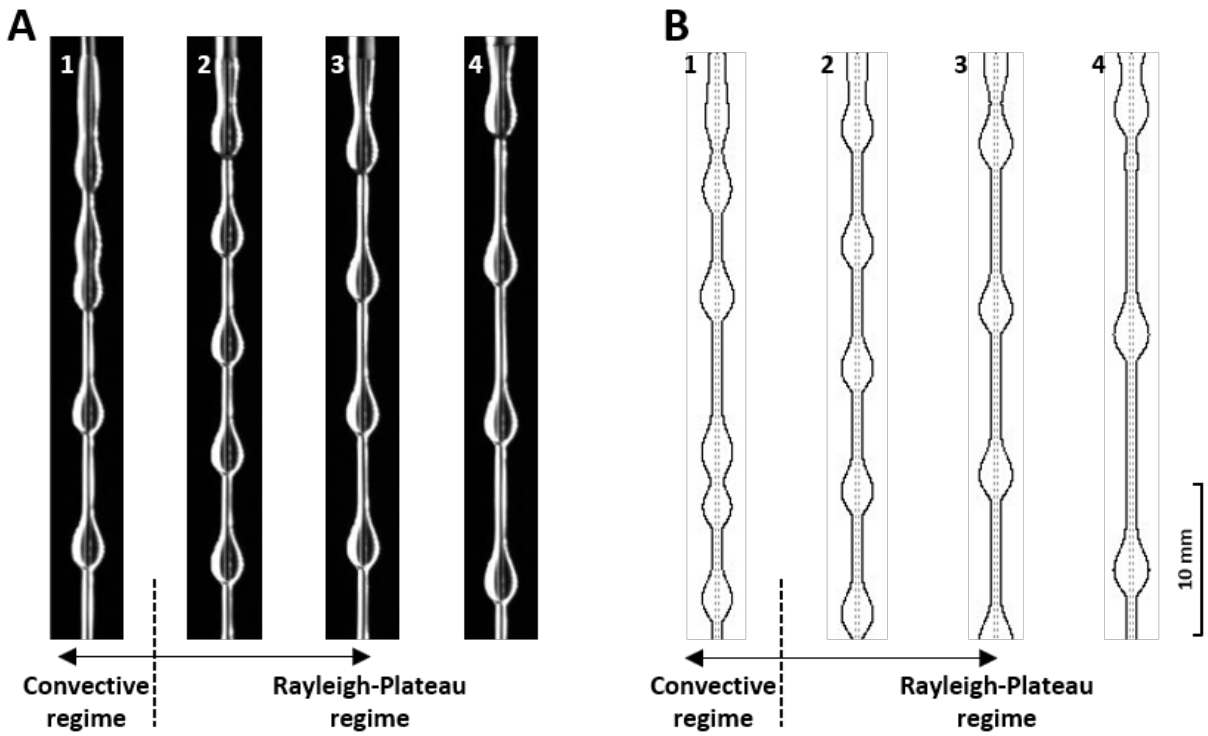

Figure 3. 2: Flow profile of Silicone oil v50 on a fiber with diameter of 0.29 mm, with liquid flow rate, Q_m, of 0.04 g/s, while varying the nozzle outer diameter (from left to right = 0.84, 1.56, 1.84, and 2.41 mm) obtained from (A) experiments, and (B) mathematical modeling with ϵ_p=0.15 mm.

Next, we discuss the influence of nozzle geometry on the dynamics of the flow within the healing length. Previous studies assumed that the film thickness and velocity profiles within the healing length are specified by the flow rate and fiber radius. However, our study reveals that for flows in convective and Rayleigh-Plateau regimes, the healing length decreases as the nozzle diameter increases. Figure 3. 3 presents one such comparison of the near-nozzle film profiles between experiments and simulations for flow rate Q_m = 0.06 g/s and fiber diameter D_s = 0.43 mm. This observation is similar to the study by Duprat et al. [18] who studied the spatial response of

the film to inlet forcing and concluded that the healing length tends to decrease as the forcing amplitude increases.

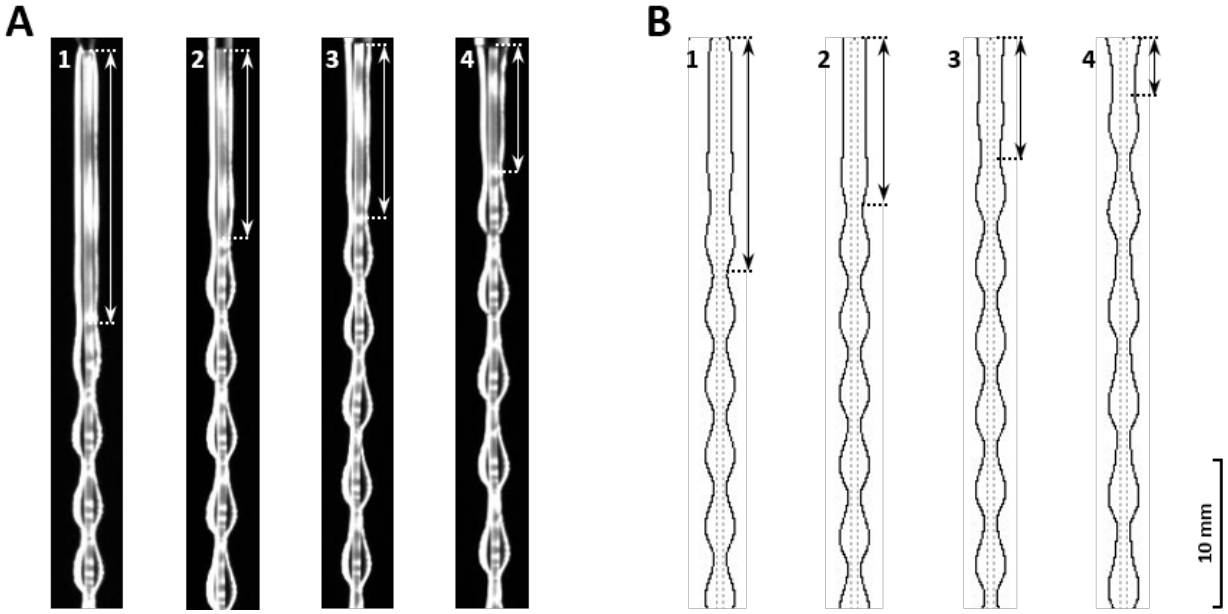

Figure 3. 3: Visualization of effect of nozzle outer diameter on the healing length (marked by arrows) for flow of silicone oil v50 on a fiber with diameter of 0.43 mm, with liquid flow rate, Q_{m}, of 0.06 g/s, while varying the nozzle outer diameter (from left to right = 0.84, 1.56, 1.84, and 2.41 mm) obtained from (A) experiments, and (B) mathematical modeling with ϵ_p=0.15 mm.

3.4.3 Experimental comparisons on bead properties

In Figure 3. 4, we show plots of predicted bead velocities, V_{b}, and inter-bead spacing, S_{b}, for varying nozzle sizes. The top through bottom panels indicate the cases of fiber diameters D_{s} = 0.2, 0.29, and 0.43 mm, with two choices of flow rate Q_{m} = 0.06 g/s for each fiber diameter. Our model (eqs 3.22-3.24) agrees quite well with the experimental observations across all cases when a suitable stable film thickness, ϵ_p, is applied.

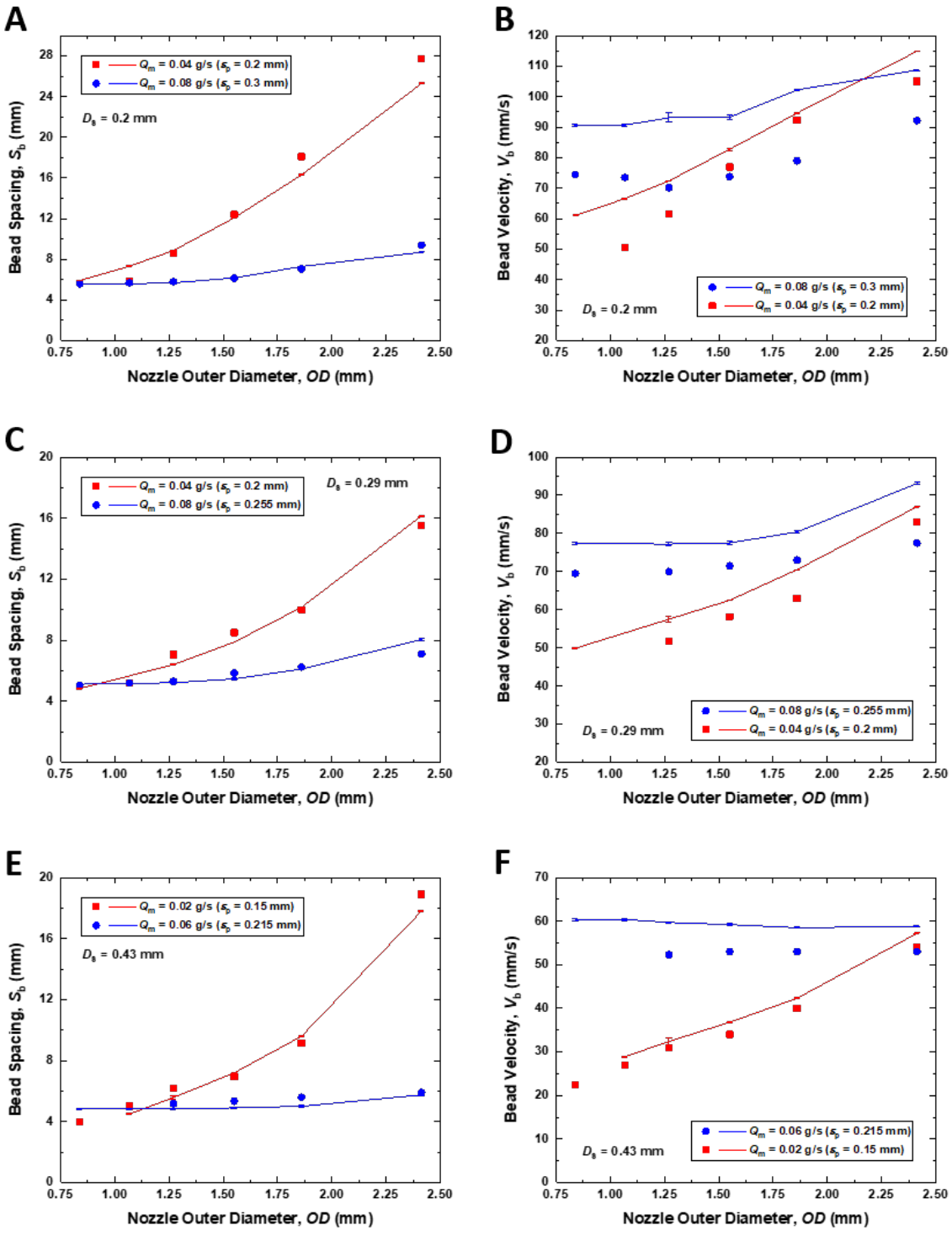

Figure 3. 4: Comparison of (A), (C), and (E) bead spacing and (B), (D), and (F) bead velocity from mathematical modeling results to the experiments as a function of nozzle outer diameter (0.84 mm to 2.41 mm) for the following cases, (A) and (B) fiber diameter = 0.2 mm and Q_m = 0.04 and

0.08 g/s, (C) and (D) fiber diameter = 0.29 mm and Q_m = 0.04 and 0.08 g/s, and (E) and (F) fiber diameter = 0.43 mm and Q_m = 0.02 and 0.06 g/s. symbols represent the experimental results and lines represent the mathematical modeling results.

The presence of the film stabilization term is important for maintaining the stable train of beads flowing down the fiber. In Figure 3. 5, we show the relation between the bead characteristics and the nozzle outer diameter OD as the stable film thickness, ϵ_p, varies. Since a larger value of the stabilization parameter, A, in equation (3.33) corresponds to stronger stabilization effects, increasing ϵ_p is expected to yield more stabilized moving beads. For a fiber diameter D_s = 0.43 mm at a small flow rate Q_m = 0.02 g/s, the film stabilization model with ϵ_p = 0.15 mm best captures both the bead profiles and moving velocity. While without the film stabilization mechanism (ϵ_p = 0 mm), large variations in the downstream bead characteristics are observed, which indicates that the model does not predict a stable train of moving beads.

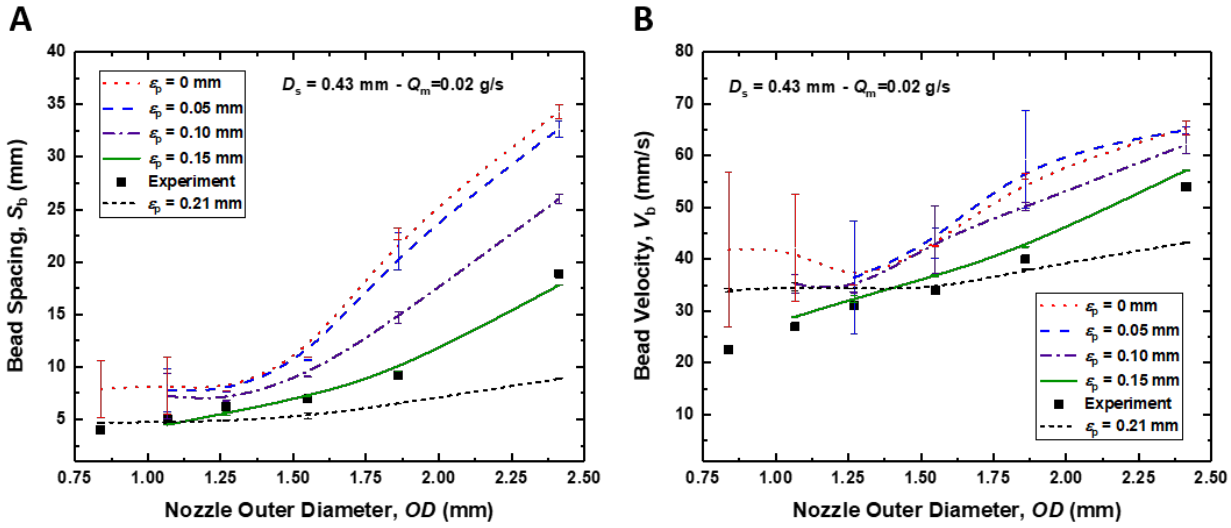

Figure 3. 5: Effect of ϵ_p on the (A) bead spacing, and (B) bead velocity as a function of nozzle outer diameter obtained from experiments and mathematical modeling for fiber diameter of 0.43

mm, and liquid flow rate, Q_m, of 0.02 g/s. Symbols represent the experimental results; dotted line, dashed line, dot-dashed line, solid line and short dashed line represent the ϵ_p= 0 mm, ϵ_p= 0.05 mm, ϵ_p = 0.10 mm, ϵ_p = 0.15 mm, and ϵ_p = 0.21 mm case from mathematical modeling, respectively.

Finally, we study the influence of inertia effects, nonlinear curvature terms, and the film stabilization term to the bead characteristics. Figure 3. 6 shows a comparison of the experimental bead spacing and velocity of downstream dynamics against those obtained from the Craster & Matar model (CM) in (3.35), the full curvature model with $Z(h)$ given by equation (3.34) and A = 0, the linear curvature model with $Z(h)$ given by equation (3.33) and A = 0, and the film stabilization model with $A > 0$. Whereas the different models all yield qualitatively reasonable trend as the nozzle size increases, the film stabilization model provides the best agreement with the experiment, while the other models over-estimate the bead spacing and velocity.

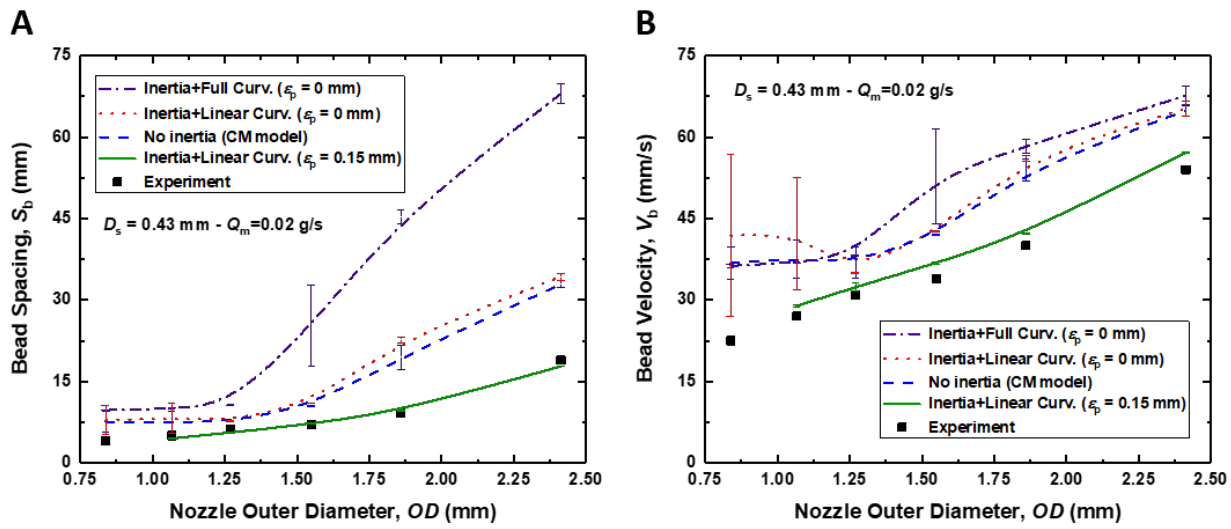

Figure 3. 6: Effect of nozzle diameter on the (A) bead spacing, and (B) bead velocity obtained from experiments and various mathematical modeling methods for fiber diameter of 0.43 mm, and liquid flow rate, Q_m, of 0.02 g/s. Symbols represent the experimental results; dot-dashed line, dotted line, dashed line, and the solid line represent mathematical modeling that includes inertia and full curvature with ϵ_p= 0 mm, inertia and linear curvature with ϵ_p= 0 mm, no inertia (CM model), and inertia and linear curvature with the best ϵ_p value (0.15 mm), respectively.

3.5 Summary

In summary, we have performed a detailed experimental and theoretical study of viscous flow down a vertical fiber, focusing on understanding the influence of nozzle diameter on the regime transition and downstream bead dynamics. We propose a boundary layer model that incorporates a film stabilization term to the pressure, and compare the predicted film dynamics against a range of experimental results. Numerical simulations show that in addition to fiber sizes and flow rates, the downstream flow regime transitions and bead characteristics are also affected by the nozzle geometry. Within the Rayleigh-Plateau regime, our results show outstanding experimental agreement in terms of bead spacing and velocity, and film profile within healing length near the

nozzle. We also compared our results with various theoretical methods, such as CM model, linear curvature model, full curvature model and various film stabilization terms.

CHAPTER 4

Water vapor capturing using an array of traveling liquid beads for desalination and water treatment

Growing concern over the scarcity of fresh water motivates development of compact and economic water vapor capture and condensation methods for distributed water treatment and harvesting. We report a study of water vapor in a warm humidified air condensing on cold liquid beads traveling down a massive array of vertical cotton threads acting as pseudo-superhydrophilic surfaces. These liquid beads are generated through intrinsic instability in thin films of water without requiring spray nozzles or electric excitation. They offer localized high-curvature surfaces that enhance vapor diffusion toward the liquid surface, a critical rate limiting step. With increasing liquid flow rates, the bead spacing decreases whereas the bead size and speed stay nearly constant. The resulting increase in the spatial bead density delivers mass transfer conductances and hence condensation rates per volume of 3 times higher than best reported values. Equally importantly, parallel and contiguous gas flow paths in our multi-string water vapor capturing device results in significant reduction in gas pressure drop and hence electric fan power consumption. Our compact, light-weight, and highly-effective device can serve as a critical enabler for distributed thermal desalination and vapor capture systems.

4.1 Background

Humidification and dehumidification (HDH) is an appealing thermal distillation technique for small-scale and mobile desalination and water treatment applications [24], [75] which imitates the natural rain cycle by creating humidified air (e.g., blowing dry air over a heated brine) and then condensing water vapor, using a water vapor capturing device (hereinafter referred to as "dehumidifier"), to produce distilled water. The critical technical challenge of HDH method lies in improving thermal energy efficiency. Past studies [76]–[79] proposed approaches to thermodynamically balancing humidification and dehumidification processes and reported designs with energy efficiency competitive with other technologies while delivering benefits of reduced capital and operation costs.

A practical limit in thermal efficiency, however, is posed by heat/mass exchange processes. Particularly problematic is dehumidification, which suffers from inherently large resistance to mass transfer experienced by water vapor as it diffuses through air. The deleterious effects of non-condensable gases on condensation has been well documented [80], [81]. Non-condensable gases of a volume fraction as low as 0.5% has been observed to cause as much as 50% reduction in condensation heat transfer.

Conventional approaches to condensation rely on cooled solid surfaces in contact with a gas stream, which is a mixture of the target vapor and other non-condensable gases. One can theoretically achieve high mass transfer rates by employing densely packed solid surfaces of large surface areas to reduce average distances vapor molecules must diffuse through. However, due to constraints on weight, cost, and/or manufacturability, solid surface areas per volume one can achieve are limited. Other methods, such as enhanced convective mixing through intermittent

liquid feeds [82] and electric winds generated by corona discharge [83], can enhance mass transfer but at the expense of increased power consumption and complexity. More recent studies adapted bubble columns for dehumidification [84] where humidified air is injected through a pool of cooled water to create bubbles with large surface-to-volume ratios for enhanced heat and mass transfer. The very large pressure head required to sustain air flows, however, again leads to increased electricity consumption.

In our recent paper [85], we reported an early demonstration of thin film flows of water along cotton threads and their potential application in evaporation/humidification. This early demonstration, however, was rather *ad hoc* and incomplete as we merely relied on trial and error to select thread diameters and liquid flow rates without proper theoretical understanding of fluid mechanics or heat and mass transfer processes involved. Furthermore, although experimental data on the evaporation rates were obtained, they were limited and we could only discuss qualitative trends over narrow ranges of flow parameters. Finally, the improvement in the performance over the existing state of the art humidifier was appreciable but not dramatic.

The present paper significantly builds upon this early work and reports a dehumidifier that offers 200% improvement in the condensation rate per volume than the current states of the art, which are heavy and expensive or involves significant pressure drops. To establish firm scientific foundation, we performed a first-ever combined experimental and theoretical study of the instability in thin film flows of a high-surface-energy low-viscosity liquid. This allows us to develop a theoretical framework to identify threshold flow rates for transition between two different instability regimes. We also report a complementary numerical model that solves the full Navier-Stokes equations to quantitatively capture the details of flow patterns while accounting for the impact of surface roughness inherent in cotton threads. In addition, our systematic experiments

of heat and mass transfer provide data to develop and validate an analytic model for dehumidification and to quantify the impact of transition between the flow instability regimes on heat and mass transfer processes.

4.2 Experimental setup, data acquisition and numerical simulation

4.2.1 Experimental setup

Figure 4. 1 shows the schematic of the experimental setup used in our study. The setup includes three flow loops: (I) the fresh water loop in the dehumidifier (dashed line); (II) the air loop through the heater and the bubble column to achieve a specific humidity and temperature and finally along the dehumidifier (dotted line); and (III) the closed water loop between the water heater and the bubble column for controlling the water temperature in the bubble column (dash-dotted line).

The dehumidifier (DEH) consists of a 0.6 m-long vertical cylinder of diameter 2.5 inch and includes a square array of 52 (or 96) cotton threads with 7 mm (or 5 mm) pitch. The cotton threads of 0.76 mm diameter are fixed to the bottom acrylic sheet to ensure their verticality. The liquid reservoir is located at the top. To introduce water onto the cotton threads, stainless steel nozzles with an inner diameter of 1.2 mm are used in our dehumidifier design and throughout this study, except in Figure 4. 3 for which we used a nozzle with inner diameter of 0.8 mm. The inlet plenum at the bottom is designed to create a uniform flow of humidified air stream. Distilled water at 20 $^{\circ}$C (monitored using two thermocouples inside the reservoir) is pumped to the top reservoir from a main reservoir (FWR-1). A pump and a flowmeter are used to control the flow rate. Water flows down the cotton threads after exiting the nozzles and absorbs the water vapor from the countercurrent humidified air stream. It is then collected at the bottom reservoir (FWR-2). A

weight scale placed under the fresh water reservoir (FWR-2) with a resolution of 0.1 g to measure the flow rate of fresh water at the outlet of dehumidifier.

We use a bubble column as a humidifier (HUM) to supply air saturated with water to the dehumidifier. Filtered compressed air at 20 ℃ flows into the bottom chamber of a bubble column, which has the cross section of 150 mm × 150 mm and height of 250 mm. The sieve plate has a square array of 25 × 25 holes of diameter 1 mm. Heated water circulates through the bubble column using a heating/pumping unit to ensure the uniform temperature distribution of water inside the bubble column. By adjusting the height of the heated water in the bubble column, a desired output air condition is obtained. The humidified air flows through two plastic tubes with an inner diameter of 25 mm to reach the air inlet of the dehumidifier.

Four sets of 4 micro-thermocouples with a tip diameter of 250 μm are mounted at four axial locations (0.0 m, 0.1 m, 0.4 m, and 0.7 m from the liquid nozzle) and four positions in each axial location (two for air temperature and two for water temperature) as shown in Figure 4. 1 (locations 1, 2, 3, and 4). A differential pressure transducer (P) is used to measure air stream pressure drop along the 0.5 m-long mid-section of the dehumidifier. Two humidity sensors are also mounted at the air inlet and outlet of the dehumidifier to measure the relative humidity of air.

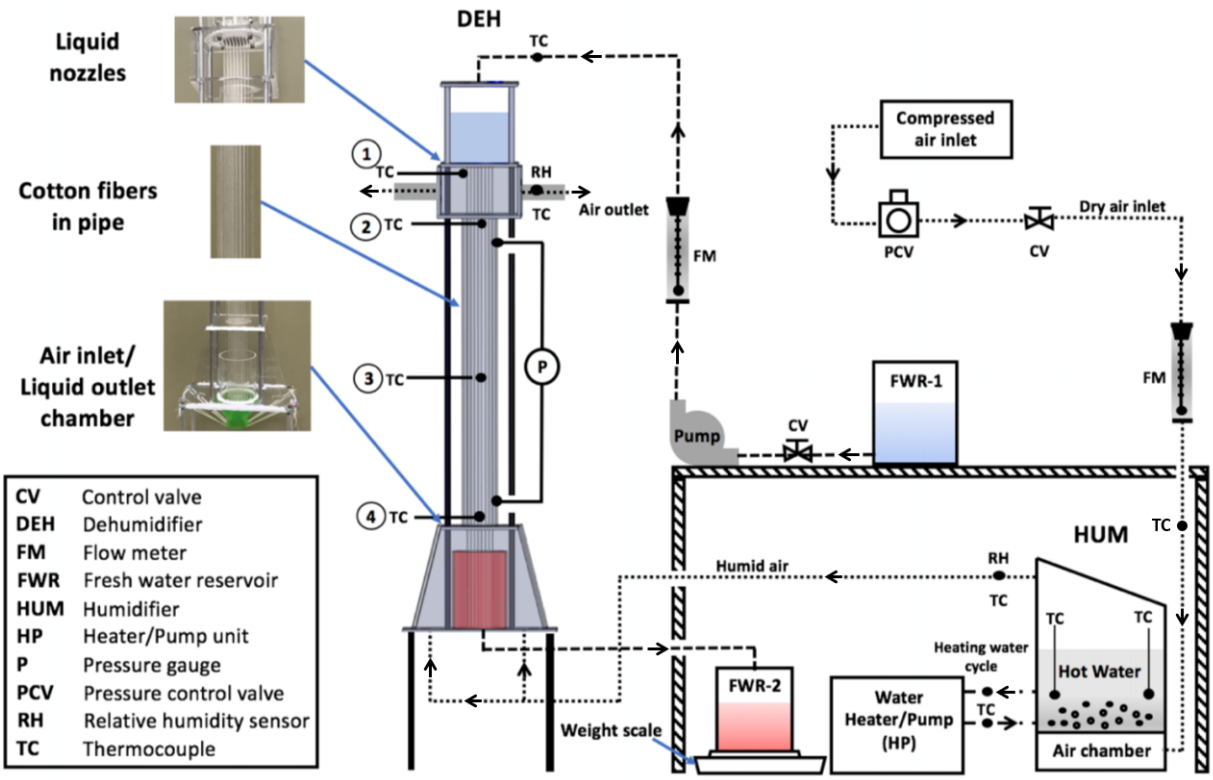

Figure 4. 1: The schematic of the experimental setup used in this study.

4.2.2 Data Acquisition: Temperature, Humidity and Pressure Measurements

For each run, we first adjust the water ($\dot{m}_{Lps}$ = 0.03 g/s -0.14 g/s) and air (V_{air} = 0.2 m/s – 0.75 m/s) flow rates in flow loops (I) and (II). Then, we start flow loop (III) and wait for all the thermocouples, humidity sensors and pressure transducer readings to stabilize to within 1% of their values before taking measurements. Each set of experiments was repeated multiple times to ensure repeatability. The uncertainties of the measured values are estimated as follows: ± 0.1°C for the temperature readings, 0.03 Pa for the pressure readings, 0.1 g/s for the water flow rates at the outlet of DEH, 1% for the relative humidity readings, and 0.05 m/s for the air velocities in the DEH.

4.2.3 Numerical simulation

We perform numerical simulation by solving the 2D axi-symmetric full Navier-Stokes equations for a flow of water along a string with average roughness of λ = 0.04 mm. Figure 4. 2 shows the simulation domain and boundary conditions used. We implement the volume of fluid (VOF) method to track the water-air interface. We employ an unsteady 2D solver with the pressure staggering option (PRESTO) to handle the pressure-velocity coupling. A second-order upwind scheme is used to discretize the momentum equation. A quadratic mesh with the average element size of 0.015 mm and the number of mesh elements of approximately 400,000 is used in typical simulation runs.

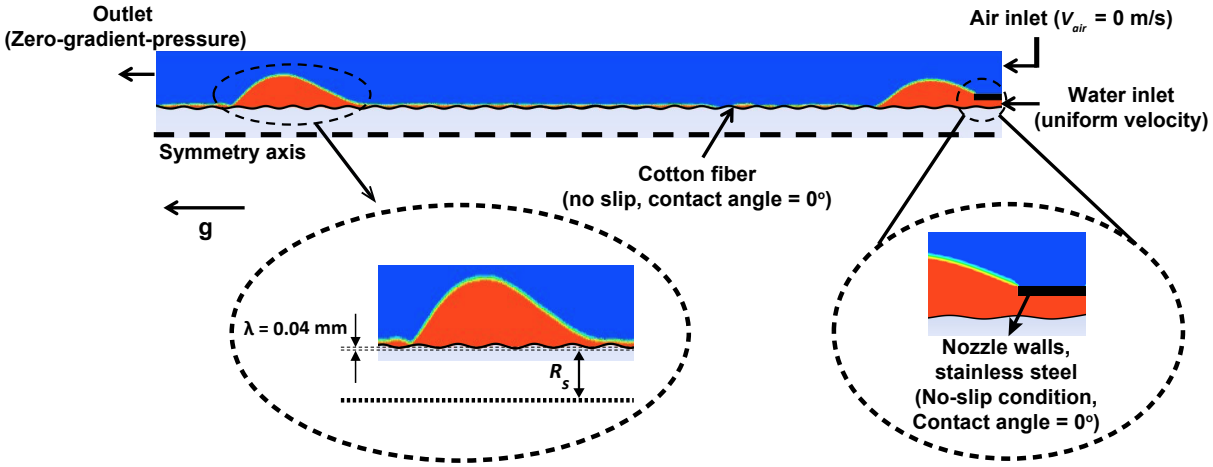

Figure 4. 2: Schematic of the simulation domain and the boundary conditions for the full 2D axi-symmetric Navier-Stokes simulations.

4.3 Instability in thin water films flowing down vertical strings

Due to interplay among surface tension, viscous, inertial, and gravitational forces, liquid films flowing down vertical strings develop complex flow patterns [56], [19], [55], [18], [86]. The insets in Figure 4. 3 show still images of wavy liquid films, representing discrete traveling liquid beads

formed by intrinsic flow instability. We shall show that such wavy patterns help significantly enhance mass transfer and thereby condensation of water vapor.

As shown in Figure 4. 3A, thin liquid films flowing down a string may exhibit absolute instability where the surface tension and viscous forces primarily govern flow dynamics, with liquid beads of a fixed size traveling at a constant speed and interval (i.e., a fixed wavelength of wavy patterns). This is often referred to as the Rayleigh-Plateau regime. When inertia becomes important, thin-film flows may exhibit convective instability where liquid beads travel at different speeds, merging and subsequently forming new beads. Figure 4. 3B illustrates coalescence of water beads in the convective instability regime. These different instability modes can be captured in spatiotemporal diagrams, which schematically represent the temporally evolving positions of liquid beads along the string (Figure 4. 4).

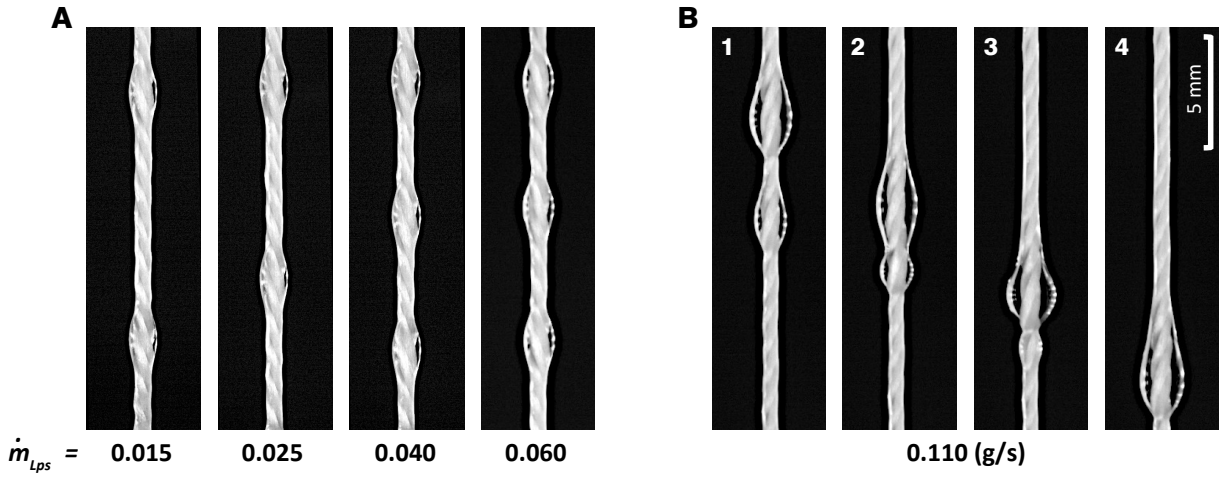

Figure 4. 3: Water flowing down a cotton thread of diameter of 0.76 mm at flow rates of (A) $\dot{m}_{Lps}$ = 0.015 g/s to 0.06 g/s, resulting in the RP instability regime, where beads have constant velocities and spacings, and (B) $\dot{m}_{Lps}$ = 0.11 g/s, generating a flow in the convective instability regime that feature bead coalescence (Nozzle inner diameter = 0.8 mm).

Previous experimental studies of the flow instability in question almost exclusively used well-wetting low-surface energy liquids of high viscosities, such as silicone oil. Water is a high-surface-energy low-viscosity liquid where the influence of surface tension is much more pronounced. As water does not wet common polymeric strings, past studies used a carefully cleaned glass wire to achieve a thin film flow in the absolute instability regime [3]; however, such a fragile material is not practical for engineering applications. Here, we use cotton threads that absorb water into their porous structures and essentially function as super-hydrophilic strings.

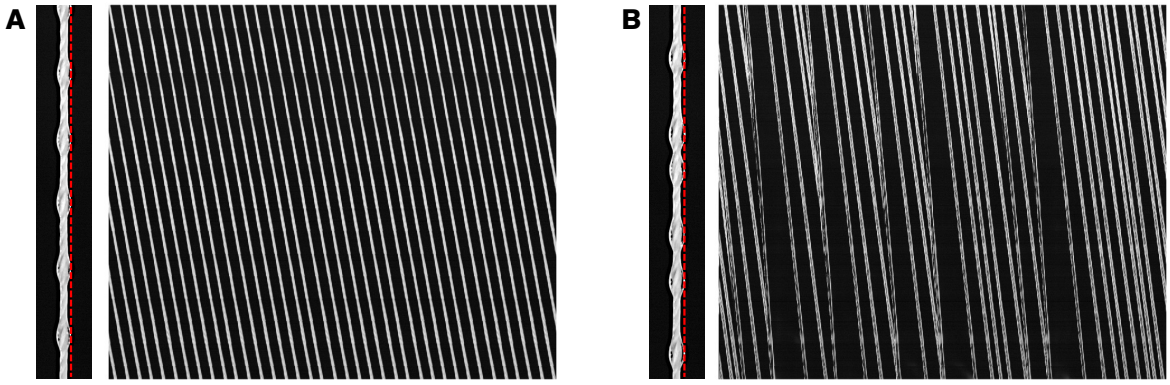

Figure 4. 4: The spatiotemporal diagram of a water film flowing down a cotton thread of diameter 0.76 mm and nozzle inner diameter of 1.2 mm. (A) The Rayleigh-Plateau regime where the trajectory lines are parallel, representing uniform bead spacing ($\dot{m}_{Lps}$ = 0.06 g/s) and (B) The convective instability regime where merging trajectory lines indicate coalescence ($\dot{m}_{Lps}$ = 0.14 g/s).

4.4 Mathematical modeling of water film flows on cotton thread

Earlier studies of thin liquid films flow along strings used low surface tension fluids of relatively high viscosities, whose main flow characteristics can be captured using one dimensional lubrication and related models. Our thin water film flows have much higher characteristic Reynolds numbers and the effects of inertia and nozzles cannot be ignored. We numerically solve

the Naiver-Stoke equations to predict the characteristics of water flowing down a vertical cotton thread such as bead size and bead spacing. We observe that incorporating an effective boundary slip induced by the surface roughness on cotton threads is essential in correctly capturing the flow pattern due to the fact that the smooth surface assumption leads to an underestimation of the bead frequency by more than 30%. As shown in Figure 4. 5A, we define the slip coefficient, λ, as the average amplitude of the surface roughness of cotton thread [87], which was found to be ~0.04 mm for our cotton threads based on the image analysis study. Figure 4. 5B shows that a flow pattern predicted in our numerical stimulation is consistent with the experimental result for a string diameter, D_s, of 0.76 mm, a nozzle inner diameter of 1.2 mm, an average surface roughness, λ, of 0.04 mm at the string surface, and a water flow rate, $\dot{m}_{Lps}$, of 0.12 g/s. Figure 4. 5C shows that the experimental results, which are measured by image analysis, and numerical simulation results for bead spacing, S_{bead}, and bead velocity, V_{bead} agree to within 10%.

As we shall discuss further in the subsequent section, with increasing liquid flow rates, the mass transfer rate of water vapor is generally enhanced. When the film flow transitions from the absolute to the convective instability regime, however, the emergence of irregular bead patterns in the convective regime suppresses further growth in the mass transfer rate with continued increase in the liquid mass flow rate. Identifying the critical flow rate for the instability regime transition is therefore important.

We apply the Orr-Sommerfeld (OS) analysis to investigate the transition. The OS equation derived from linearization of the Navier-Stokes equation is a fourth-order differential equation for the complex perturbation stream function amplitude $\Psi(r)$. The form of the perturbation is given by $\psi(r,t) = \Psi(r)\exp(i(kx - \omega t))$, where $k = k_r + ik_i$ and $\omega = \omega_r + i\omega_i$. In the complex ($k_r$, k_i) plane, two disconnected spatial branches merge together at a point that corresponds to the zero

group velocity, $v_g = d\omega/dk = 0$. This defines the absolute wavenumber k_0 and the absolute frequency ω_0. A zero group velocity with $\omega_{0i} > 0$ identifies the onset of the absolute instability, and the instability regime transition occurs when the two branches merge at a point that corresponds to a real absolute frequency. Figure 4. 5D shows an example of the merging of branches of the OS solutions at a critical flow rate.

Previous OS studies [19], [88] for cylindrical falling films assumed smooth surfaces and applied the no-slip boundary condition at the liquid-solid interface. However, we find that this assumption leads to an overestimation of the critical flow rate by nearly 20% (Figure 4. 5E). As mentioned before, we approximately account for the finite roughness of cotton thread surfaces by introducing the Navier slip condition at the string surface ($r = R_s$)

$$\frac{d\psi}{dr} + \lambda \frac{d^2\psi}{dr^2} = 0 \tag{4.1}$$

where R_s is the average string radius. This approximation represents homogenization of the no-slip condition on rough surfaces and is sometimes referred to as the Navier friction condition. To account for uncertainty in measured values of the string radius, we perform the OS analysis for a range of string radius values, 0.35 mm $\leq R_s \leq$ 0.4 mm and compare the predicted critical flow rates for $\lambda = 0$ (no-slip) and $\lambda = 0.04$ mm in Figure 4. 5E. Our results show that the surface roughness, λ, of 0.04 mm produces decreased unperturbed flow velocities and yields a smaller critical flow rate, which is consistent with our experimental observations.

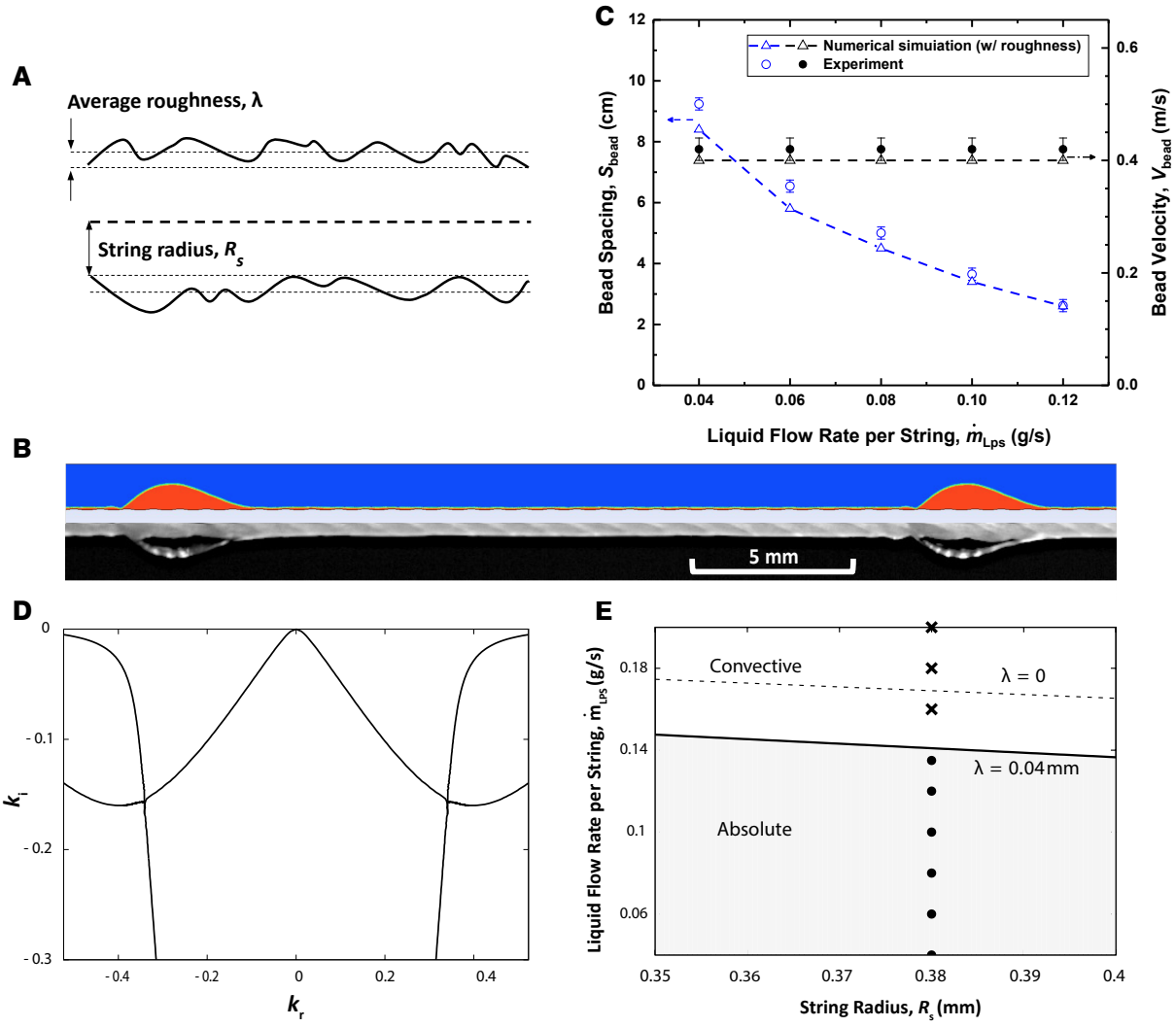

Figure 4. 5: (A) Schematic of a cotton thread with radius of R_s and average roughness of λ. (B) Comparison of the experimentally obtained liquid profile and the results obtained from the full Navier-Stokes numerical simulation (string diameter D_s = 0.76 mm, the nozzle inner diameter = 1.2 mm, liquid mass flow rate $\dot{m}_{Lps}$ = 0.12 g/s, and average roughness of λ = 0.04 mm). (C) The bead spacing and velocity predicted from full Navier-Stokes numerical simulation compared with experimental results (D_s = 0.76 mm, nozzle inner diameter = 1.2 mm, $\dot{m}_{Lps}$ = 0.04 - 0.12 g/s, and λ = 0.04 mm). (D) Spatial branches in the complex k-plane from the OS analysis for a liquid flow rate of 0.141 g/s, string diameter of 0.76 mm, effective slip length of 0.04 mm and $\omega_i = 0$. (E) The absolute and convective instability regimes in the parameter plane of the flow rate versus the string radius. The solid line corresponds to the OS solutions with roughness induced boundary slip, and

the dashed line corresponds to the no-slip case. The circle and cross symbols represent the regularly or irregularly spaced liquid beads observed in the experiments.

4.5 Results and discussion

4.5.1 Condensation Rates: Mass transfer Conductance

Direct determination of the condensation rate from the difference between the inlet and outlet liquid flow rates is challenging due to fluctuations in the inlet and outlet flow rate and uncontrolled evaporation in and around the inlet and outlet reservoirs. We instead analyze axial temperature profiles (Figure 4. 6) using the energy and mass balance equations to indirectly calculate the rate of mass transfer of water vapor from the humidified air stream to the liquid films flowing down the threads. The mass transfer conductance, g_m, which has the unit of mass flux [kg/(m^{2}s)], is a proportionality factor for mass transfer rates. It is defined as $\rho_m D_{12}/\delta$, where ρ_m is the density of the air/water mixture, D_{12} is the binary diffusion coefficient of water vapor in air and δ is the thickness of mass transfer boundary layer.

The balance equations are derived by applying the mass and energy conservation principle to a differential control volume shown in Figure 4. 7A. The mass balance equations for the water and air streams are:

$$\dot{m}_{w,2} - \dot{m}_{w,1} = g_m \left[m_1\left(T_{a,1}\right) - m_1\left(T_{w,1}\right) \right] dA \tag{4.2}$$

$$\dot{m}_{a,2} - \dot{m}_{a,1} = \dot{m}_{w,2} - \dot{m}_{w,1} \tag{4.3}$$

Here, $\dot{m}$ is the mass flow rate and the subscripts a and w denote the properties of the saturated air and water, respectively. $m_1(T_{a,1})$ and $m_1(T_{w,1})$ are the mass fractions of water in the saturated air at temperatures $T_{a,1}$ and $T_{w,1}$, respectively. We define dA as the nominal air-water interfacial area in the control volume. For mathematical convenience, we assume a perfect cylinder of water flowing down the cotton thread. The radius of the water cylinder was obtained from the Nusselt solution based on the experimentally measured water mass flow rates [18]. The energy balance equation for the combined air and water stream in terms of their enthalpy h is

$$\dot{m}_{a,2}h_{a,2} - \dot{m}_{a,1}h_{a,1} = \dot{m}_{w,2}h_{w,2} - \dot{m}_{w,1}h_{w,1} \tag{4.4}$$

The total heat transfer rate between the air and water stream is the sum of the rate of sensible heat transfer by convection, q_{conv}, and the rate of heat transfer associated with condensation:

$$\dot{m}_{w,2}h_{w,2} - \dot{m}_{w,1}h_{w,1} = q_{conv}dA + g_m\left[m_1\left(T_{a,1}\right) - m_1\left(T_{w,1}\right)\right]\left(h_{w,1} + h_{fg}\left(T_{w,1}\right)\right)dA \tag{4.5}$$

where q_{conv} is expressed in terms of the temperature difference and the convective heat transfer conductance g_h:

$$q_{conv} = g_h C_{p,a}\left(T_{a,1} - T_{w,1}\right) \tag{4.6}$$

The heat transfer conductance, g_h, which as the unit of [kg/(m^{2}s)], is defined as $h/C_{p,a}$ where h is the conventional heat transfer coefficient and $C_{p,a}$ is the specific heat of the saturated air. Since the range of temperature changes is relatively small, we assume that $C_{p,a}$ is constant. The Lewis number, *Le,* for water vapor and air is near unity. Based on the analogy between heat and mass

transfer, we estimate the ratio of mass and heat transfer conductances to be $g_m / g_h \sim Le^{2/3} = 1.08$ [89].

For each experimental case, we solve Eqs. (4.2)-(4.6) using the measured water inlet temperature, $T_{w,in}$, and air outlet temperature, $T_{a,out}$ as inputs. We adjust the value of g_m iteratively until we match the measured temperature profiles for both the air and water streams. Figure 4. 6 shows representative experimental temperature profiles and the corresponding best fits from Eqs. (4.2)-(4.6).

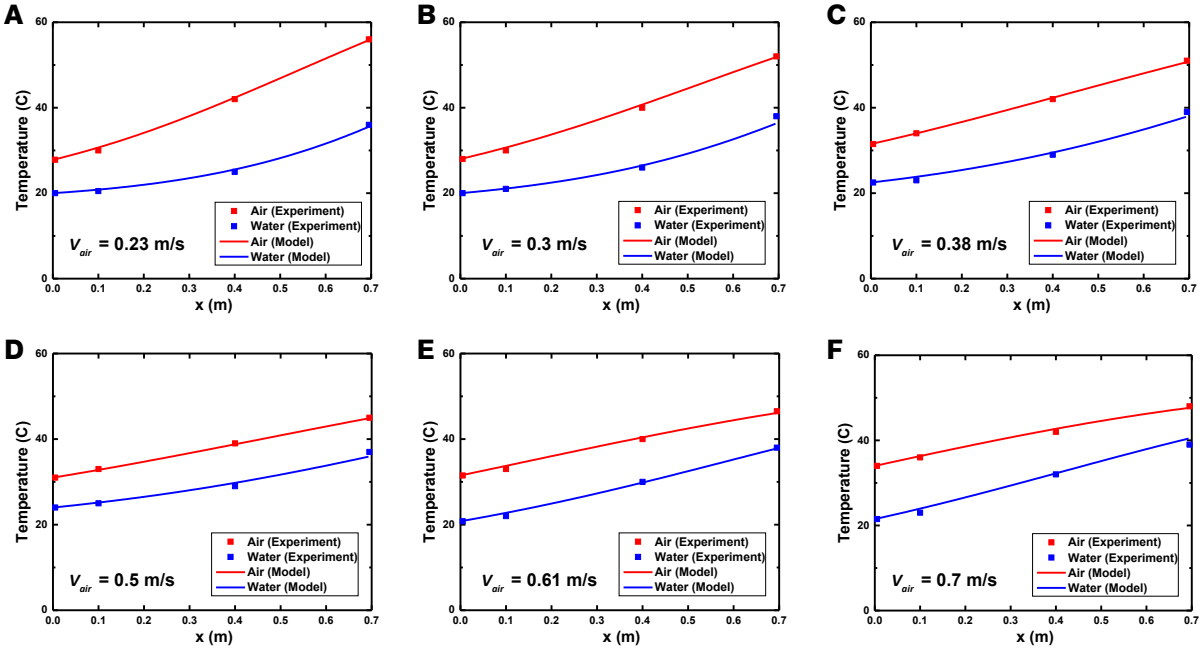

Figure 4. 6: The experimental and model prediction results for the temperature profiles of the water and air streams along the dehumidifier (52 strings and $\dot{m}_{Lps}$ = 0.065 g/s) with the superficial air speed V_{air} of (A) 0.23 m/s, (B) 0.3 m/s, (C) 0.38 m/s, (D) 0.5 m/s, (E) 0.61 m/s, and (F) 0.7 m/s. The symbols represent the experimental results and the lines represent the model predictions.

Figure 4. 7B shows the experimentally determined mass transfer conductance and water bead spacing as a function of the water flow rate under two different velocities of the counterflowing

air. As the water mass flow rate increases, the bead spacing decreases and the total mass transfer conductance increases. To further analyze the effect of water beads on condensation rates in our experiments, we develop a simplified model. We decompose our liquid film conceptually into two components in a uniform air flow condition: 1) a thin continuous liquid substrate coating the thread and 2) liquid beads of diameter D_{bead} sliding on the liquid substrate at speed V_{bead} in the range of 0.3-0.42 m/s. We model the liquid substrate as a stationary cylinder and each liquid bead as a sphere of the equivalent diameter (see Figure 4. 8A).

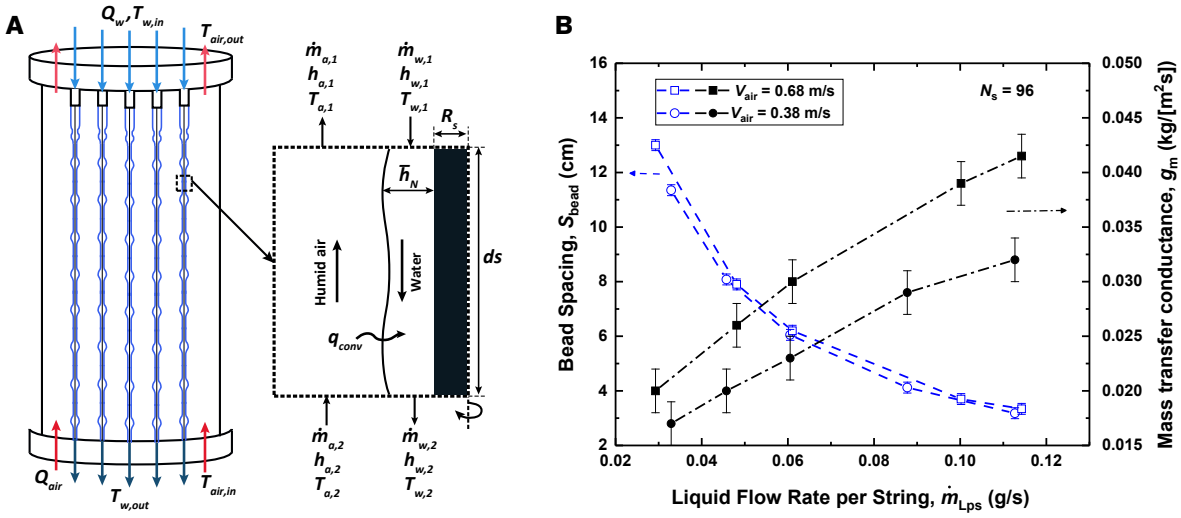

Figure 4. 7: (A) Schematic of the control volume used to develop the governing mass and energy balance equations for the dehumidifier. (B) Mass transfer conductance and bead spacing as a function of the liquid flow rate per string under two different air stream velocities (V_{air} = 0.38 m/s and 0.68 m/s).

For mass transfer of water vapor from the humidified air stream to the sphere, we use the heat and mass transfer analogy to obtain the Sherwood number *Sh* [89], [90]

$$\overline{Sh}_{bead} = 2 + \left(0.4\,\mathrm{Re}_{bead}^{1/2} + 0.06\,\mathrm{Re}_{bead}^{2/3}\right) Sc^{0.4} \tag{4.7}$$

Here, the Reynolds number is $Re_{bead} = \rho_m \left(V_{bead} + V_{air}\right) D_{bead} / \mu$, where the superficial air velocity, V_{air}, is calculated through dividing the volumetric flow rate of air by the cross section area provided by the acrylic cylinder with the diameter of 6.5 cm for the air stream. The dynamic viscosity of air is denoted by μ and the Schmidt number *Sc*. The mass transfer conductance for the bead, $\overline{g}_{m,bead}$, is next obtained from *Sh*:

$$\overline{g}_{m,bead} = \rho_m \mathcal{D}_{12} \overline{Sh}_{bead} \Big/ D_{bead} \tag{4.8}$$

Rigorously speaking, our liquid beads may not be represented as isolated spheres in a uniform gas flow. We use the existing correlation for $\overline{g}_{m,bead}$ only as a convenient and yet approximate expression to quantitatively interpret our experimental data. In order to assess the accuracy of the correlation for $\overline{g}_{m,bead}$, we numerically simulated air flows over an array of water beads flowing down a cotton thread. We find that, for relatively large inter-bead spacings (> 6 times of the bead diameter), which is satisfied for all experimental conditions we used, the impact of preceding liquid beads is relatively small. We estimate the error in $\overline{g}_{m,bead}$ calculated using the existing correlation for an isolated sphere in a uniform gas flow to be less than 10%.

For the liquid substrate, we determine the mass transfer conductance $\overline{g}_{m,sub}$ by spatially averaging the local value from the boundary layer theory. We use the boundary layer theory for a flat surface to estimate the average mass transfer conductance over a liquid substrate, which is modeled as a cylinder.

Under our experimental conditions, the blowing factor, $\mathcal{B}_m$ [90],

$$\mathcal{B}_m = \frac{m_{1,e} - m_{1,s}}{m_{1,s} - 1} \tag{4.9}$$

is estimated to be small, -0.07 < $\mathcal{B}_m$ < 0 and the zero normal velocity condition may be assumed to hold at the water-air surface. Using the established boundary layer theory for a flat surface, we obtain

$$\bar{g}_{m,sub} = \int_{0^+}^{L_{sub}} 0.332 \rho_m V_{air} \, \mathrm{Re}_x^{-1/2} \, Sc^{-2/3} dx \Big/ L_{sub} \tag{4.10}$$

The local Reynolds number is defined as $Re_x = \rho_m V_{air} \, x / \mu$, where the local coordinate x is shown in Figure 4. 8A. We use the analytic correlation for the boundary layer over a flat plate as a convenient and yet approximate expression for $\bar{g}_{m,sub}$ to quantitatively interpret our experimental data. To assess the accuracy of this approximation, we compare the average shear stress over the liquid substrate obtained using numerical simulation with that obtained using the analytic correlation. The estimated errors are approximately 4% for $\dot{m}_{Lps}$=0.115 g/s and approximately 15% for $\dot{m}_{Lps}$ =0.035 g/s.

The water-air interfacial area of the beads, A_{bead}, and that of the substrate, A_{sub}, are used as the weighting factors to calculate the overall g_m as follows:

$$g_m = \frac{\bar{g}_{m,bead} . A_{bead} + \bar{g}_{m,sub} . A_{sub}}{A_{bead} + A_{sub}} \tag{4.11}$$

Figure 4. 8B shows the experimentally determined and predicted mass transfer conductances of the design with 96 strings as a function of the superficial air velocity for various values of the

water flow rates. We can observe that the predicted and measured mass transfer conductances agree to within 7%. The reasonably good agreement between the predicted and experimentally obtained g_m values indirectly supports the overall validity of our physical model for the heat and mass transfer processes involved. But we do note that the water-air interfacial areas are needed as input parameters, which are obtained either from experiments or from a separate fluid mechanics model. Our results suggest that the mass transfer conductance for the beads are up to 5 times of that of the substrate (see Figure 4. 8C). This finding is in accord with the past studies of condensation on localized surface bumps, which were inspired by desert beetles, where the importance of surface features on condensation rates was suggested[91]. This enhanced mass transfer around water beads explains high mass transfer rates and hence correspondingly high condensation rates obtained in our experiments.

From Figure 4. 8B, one might expect that one could continue to increase the mass transfer and hence condensation rate by further increasing $\dot{m}_{Lps}$. When the water flow rate is increased above 0.135 g/s, however, the flow transitions into the convective instability regime and we observe a different trend (Figure 4. 9). As mentioned before, the transition to the convective instability regime results in bigger and faster moving beads. The increased bead diameter leads to reduction in the mass transfer conductance around each bead while the increased bead spacing leads to reduction in the spatial density of liquid beads. These effects counteract enhancement resulting from the increased bead traveling speed (Eqs. (4.7) and (4.8)). As a result, the overall mass transfer conductance remains nearly unchanged after the further increase in the liquid flow rates.

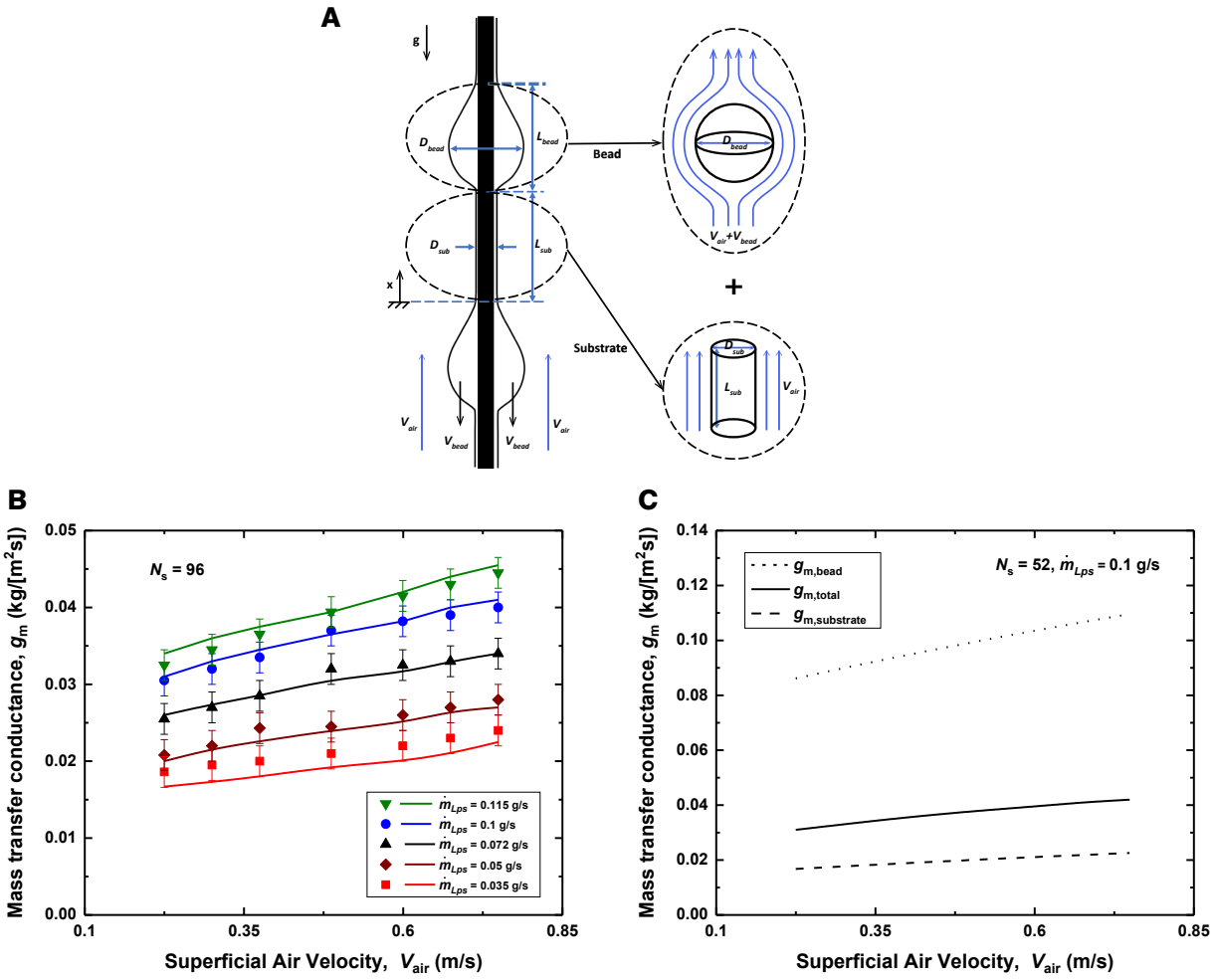

Figure 4. 8: (A) Schematic illustrating the decomposition of the water film into two components: 1) each water bead as a sphere in a uniform air stream of velocity $V_{air} + V_{bead}$ (to account for the bead velocity), and 2) a stationary water cylinder with the same diameter as the liquid substrate coating the string in a uniform air stream of velocity V_{air}. (B) The experimental and predicted mass transfer conductances as a function of the superficial air velocity for the dehumidifier with 96 strings. Various sets of data are presented for different water flow rates per string, $\dot{m}_{Lps}$. The liquid flows are all in the RP regime. The symbols represent the experimental results and the lines the model predictions. (C) The estimated mass transfer rate [kg-water/s] to the total interfacial area of: 1) liquid beads or 2) the liquid substrate.

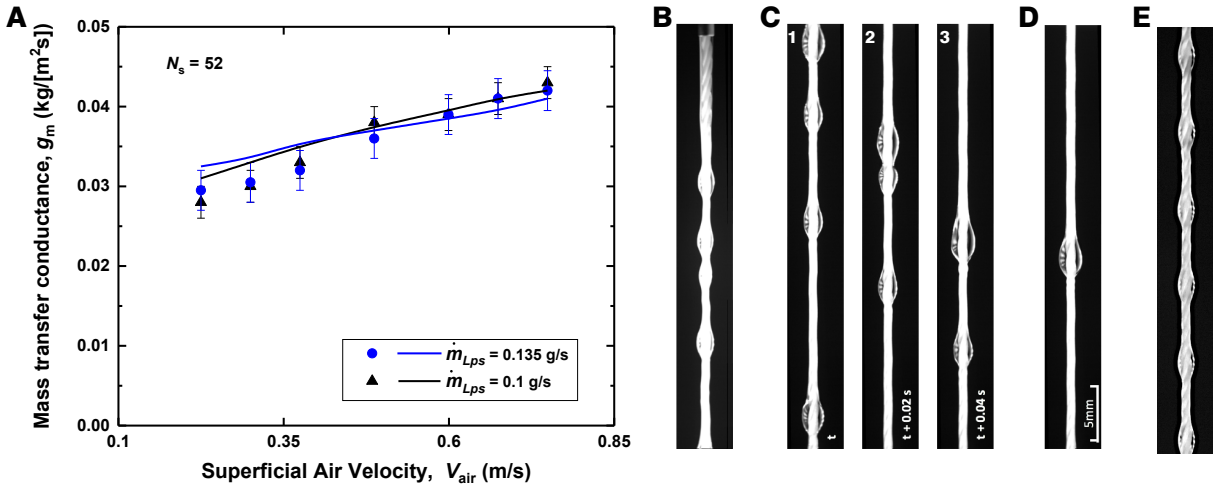

Figure 4. 9: (A) The experimental and predicted mass transfer conductances as a function of the superficial air velocity. Two sets of data are shown, representing $\dot{m}_{Lps}$ = 0.1 g/s (RP regime) and $\dot{m}_{Lps}$ = 0.135 g/s (convective instability regime). The symbols represent the experimental results and the lines represent the model predictions. The error bars for the data for $\dot{m}_{Lps}$ = 0.135 g/s are bigger than those for the smaller water flow rate due to large variations in the geometric parameters of the beads in the convective instability regime. (B-D) The liquid film pattern at $\dot{m}_{Lps}$ = 0.135 g/s within 5 cm from the nozzle where the instability starts to disrupt the flat film region (B), within the next 5 cm region where beads coalesce and form bigger beads (C), and in the semi-steady region where these bigger beads move at higher speeds (D). (E) The liquid film pattern with $\dot{m}_{Lps}$ = 0.1 g/s corresponds to the RP instability regime.

4.5.2 Gas stream pressure drop

A key consideration in a dehumidification process, aside from the overall mass transfer and hence condensation rate, is axial pressure drop in the gas stream. In Figure 4. 11A, we compare the experimentally measured pressure drop in the air stream per unit length and the corresponding model prediction as a function of the superficial air velocity. The two results agree to within 6%.

The prediction is based in part on an established empirical correlation for longitudinal flows over an array of parallel solid cylinders [92]–[94]. The pressure drop consists of three major components: the frictional pressure drop dP_f, the pressure drop due to gravity dP_g and the pressure drop due to the momentum change dP_m:

$$\frac{dP}{dz} = \left(\frac{dP}{dz}\right)_f + \left(\frac{dP}{dz}\right)_g + \left(\frac{dP}{dz}\right)_m \tag{4.12}$$

The pressure drop due to gravity $dP_g = \rho_m g dz$ in our setup is less than 7 Pa. The term dP_m results from vapor condensation and deceleration in the air stream [95]:

$$\left(\frac{dP}{dz}\right)_m = \left(\frac{\dot{m}}{A_c}\right)^2 \left(\frac{1}{\rho_m} + \frac{1}{\rho_w}\right) \frac{d\omega}{dz} \tag{4.13}$$

A_c represents the cross-section area for the air stream, ρ_w is the density of water, and ω is the humidity ratio.

The frictional pressure drop is the sum of the frictional pressure drops caused by liquid beads (sphere of diameter D_{bead} and the relative velocity of $V_{bead} + V_{air}$) and that by the liquid substrate (cylinder of diameter, D_{sub} and and the air stream velocity of V_{air}). The friction on the tube wall is estimated to be below 0.2 Pa, with the maximum corresponding to the air velocity of 0.75 m/s.

The frictional pressure drop for laminar flows along an array rod bundles [92] was given in terms of the friction factor f_L:

$$f_L \,\mathrm{Re}\left(\frac{D_f}{D_h}\right) = \frac{8\sigma^2}{2(1-\sigma) - \ln(1-\sigma) - 0.5(1-\sigma)^2 - 1.5} \tag{4.14}$$

$$\left(\frac{dP}{dz}\right)_f = \frac{2 f_L \rho_m V_{air}}{D_h} \tag{4.15}$$

Here, $Re = \rho_m V D_h / \mu$ and V and μ are the relative air stream velocity and viscosity, respectively. D_h and D_f are the hydraulic diameter and the average liquid film diameter calculated from Nusselt solution, respectively [18]. The parameter σ represents the fraction of the total cross section available to the air flow.

The maximum Reynolds number for air flows in our experiments is approximately 2400, comparable to the critical Reynolds number for transition to turbulence (2300). Reynolds number can be calculated from $Re = \rho_m (V_{air} + V_{bead}) D_h / \mu$ where D_h is the hydraulic diameter of the air duct. In the laminar flow regime, the pressure drop exhibit an approximately linear dependence on the superficial air velocity.

Liquid beads in the present work have relatively low geometric profiles, resulting in smaller form drag than spherical droplets in the presence of a counterflowing gas flow. This was confirmed in an independent experimental study of heat transfer in a multi-string heat exchanger using non-evaporating liquids. In that study, the Reynolds analogy was shown to hold reasonably well, indicating that the frictional component to the pressure drop dominates over the component associated with form drag[25].

As the counterflowing air stream velocity, aerodynamic drag does deform liquid beads and change bead spacing (Figure 4. 10). However, significant deformation does not occur until the air velocity is increased well beyond the range expected of typical dehumidification processes.

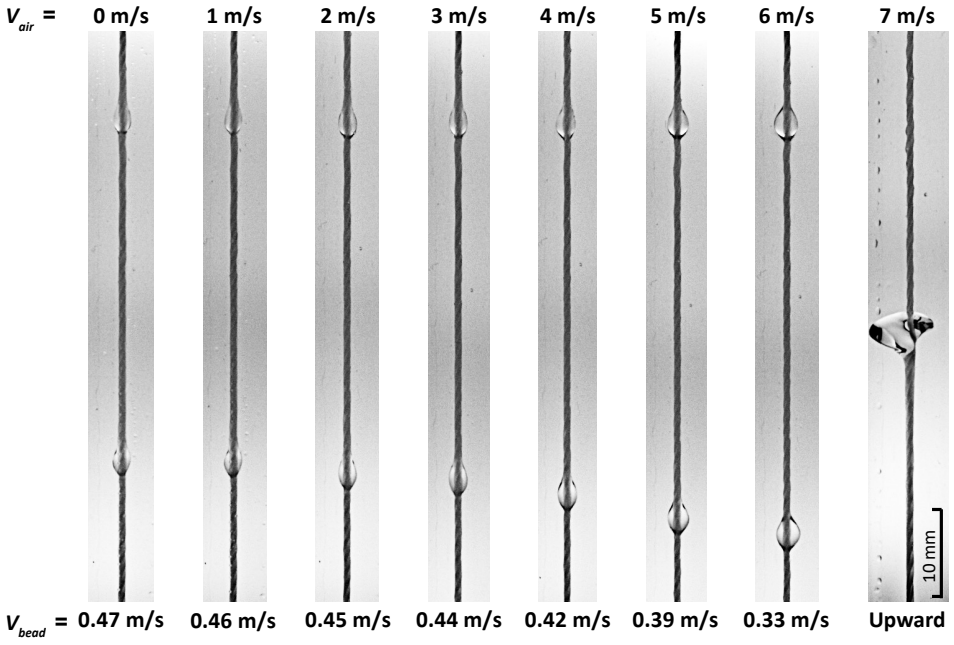

Figure 4. 10: The effect of counterflowing air streams on the dynamics of water film flows. Increasing air superficial velocities lead to increasing bead sizes and bead spacing. Only at very high air velocities (V_{air} > 7 m/s), well beyond the expected range used in dehumidifiers, water beads experience significant deformation and may reverse their directions.

4.5.3 Effectiveness, heat flux and overall performance

To quantify the overall performance of our device, we define the overall capacity coefficient, $g_m A_{int}/V_{deh}$, as our device performance parameter [7]. Here, A_{int} and V_{deh} are the total liquid-gas interfacial area and the total volume of the device, respectively. This parameter essentially conveys the total mass transfer rate per unit volume of a dehumidifier. Figure 4. 11B shows the overall capacity coefficient of our design compared with that of other dehumidifiers as a function of the total gas-stream pressure drop. We note that our unique geometric configuration offers at least 3 times higher overall capacity coefficients compared with existing designs at smaller air-stream pressure drops. One might argue that the air and water mass flow rates can affect the overall capacity performance. However, this significant improvement in the overall capacity coefficient is due to the ability of our compact design to provide intrinsic surface bumps, high interface-to-

volume ratios for mass transfer, and the long resistance time for water vapor capturing due to the shear stress at the string surface. To ensure the fairness of our comparison in Figure 4. 11B, the results representing the other existing designs are obtained from comparable conditions with our experimental condition (see

).

Although previous studies did not report the weight of their humidifiers, we expect that the present humidifier, constructed of a plastic housing and cotton threads, also provides significant weight reduction from established metal-based dehumidifiers.

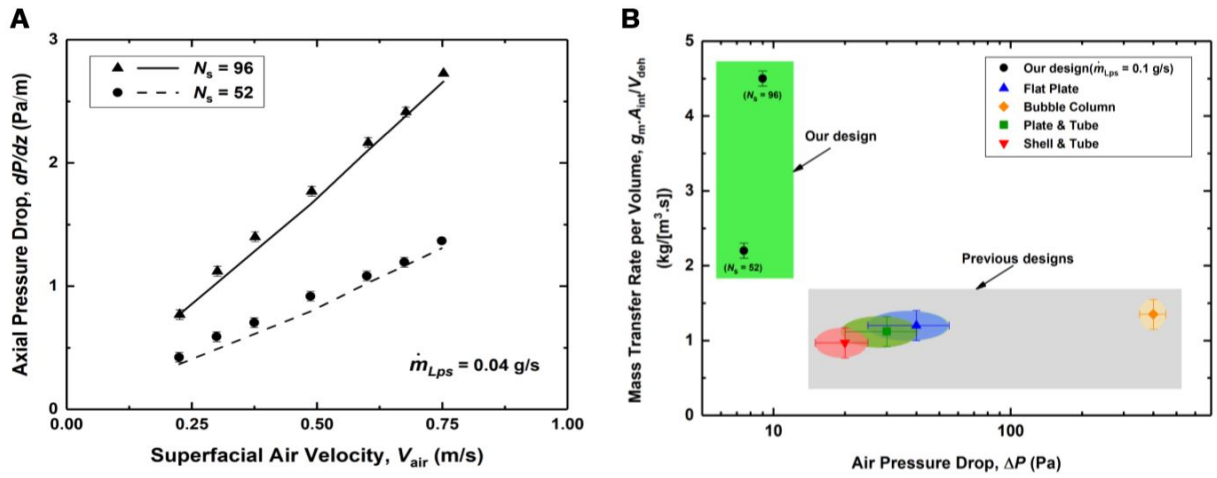

Figure 4. 11: (A) Pressure drop as a function of the superficial air velocity for the dehumidifiers with 52 and 96 strings. Symbols represent the experimental data and the lines represent the model results. (B) Comparison of the mass transfer rate per volume as a function of the air pressure drop per length of dehumidifier. We compare our geometric configuration with previously reported dehumidifier designs, such as flat-plate[95], bubble column[96], plate-tube[97], and shell-and-tube[98].

In a heat and mass exchanger, the modified heat capacity ratio, HCR, is defined as [77], [99]

$$HCR = \frac{\Delta \dot{H}_{\max,c}}{\Delta \dot{H}_{\max,h}} \tag{4.16}$$

HCR is the comparison between the maximum rate of change in the total enthalpy of the cold stream and that of the hot stream. The maximum rates of change can be obtained by assuming respective ideal conditions. In other words, $\Delta \dot{H}_{\max,h}$ is obtained from a condition where the outlet temperature of the air reaches the inlet temperature of the water. Likewise, $\Delta \dot{H}_{\max,c}$ can be obtained from a condition where the outlet temperature of the water reaches the inlet temperature of the air.

An energy-based effectiveness, ε, can then be defined for the dehumidifier in the following form:

$$\varepsilon = \frac{\Delta \dot{H}}{\Delta \dot{H}_{\max}} \tag{4.17}$$

Here, $\Delta \dot{H}_{\max}$ is the maximum possible rate of change of enthalpy, $\min(\Delta \dot{H}_{\max,h}, \Delta \dot{H}_{\max,c})$, and the $\Delta \dot{H}$ is the actual rate change for one of the streams [100].

Another performance parameter of dehumidifiers is the total heat exchanged between the coolant and the air-vapor mixture as discussed in Nayaran et al. [84]. Figure 4. 12A and B show the effect of HCR on the energy-based effectiveness and the heat flux (kW/m^2), respectively. We can see that the effectiveness reaches the minimum when HCR is 1 (i.e. thermally balanced state). The same trend was reported by Nayaran et al. [100]. In contrast, the heat flux, $\dot{q}$, increases with

increasing mass flow rates of either of the streams until it reaches a limit due to the limit on the rate of change in the total enthalpy of the other stream.

shows the calculated values of ε and $\dot{q}$ for the present device and the existing technologies reported in the literature. All the dehumidifiers offer comparable effectiveness. We note that ε is a function of HCR (Figure 4. 12A) and that a complete comparison is not feasible when ε was not reported over a wide range of HCR.

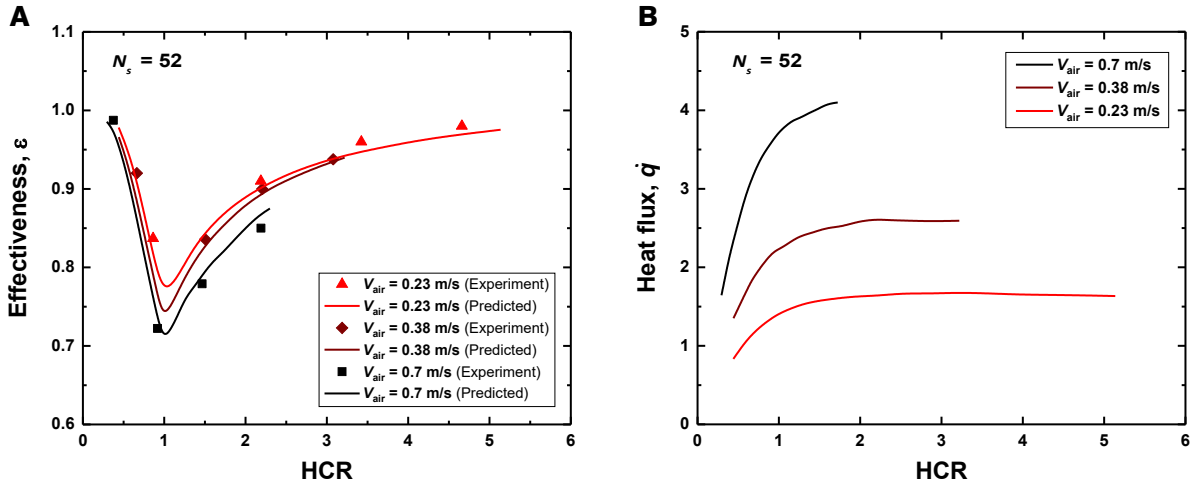

Figure 4. 12: (A) Experimental results and model predictions of the energy-based effectiveness of dehumidifiers as a function of HCR for different superficial air velocities. (B) The effect of HCR on the heat flux for different superficial air velocities (model prediction results).

The heat flux, $\dot{q}$ [kW/m^2], is also provided for the different dehumidifiers in

. One goal in designing a dehumidifier is to achieve the highest condensation rate in a unit volume, which is directly proportional to $\Delta \dot{H}$. The heat flux is related to the total enthalpy change through the following relation:

$$\dot{q} = \frac{\Delta \dot{H}}{A_f} \tag{4.18}$$

where, A_f is the area for heat transfer from the hot air stream to the cold water stream in a given dehumidifier. Some dehumidifiers offer very high heat flux and yet poor overall performance due to their small heat transfer area. This deficiency can be captured by $\Delta \dot{H}$ or the overall capacity coefficient $g_m A_{int}/V_{deh}$.

The number of transfer units, N_{tu}, is defined as follows:

$$N_{tu} = \frac{g_m A_{int}}{\dot{m}_w} \tag{4.19}$$

Here, $\dot{m}_w$ is the inlet mass flow rate of water. N_{tu} can be numerically calculated using [90]:

$$N_{tu} = \int_{h_{w,in}}^{h_{w,out}} \frac{dh_w}{h_a - h_s} \tag{4.20}$$

where, h_a and h_w are the enthalpy of the saturated air (at T_{air}) and water (at T_{water}), respectively. h_s is defined as the enthalpy of saturated air at T_{water}. The values of h_w and h_s were obtained from existing literatures [101]. The enthalpy of the saturated air, h_a, is calculated using $h_a = h_{a,out} + \dot{m}_w / \dot{m}_a (h_w - h_{w,in})$. The overall capacity coefficient $g_m A_{int}/V_{deh}$, then, is calculated from N_{tu} using the following equation:

$$\frac{g_m A_{int}}{V_{deh}} = \frac{N_{tu} \dot{m}_w}{V_{deh}} \tag{4.21}$$

Table 4. 1 shows all the intermediate parameters used to calculate the overall capacity coefficients.

Table 4. 1 lists the pressure drop, ε, $\dot{q}$, and overall capacity coefficient of our dehumidifier for a wide range of water-to-air mass flow rate ratio, $m_r = \dot{m}_{w,in} / \dot{m}_{a,in}$, (1.37 - 4.41), covering the range of m_r reported for the other dehumidifiers [95]–[98].

The relative humidity, *RH*, measured at the air inlet and outlet of our dehumidifier is approximately 100% in all our experimental conditions. The mass of the condensed vapor can be calculated from the difference in water content of the inlet and outlet air streams. For our experimental cases the absolute condensation rate is in the range of 0.15-0.32 kg/h.

The ratio of the condensed water vapor to the total water vapor in the inlet air stream is calculated to be in the range of 0.31 to 0.85 for our dehumidifier. The smallest value, 0.31, corresponds to the 52-string configuration with the lowest water-to-air mass flow rate ratio (air superficial velocity of 0.7 m/s and water flow rate per string of 0.035 g/s). The highest value, 0.85, corresponds to the 96-string configuration with the highest water-to-air mass flow rate ratio (air superficial velocity of 0.23 m/s and water flow rate per string of 0.115 g/s).

Table 4. 1: Dehumidifier Comparison

Dehumidifier	**Our design**				**Plate & Tube**	**Flat Plate**	**Bubble Column**	**Shell& Tube**
	N_s=96	N_s=96	N_s=96	N_s=52				
Air flow rate, $\dot{m}_a$ [g/s]	2.45	2.45	2.45	2.45	8.7	700	2	159
Water flow rate, $\dot{m}_w$ [g/s]	3.4	7	10.8	7	10.2	1300	8.3	227
Water/Air flow rate, m_r	1.37	2.85	4.41	2.85	1.17	1.86	4.17	1.42
Length, L (m)	0.7	0.7	0.7	0.7	1	1.9	0.04	0.6
Volume, V_{deh} (m^3)	0.00222				0.015	0.4844	0.0031	0.1991
Air inlet T [^{o}C]	49	49	48	41	59.5	60	70	58
Air outlet T [^{o}C]	30	24.5	23.8	25	48.5	42	49	48
Water inlet T [^{o}C]	21	21	22	20	25	15	20	30
Water outlet T [^{o}C]	44	33.5	30	27	58	46	43	56
NTU	2.07	1.11	0.76	0.71	1.19	0.60	0.30	1.01
g_m*A [g/s]	6.9	7.8	9.9	4.9	12.0	790	4.0	229.6
g_m*A/V [kg/s.m^3]	3.1	3.5	4.5	2.2	0.8	1.6	1.3	1.2
Pressure drop, ΔP [Pa]	9	9	9	8	25	32	400	18
ΔP/Length [Pa/m]	13	13	13	11	25	16.6	10000	29.6
Effectiveness, ε	0.9	0.91	0.94	0.85	0.94	0.85	0.86	0.9
Heat Flux, $\dot{q}$ [kW/m^2]	1.4	1.9	2.1	1.8	0.2-0.4	3.7	15	-

4.6 Summary

In summary, we have demonstrated the ability of our water vapor capturing design in being able to significantly increase the condensation rate per device volume (200% increase), by taking advantage of high mass transfer rates of surface bumps, while having the capability to remarkably

decrease the air stream pressure drop, through providing straight paths for gas flow, compared with the current dehumidifiers.

In the present work, liquid beads are generated through intrinsic instability of thin liquid films flowing down vertical cotton threads. No high-pressure spray nozzles or electric and other excitations are therefore necessary. Generating droplets of a narrow and controlled size distribution in spray columns is very challenging. Larger droplets are remarkably undesirable because they have higher fall velocities (shorter residence times) and larger internal thermal resistance, negatively impacting overall heat/mass transfer effectiveness. Very small droplets are also undesirable because they may be entrained by gas flows and then mix with condensates in the dehumidifier, which is problematic due to degrading the quality of "clean" water output.

CHAPTER 5

Experimental study of a multi-string counterflow wet electrostatic precipitator for collection of diesel particulate matter (DPM)

Wet electrostatic precipitators (WESP) are appealing devices for collecting ultrafine diesel particulate matter (DPM), substances that could have deleterious effects on human health. Here, we report an experimental, theoretical, and numerical simulation study on a novel string-based two-stage WESP. This new design consists of grounded vertical porous strings, along which water flows down in the presence of a counterflowing gas stream. The water beads, generated through intrinsic flow instability, travel down the strings and collect the charged particles in the counterflowing gas stream. We performed systematic experiments on two 0.6-m-tall designs in a cylindrical and a linear configuration. We examined the effects of the collector bias voltage, air stream velocity, and water flow rate on the number-based fractional collection efficiency for DPM in a diameter range of 10 nm to 2.5 μm. We report that the collection efficiency can be increased with an increase in the collector bias voltage or a decrease in the airflow rate. Also, our results show that water-to-air flow rate ratios as low as ~0.0066 [kg-water/kg-air] can achieve a collection efficiency over 70% even for fine and ultrafine particles. The cylindrical and the linear configuration exhibited similar collection efficiencies under the similar working conditions. We

also compare the water-to-air mass flow rate ratio, air flow rate per unit collector volume, and the collection efficiency between the string-based configuration and previously studied WESPs. The string-based WESP delivers a comparable collection efficiency with at least three times smaller water-to-air mass flow rate ratios. Our novel work demonstrates a design for a highly efficient, compact, and scalable two-stage WESPs with minimum water consumption.

5.1 Background

Wet electrostatic precipitators (WESP) are attractive as they help circumvent the issues that degrade the performances of single and two-stage dry ESPs. WESPs continuously run films of a liquid, typically water, to wash captured particles off the collector plates. Key challenges, such as dry spots on collection plates, corrosion of collector plates, and importantly, high water consumption rate, remain in realizing efficient WESPs [102].

To mitigate dry spots and corrosion of collectors, previous studies proposed new collector materials and designs, such as membrane-based collection plates, which utilize capillary force to maintain uniform films of water over the entire collection area [103]–[105]. Bayless and colleagues [102] developed a parallel-plate, single-stage WESP using a membrane-based collection plate for collecting particles in the range of 1 to 25 μm and observed that the collection efficiency on average, was about 30% higher than that of dry ESPs with almost no attenuation in the collection efficiency for the smaller particles. Ali and colleagues [106] developed a single-stage, cross-flow WESP design with vertical columns of membrane cords supplied with water. They reported particle collection efficiencies greater than 80% for a particle size range of 1.61 μm to 8.84 μm. Neither studies, however, reported the collection efficiency for fine and ultrafine particles. [107] experimentally examined a cylindrical single-stage WESP and reported high

collection efficiencies for ultrafine particles (from 10 to 100 nm). However, the water-to-air flow rate ratio in their study was very high, ~ 0.9 (kg-water/kg-air).

To help mitigate the challenges of existing WESPs, we report a two-stage WESP design where an array of traveling liquid water beads on vertical cotton strings act as collection electrodes for a counterflowing exhaust gas stream. Our design provides competitive particle collection rates for fine and ultrafine particles while overcoming the limitations of existing WESPs. Our unique string-based design helps eliminate local dry spots on or contamination of surfaces. It also helps reduce water consumption rates significantly when compared with existing WESP devices.

We performed a combined experimental, theoretical, and numerical study to assess the performance of our device. Two different collection electrode configurations, cylindrical and linear, are implemented and examined in this work. The effects of the collector bias voltage, air velocity, and water flow rate per string on the collection performance were investigated experimentally and compared with theoretical predictions. The particle trajectories and the effects of the water flow rate are further studied using numerical simulation to help understand collection mechanisms in our string-based collectors.

5.2 Experimental setup, theoretical model, and numerical simulation

5.2.1 Experimental setup

Figure 5. 1 shows a schematic of the experimental setup used in this work to characterize the performance of our string-based two-stage WESPs. The experimental setup consists of four main sections: a diesel generator, a particle charging cell, a particle collector (cylindrical and linear configurations), and particle number concentration measurement systems.

A portable diesel generator (Sportsman GEN4000DF, 4 kW) was used as the DPM source in this study. As shown in Figure 5. 1, an indirect air-cooled heat exchanger was used to cool down the generator exhaust from about 200 to 350^{o}C down to less than 40^{o}C. The condensed water from this cooling process was then collected in an in-line container. This cooling was necessary to protect the polymeric components. The flow rate of the exhaust stream entering the charging cell was controlled using a flow diverter. The flow velocity in the charging region was varied from 0.7 to 2 m/s, which corresponds to the flow velocity range of 2 to 6 m/s in the collection region.

Two string-based collector configurations are tested in this work. The first design, hereinafter referred to as the linear collector, consists of five strings of diameter 0.76 mm, which are placed 5 mm apart in a single-line formation (Figure 5. 2(a)). This collector provides a 25 mm × 25 mm cross-sectional area for the air stream. The channel walls are made of a 3-mm-thick acrylic sheet. Two 0.5-mm-thick copper sheet are placed on the outside of the air channel as the high voltage electrode of the opposite polarity (see Figure 5. 2(a)). The second configuration was a cylindrical collector with a single vertical string at the center. The cylindrical collector provides a circular cross-section of 25 mm in diameter for the air stream. A transparent cylindrical tube with a wall

thickness of 3 mm was used to construct this collector. A copper sheet covering the outside of the cylinder acts as a counter electrode and provides a symmetric electric field around the string.

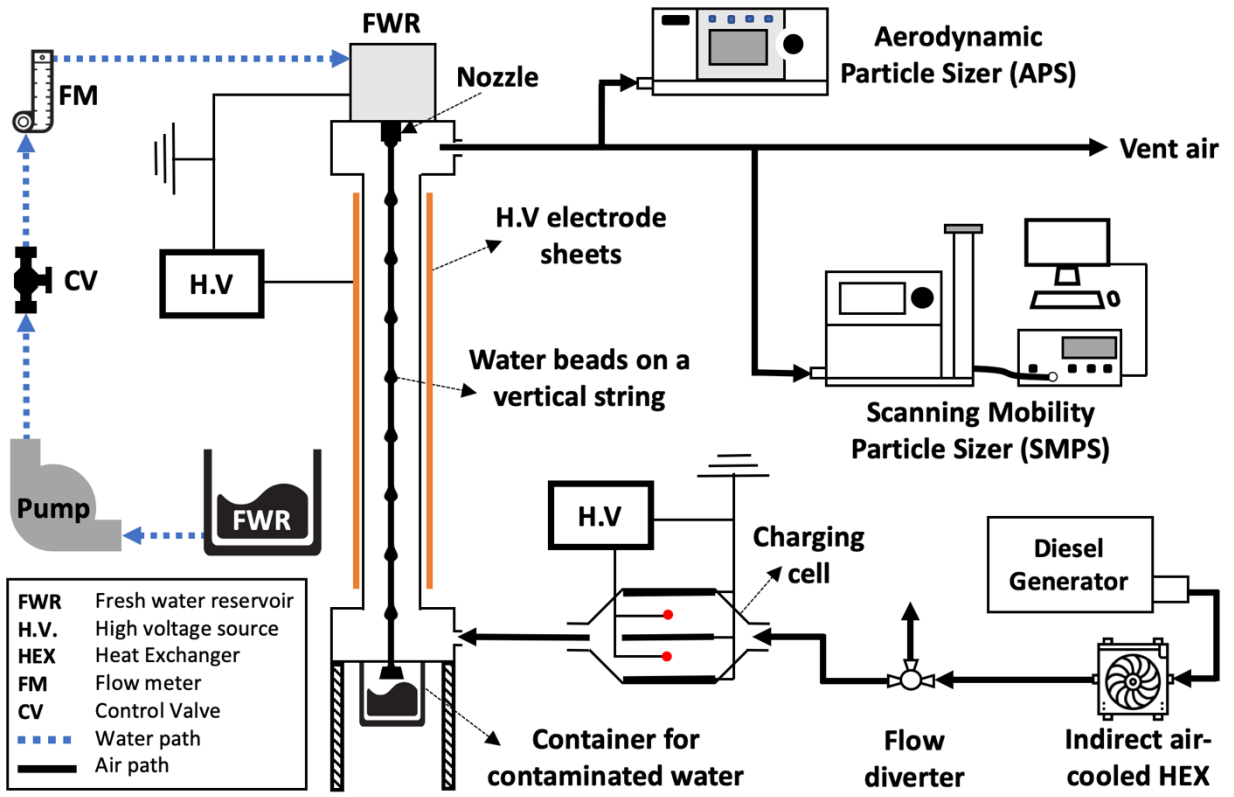

Figure 5. 1: Schematic of the experimental setup for characterizing the performance of the string-based collectors.

Both collectors are 0.6 m long. The copper sheets are connected to a variable voltage source, which is controlled to be in the range of 0 - 10 kV to investigate the effects of the collector voltage on the collection efficiency.

We use cotton fibers as strings in the present study. As shown in our previous works [85], [108], cotton threads absorb water and function as a super-hydrophilic surface. As a thin film of liquid flows down each string, intrinsic flow instability generates uniformly-spaced traveling water

beads. These beads help wash collected particles efficiently and mitigate the re-entrainment issue. It also helps to eliminate potential dry spots with minimal water usage. Water is supplied to the strings using stainless steel nozzles of 1.2 mm inner diameter connected to the top reservoir. The top water reservoir is grounded. A set of pumps and flow meters is used to control the flow of water to the top reservoir. The water flow rate per string is varied by controlling the liquid height in the top reservoir in the range of 0.01 to 0.135 g/s to investigate its effects on the collection efficiency. Water is collected at the bottom reservoir. A weight-scale with 0.1 gram precision is used to measure the water flow rate.

A particle charging cell (Figure 5. 2(c) and (d)) is used to charge particles in the exhaust gas stream. The charging cell consists of three grounded parallel aluminum plates with thickness, t_{Al}, of 2 mm and length, L_p, of 10 mm and two tungsten wires (200 μm in diameter) in between the plates. The plates are spaced 14 mm apart. Tungsten wires are connected to a high voltage source in the range of 0 - 20 kV. The applied voltage and the resulting corona current are measured using insulated digital multimeters. Since the cross-sectional area of the two collectors in this study are different, we designed two charging cells of different heights. The height of the charging cell, h_p, used for the cylindrical collector is 60 mm and the height of the charging cell for the linear collector is 80 mm. The other geometric parameters of the charging cells, L_p and w_p, are the same.

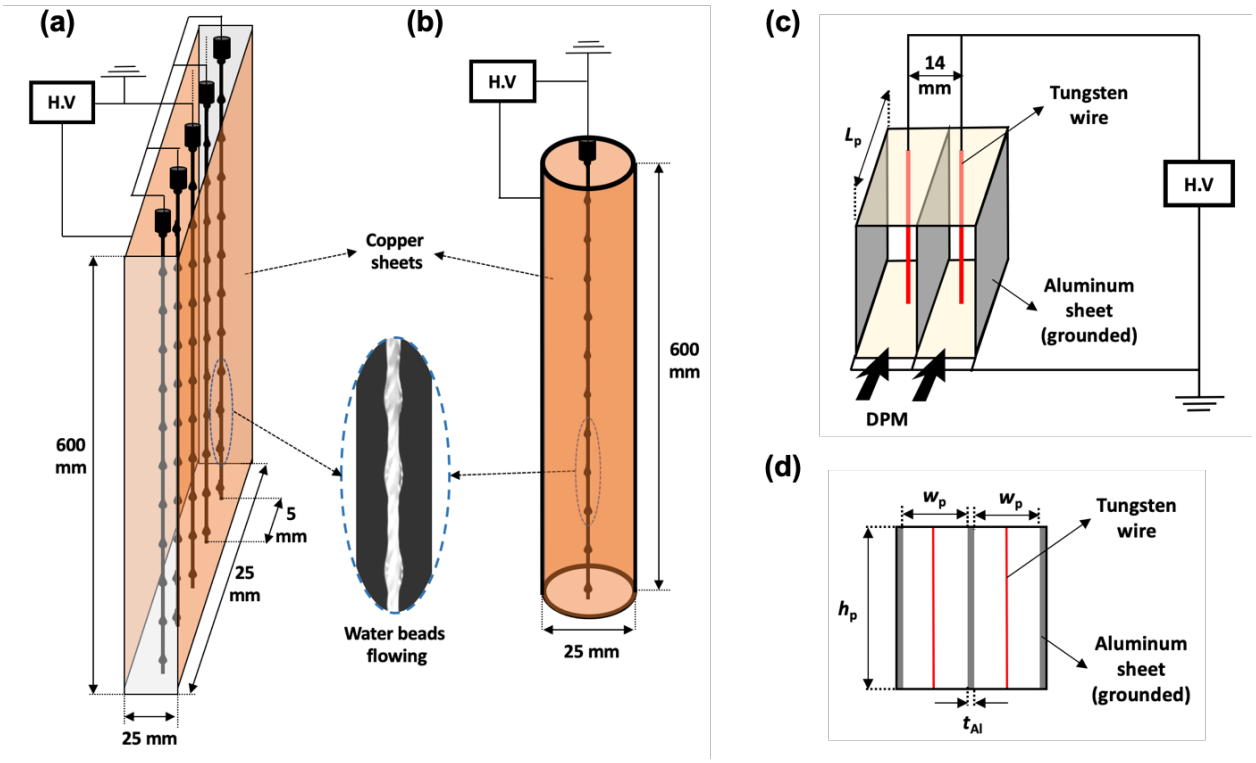

Figure 5. 2: Schematics of (a) the linear collector, (b) the cylindrical collector, (c) the charging cell. (d) The front view of the charging cell used in this study.

The DPM number size distributions were continuously monitored downstream of the collectors using two measurement systems: a SMPS (Scanning Mobility Particle Sizer; model 3080) and a CPC (Condensation Particle Counter; model 3787) for particles in the range of 10 nm to 300 nm and an APS (Aerodynamic Particle Sizer; model 3321) for particles in the range of 500 nm to 10 μm. Table 5. 1 summarizes the experimental conditions.

Table 5. 1: Parameters and test conditions used to study the string-based WESP performance.

Parameters	Conditions	Notes
Applied voltage [kV]	0 - 10	In collectors, ΔV_c
	7 - 7.6	In charging cell, ΔV_p

Air velocity [m/s]	2.3 – 4.5	In collector
	0.7 - 1.5	In charging cell
Water flow rate per string [g/s]	0.01 – 0.135	$\dot{m}_{Lps}$
Air inlet temperature [^{o}C]	30 - 40	---

The performance of our two-stage WESPs, expressed in terms of the fractional particle collection efficiency, η, is given by the following expression:

$$\eta = \left(1 - C_{on} / C_{off}\right) \times 100 \tag{5.1}$$

where C_{on} and C_{off} are the number concentration of the particles (particles/cm^3) in the power-off and power-on (in the charging cell or the collector) mode, respectively.

5.2.2 Theoretical modeling

Many previous studies investigated particle charging mechanisms and proposed various models[109]–[111]. Predictions of these models agree reasonably well with the experimental results. We use the Cochet's charging model, which was shown to be valid for the particle size range of our main concern (from 0.1 to 1 μm) [112], [113]. This model predicts the maximum charge, Q_p, on particles as [114]:

$$Q_p = \left[\left(1 + 2\lambda / d_p\right)^2 - \left(\frac{2}{1 + 2\lambda / d_p} \right) \left(\frac{\varepsilon_r - 1}{\varepsilon_r + 2} \right) \right] \pi \varepsilon_0 {d_p}^2 E_p \tag{5.2}$$

where λ is the mean free path of the gas molecules, d_p is the diameter of the particles, ε_r is the dielectric constant of the particles, ε_0 is the electrical permittivity of vacuum and E_p is the electrical

field in the particle charging cell. Note that, DPMs are not chemically homogenous. In the present work, we controlled ε_r as an adjustable parameter.

Past studies also proposed various models for particle collection in ESPs [115]–[117]. Deutsch presented a simplified model by assuming perfect mixing [118] and predicted the collection efficiency to be exponentially decaying in the flow direction:

$$\eta = 1 - \exp\left(\frac{\varpi_m L}{\overline{U}_a S}\right) \tag{5.3}$$

where ϖ_m is the theoretical migration velocity of particles toward the collection plate due to the electric field (m/s), L is the length of the collection plate in the flow direction, $\overline{U}_a$ is the mean velocity of the air stream, and S is the distance between the high-voltage electrode (copper sheets in this work) and the collection surface (strings). We obtain ϖ_m by balancing the Stokes' drag with the electrical force:

$$\varpi_m = \frac{Q_p E_c C_c}{3\pi\mu d_p} \tag{5.4}$$

where E_c is the pseudo-homogeneous electric field in the collector (V/m) and μ is the gas dynamic viscosity. C_c is the Cunningham correction factor, which is given as follows [119]:

$$C_c = 1 + 1.246\left(2\lambda/d_p\right) + 0.42\left(2\lambda/d_p\right).\exp\left[-0.87\left(d_p/2\lambda\right)\right] \tag{5.5}$$

5.2.3 Numerical simulation

To help interpret our experimental results, we also performed a simplified numerical simulation study of electrohydrodynamic (EHD) using a commercial software package [120]. The numerical simulation helps visualize particle trajectories in our string-based collection cells, and examine the charging and collection models presented in the previous section. Figure 5. 3 shows the numerical simulation domains used in the present study: a 3D domain (Figure 5. 3(a)) representing the linear collector and a 2D axisymmetric domain (Figure 5. 3(b)) representing the cylindrical collector with a string of radius, R_s, 0.38 mm at the center.

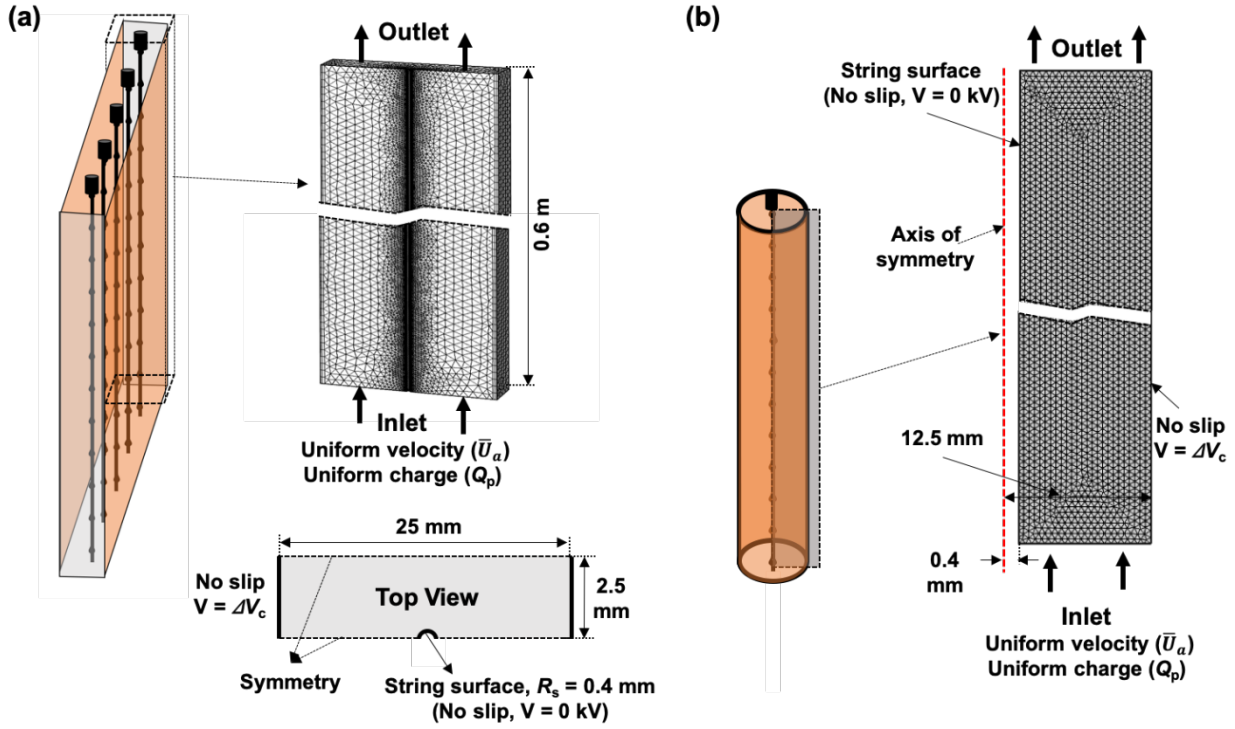

Figure 5. 3: Schematics of the numerical simulation domains for (a) the linear collector, and (b) the cylindrical collector.

We solve the steady, incompressible, Navier-Stokes equations [121], [122]:

$$\nabla.\vec{U}_a = 0 \tag{5.6}$$

$$\rho_a \vec{U}_a . \nabla \vec{U}_a = -\nabla p + \mu_a \nabla^2 \vec{U}_a - \rho_a \nabla V \tag{5.7}$$

where $\vec{U}_a$ is the velocity vector, p is the air pressure, V is the electric potential, and ρ_a and μ_a are the density and dynamics viscosity of air, respectively.

To predict the trajectory of charged particles in the collector, the following equation, which considers the effect of drag force, $\vec{F}_d$, buoyancy force, and Coulomb's force, $\vec{F}_e$, is numerically solved [123]:

$$m_p \frac{d\vec{U}_p}{dt} = \vec{F}_d + \frac{g\left(\rho_p - \rho_a\right)}{\rho_p} + \vec{F}_e \tag{5.8}$$

where m_p denotes the particle mass, g is the gravitational acceleration constant, and ρ_p is the particle density.

The drag force, $\vec{F}_d$, is calculated using [124]:

$$\vec{F}_d = \frac{1}{2} C_d S_p \rho_a \left|\vec{U}_p - \vec{U}_a\right| \left(\vec{U}_p - \vec{U}_a\right) \tag{5.9}$$

where $\vec{U}_p$ is the velocity of particles, S_p is the cross-section of particles in the air flow (= $\pi . d_\mathrm{p}^2/4$), and C_d is the drag coefficient [125]–[127], defined as follows:

$$C_d = \frac{24}{\mathrm{Re}_p} \tag{5.10}$$

Here, Re_p is the particle Reynolds number.

The electric force, $\vec{F}_e$, is obtained from:

$$\vec{F}_e = Q_p \vec{E}_c \tag{5.11}$$

where $\vec{E}_c$, the electric field vector in the collector, is obtained:

$$\vec{E}_c = -\nabla V \tag{5.12}$$

In the simulations, it is assumed that the gas and particle distributions at the inlet are uniform. The initial values for the number of charges on the particles are assigned based on Eq. 5.2. A mesh-independence study was performed to ensure numerical accuracy. A mesh-independence study was performed to ensure that the velocity and electric field distribution in the air stream and the number of collected particles do not change by more than 3% with further mesh refinement. The computational mesh for the 2D domain (cylindrical collector) and the 3D domain (5-strings collector) contain 80000 and 1950000 elements, respectively.

5.3 Results and discussion

5.3.1 DPM size distribution and electrical performance of the pre-charger

Figure 5. 4(a) shows the current-voltage relationship of the wire-plate charging cell. The corona onset voltage (COV) in our charging cell is 5.5 kV. Figure 5. 4(b) shows average over four experimental samples for DPM number size distribution measured at the inlet of the charging cell using SMSP and APS. Each SMPS data consists of 10 consecutive number size distribution measurements and each APS data includes ~200 consecutive measurements.

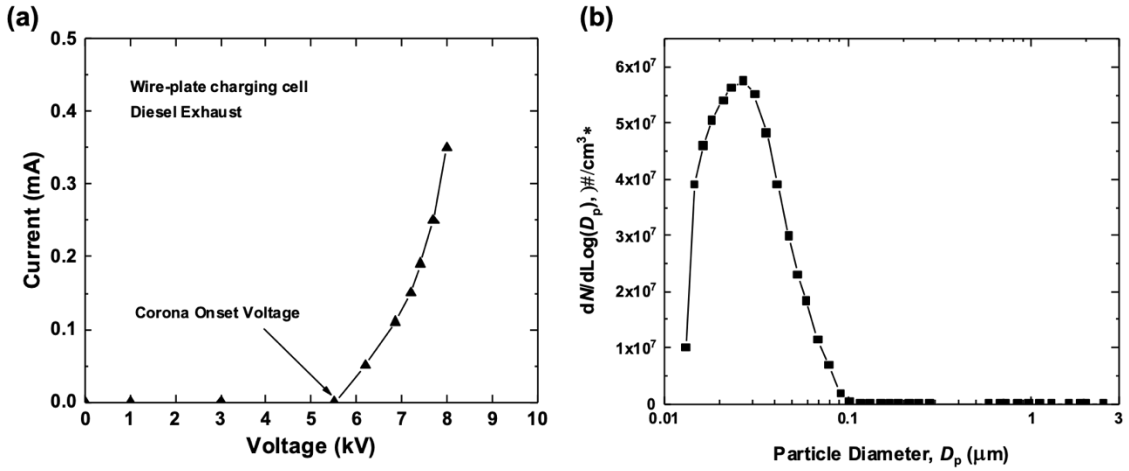

Figure 5. 4: (a) Voltage-current curve of the charging cell and (b) an average DPM size distribution at the inlet of the charging cell.

5.3.2 Effects of water flow rate

Figure 5. 5 shows the fractional collection efficiency of the two-stage WESP with a cylindrical collector for particles in the size range of 10 nm to 2.5 μm as a function of the particle diameter. The water flow rate per string, $\dot{m}_{\mathrm{Lps}}$, is varied in the range of 0.01 – 0.135 g/s. The air velocities in the charging cell and the collection zone were maintained at 1 and 3 m/s, respectively. The charging cell and the cylindrical collector bias voltage were 7.4 kV and 10 kV, respectively. The results indicate that increasing the water flow rate per string has insignificant effect on the collection efficiency.

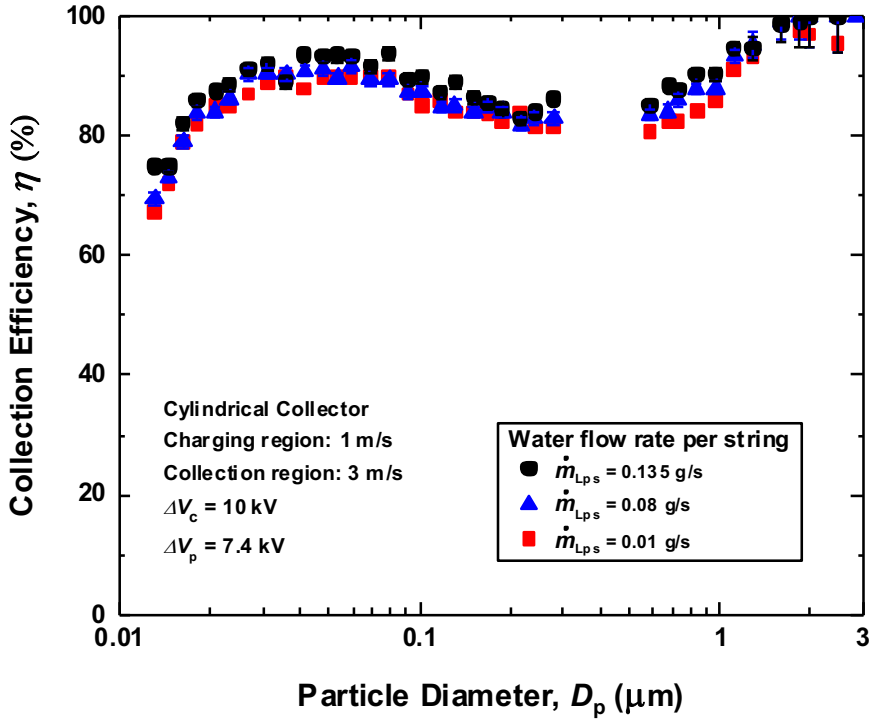

Figure 5. 5: Effect of water flow rate per string on the experimental fractional collection efficiency of the cylindrical collector

As mentioned before, water consumption necessary for cleaning the collection plates is an important metric in WESPs. We use the water-to-air mass flow rate ratio [kg-water/kg-air] as the performance metric. Figure 5. 6 shows the fractional collection efficiency of our design compared with that of other WESP designs as a function of the water-to-air mass flow rate ratio. Our string-based collector offers comparable collection efficiencies over a wide range of particle diameters with water-to-air mass flow rate ratios at least three times smaller. This reduction in the water consumption rate is achieved by the longer residence time provided in our design for the particle collection. One might argue that the longer gas residence times can be achieved by increasing the collector size. This, however, increases initial manufacturing costs.

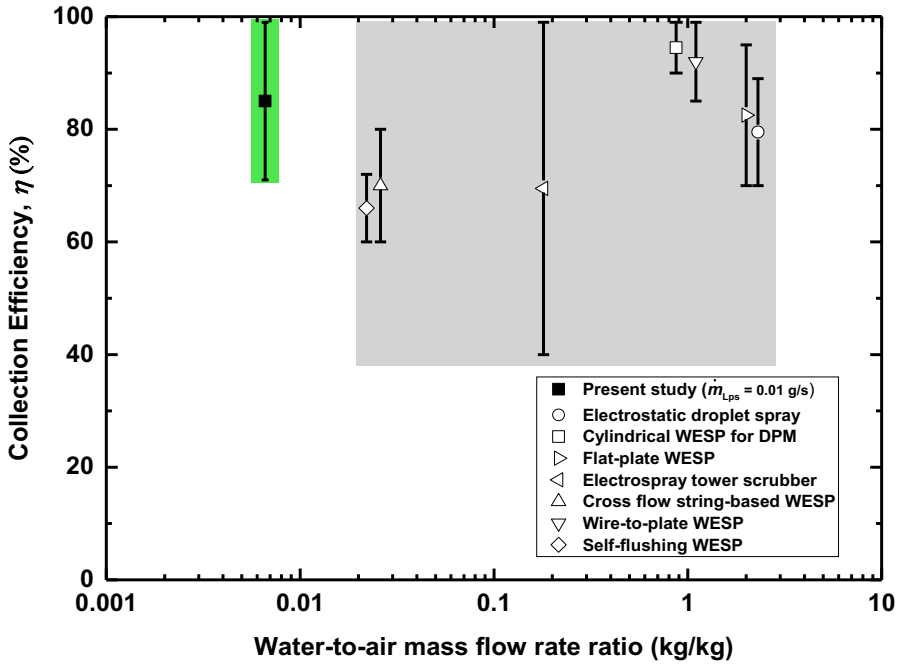

Figure 5. 6: Collection efficiencies as a function of the water-to-air mass flow rate ratio for different WESP devices. We compare our device with previously reported WESP devices; electrostatic droplet spray [128], cylindrical WESP for DPM [107], flat-plate WESP [129], electrospray tower scrubber [130], cross flow string-based WESP [106], wire-to-plate WESP [37], and self-flushing WESP [131].

We compare the air flow rate per unit collector volume as another useful metric. Table 5. 2 shows the air flow rate per unit collector volume of our and previously reported WESPs together with the corresponding experimental conditions, particle diameter ranges, and collection efficiencies. This comparison shows that the present string-based collector can achieve over 70%

collection efficiencies at much higher air flow rates per unit volume of the collector and at a much lower water consumption rate.

Table 5. 2: Comparison of experimental conditions and results in the present work with those of previous WESP designs.

Collection type	Particle diameter [μm]	Water flow rate [kg/s]	Air flow rate [kg/s]	Air velocity [m/s]	Air flow rate /collector volume [(m^3/s) /m^3]
Electrostatic droplet spray[128]	0.3-4	0.139	0.066	0.2	0.003
Cylindrical WESP [107]	0.02-0.8	0.05	0.056	2.3	2.5
Flat-plate WESP [129]	0.02-0.5	0.003	0.0016	1	2.4
Electrospray tower scrubber[130]	0.07-10	0.0013	0.0076	0.8	1.4
Cross flow string based WESP[106]	1.61-8.84	0.04	3.24	3	1.25
Wire-to-plate WESP [37]	0.02-9	0.03	0.03	1.16	1.1
Self-flushing WESP [131]	0.07-2.5	0.007	0.031	3	1
String-based Cylindrical WESP (Present study)	0.01-2.5	10^{-5}	0.0015	3	4.36

5.3.3 Effects of collector bias voltage

Figure 5. 7 shows the fractional collection efficiency as a function of the particle size for the cylindrical and the linear collector under different collector bias voltages. Also shown are the collection efficiencies predicted using eqs 5.2-5.5. A 7.2 kV charging voltage was used in the charging cell and the water flow rate per string, $\dot{m}_{Lps}$, was 0.06 g/s. Increasing the collector bias

voltage, ΔV_c, increases the particle collection efficiency for all particles larger than approximately 30 nm in diameter. However, for particles smaller than ~30 nm in diameter, the applied collector voltage has an insignificant effect on the collection efficiency. This behavior, which has also been reported in earlier studies [129], [132], [133], is due to the fractional charging effect. These ultrafine particles have an average acquired elementary charge of less than one. This means that some of these particles do not acquire any charge in the charging cell and are not collected efficiently, regardless of the collector bias voltage, ΔV_c. In fact, for particles smaller than approximately 30 nm in diameter, the partial charging and lower ion attachment coefficients result in decrease in the collection efficiency with decreasing particle sizes [134]–[136].

Figure 5. 7 shows that, under the experimental conditions used in the present study, the experimental fractional collection efficiency of particles larger than 100 nm agrees well with the prediction (Deutsch collection theory) based on Cochet's charging model. However, due in part to the limitation of Cochet's assumption of infinite particle charging time, the agreement is poor for particles smaller than 100 nm. For larger particles where the field charging mechanism dominates, the assumption of infinite charging time is adequate as they readily reach saturation charge [45]. However, for ultrafine particles where the diffusion charging is the dominant mechanism, longer relaxation time is required to gain sufficient charge, especially as particles become smaller (Adachi et al. 1985; Pui et al. 1988; White 1951).

The collection efficiency of the cylindrical collector is similar to that of the linear collector under similar operating conditions. This implies that asymmetric electric fields in the linear collector have a small influence on the overall performance. The linear collector requires higher

water-to-air mass flow rate ratios than the cylindrical collector. But, it requires fewer electrode sheets per unit foot print of the device, which makes it attractive for larger scale applications.

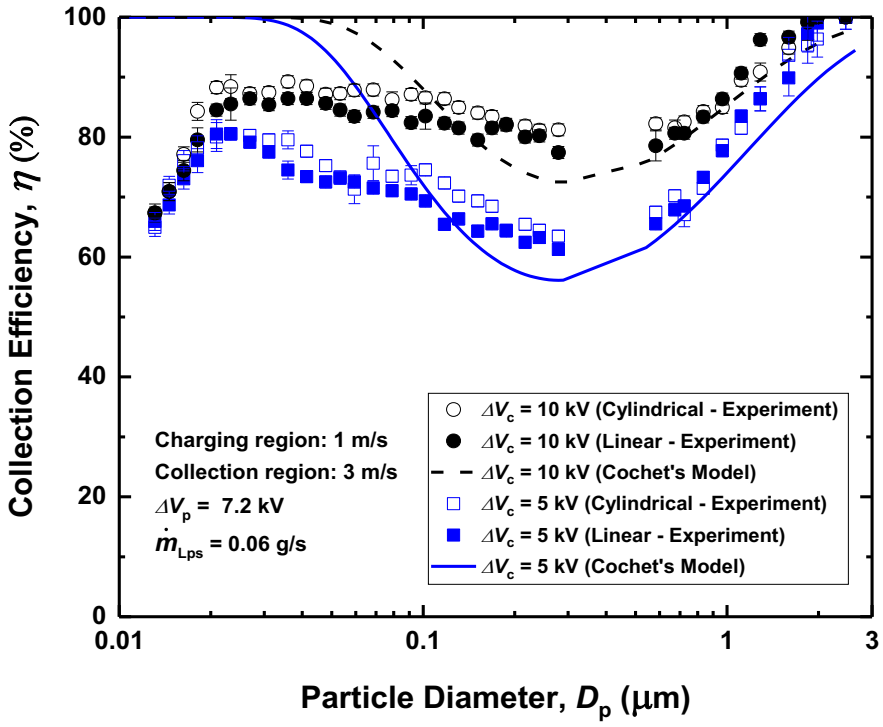

Figure 5. 7: Experimentally measured and predicted (Cochet's model) fractional collection efficiencies for the cylindrical and the linear collectors at different collector bias voltages. The experimental and predicted values are presented as the symbols and the lines, respectively.

In the two-stage ESP applications, it is important to minimize particle deposition on the ground electrodes in the charging cell to mitigate long term efficiency reduction. Our results indicate that, for charging voltage, ΔV_p, of 7.6 kV, less than 20% of particles within the particle size range of 10 nm to 2.5 μm are collected on the ground electrodes of the charging cell.

5.3.4 Effects of air stream velocity

Figure 5. 8 shows the experimentally measured and predicted (using eqs 5.2-5.5) fractional collection efficiency for the cylindrical and the linear collectors as a function of the particle diameter for different air flow rates. In these experiments, the water flow rate per string, $\dot{m}_{Lps}$, was fixed at 0.06 g/s. The air stream velocity in the collector was varied in the range of 2.3 – 4.5 m/s, and the bias voltages for the charging cell and the collectors were 7.4 kV and 10 kV, respectively. The smaller air stream velocities result in larger fractional collection efficiencies for the entire range of particle diameters due to the longer residence times provided for both charging and collection processes. The comparison of the collection efficiencies obtained from the models (eqs 5.2-5.5) with those of experiments in Figure 5. 8 shows similar trends to those observed in Figure 5. 7.

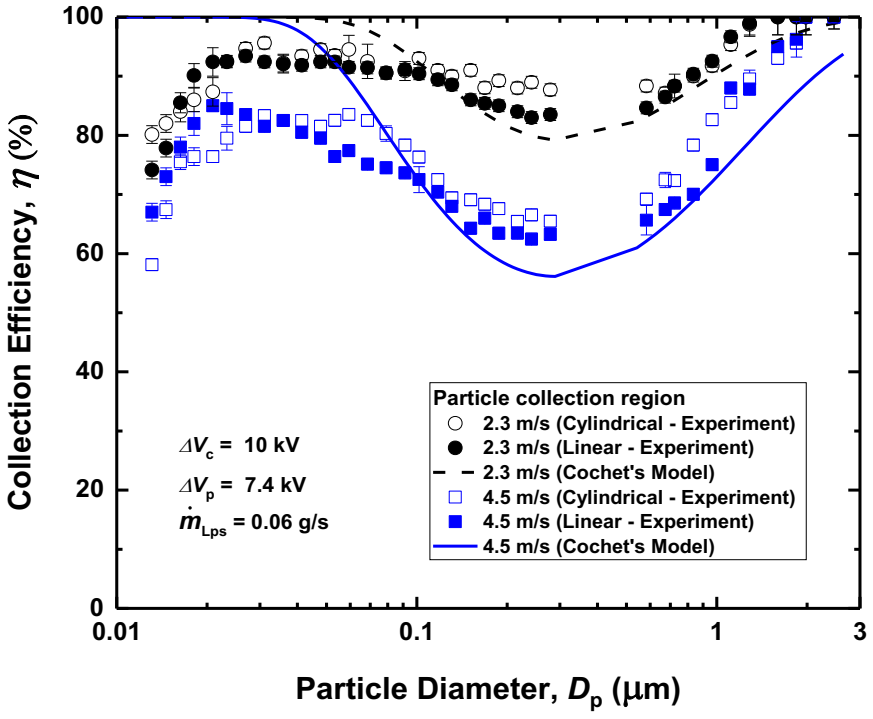

Figure 5. 8: Effect of the gas residence time in the collector on the experimentally measured and predicted (Cochet's model) fractional collection efficiencies for the cylindrical and the linear collectors. The experimental results and predicted values are presented as the symbols and the lines, respectively.

5.3.5 Numerical simulation results

We performed numerical simulation to help further elucidate particle collection mechanisms in our string-based collectors. Figure 5. 9(a) illustrates representative particle trajectories in the cylindrical collector under the bias voltage, ΔV_c, of 10 kV. The air is flowing upward at a velocity of 3 m/s, the diameter of particles is 0.101 μm, the average number of elementary charges on each particle is 11.5, and the total number of particles released at the inlet is 100. The color bar indicates the magnitudes of particle velocities. The average speed of particles increases as particles travel

downstream due to the acceleration of particles in the radial direction caused by the electric field. The maximum particle velocity at the outlet is ~4.2 m/s.

We employ a trial and error procedure to estimate the average number of charges per particle, n_p. This is, for particles of a given diameter, we adjust the corresponding n_p until the fractional collection efficiency obtained in our numerical simulation matches the experimental results (blue triangles in Figure 5. 9(b)). The fractional collection efficiency is calculated by dividing the number of particles that reach the surface of the string by the total number of particles released at the inlet. The prediction from Cochet's model agrees to within 15% with our results for particles larger than approximately 100 nm (Figure 5. 9(b)). Cochet's model, however, over predicts n_p for smaller particles. For the smallest particles, our results indicate partial charging ($n_p < 1$), consistent with the earlier observation from Figure 5. 7. The average numbers of charges obtained from the linear and cylindrical collectors are comparable, differing by less than 5%.

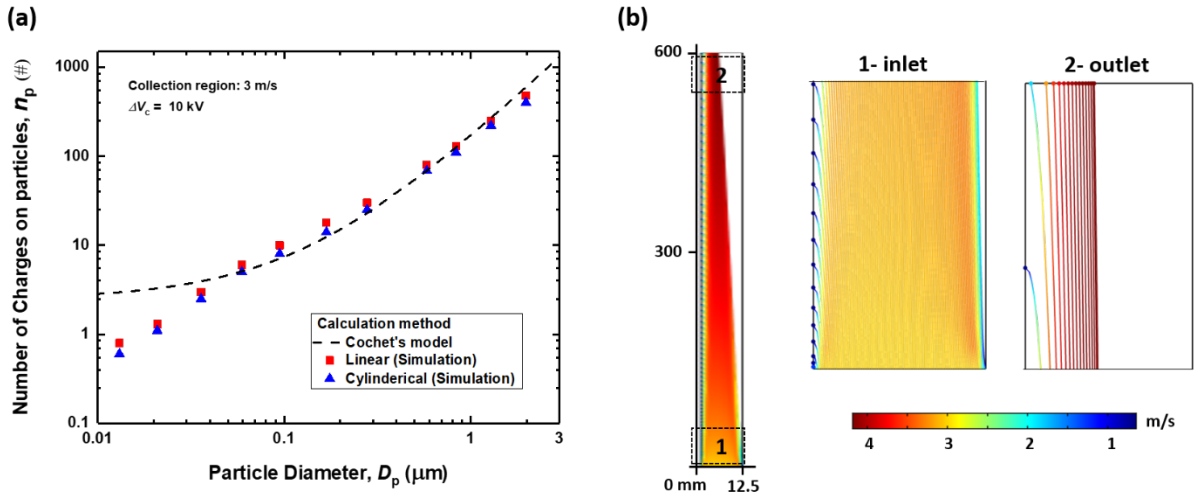

Figure 5. 9: (a) Numbers of charges on particles obtained using our numerical simulation and using Cochet's model as a function of the particle size. The numerical simulation and the Cochet's model results are presented as the symbols and the dashed line, respectively, and (b) Numerically

simulated particle trajectories in the cylindrical collector (domain size = 12.5 mm × 600 mm, inlet airflow velocity = 3 m/s, number of particles at inlet = 100, particle diameter, d_p = 0.101 μm, average number of charges on the particle, Q_p = 11.5, applied voltage = 10 kV).

We performed a systematic numerical simulation study to help investigate the effects of the bead density and water flow rate on the collection efficiency. As discussed in our previous work [108], as the water flow rate increases, the water bead spacing, S_b, decreases. We vary the water flow rate from 0.01 g/s to 0.135 g/s per string, which, in turn, leads to bead spacing in the range of 20 to 360 mm. Figure 5. 10(a) shows the numerical simulation domain for the cylindrical collector with bead profiles along the string. The bead length, L_b, and the bead thickness, t_b, are set to 4 and 1.5 mm, respectively, based on the experimental observations.

Figure 5. 10(b) shows the effect of water flow rate per string on the experimentally obtained bead spacing, S_b, and the particle collection efficiency obtained from numerical simulations. In the numerical simulation, particle diameter, d_p was 0.101 μm and inlet airflow velocity was 3 m/s. The average number of charges on the particle, Q_p, was set to 11.5, as shown in Figure 5. 9(b). Figure 5. 10(b) indicates that increasing the water flow rate per string, significantly decreases the bead spacing, while the fractional collection efficiency remains the same. The experimental and numerical simulation results indicate that using our string-based counterflow collector, high particle collection efficiencies can be obtained with water-to-air flow rate ratios as low as ~0.0066 kg/kg.

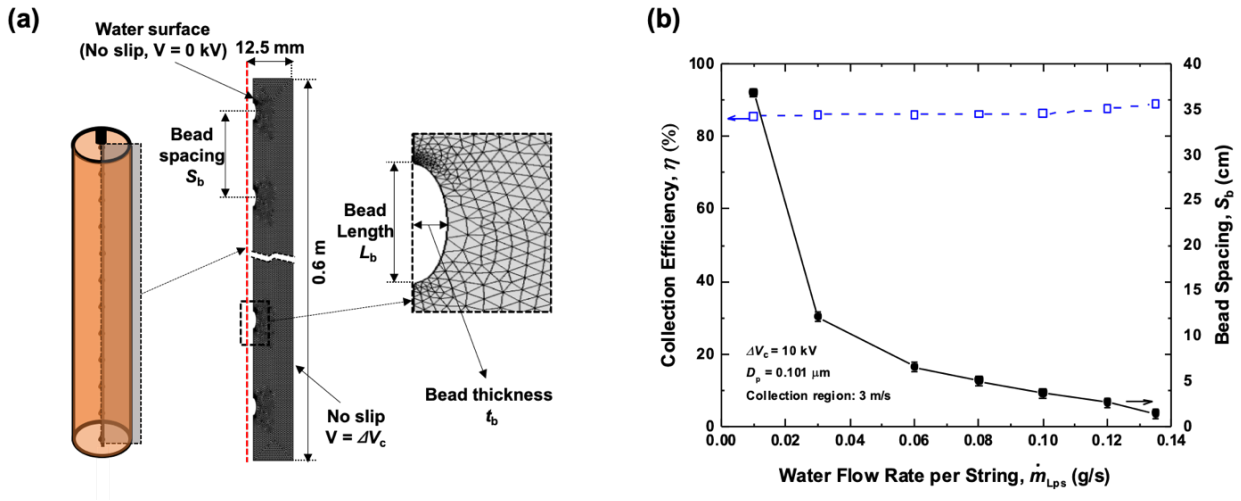

Figure 5. 10: (a) Schematics of the numerical simulation domain for the cylindrical collector with bead profiles along the string. (b) Effect of water flow rate per string on the bead spacing (obtained from experiments) and collection efficiency (obtained from numerical simulation for particles with 0.101 μm diameter).

The presented numerical simulation provides a simple method to understand the collection mechanism and predict particle trajectories in our symmetric and asymmetric designs. The assumptions and simplifications made in this study can be modified in future studies to implement further improvements to obtain closer match between numerical simulation and experiment for ultrafine particles. In particular, the uniform distribution of particles at the inlet can be replaced by a more realistic profile. Also, the charging mechanism in our wire-plate particle charger can be simulated more accurately by including field and diffusion charging mechanisms.

5.4 Summary

In summary, we experimentally and numerically studied a novel counter-flow WESP design consisting of vertical cotton strings. The strings are continuously supplied with water and act as collection plates for particles in a diameter range of 10 nm to 2.5 μm. To quantify the performance

of our string-based WESPs, fractional collection efficiency was experimentally determined using a set of APS and SMPS. Moreover, the effect of water flow rate on particle collection efficiency was examined experimentally and validated by numerical simulations. We show that for water flow rate per string, $\dot{m}_{\mathrm{Lps}}$, larger than 0.01 g/s, corresponding to water-to-air flow rate ratio of ~0.007 kg/kg, $\dot{m}_{\mathrm{Lps}}$ has negligible effects on the collection efficiency of our particle collector. Experimental results show that the increase in the collector bias voltage as well as the air residence time in the collector results in the increase of the collection efficiency.

We also show that, compared to previously reported WESP devices, our string-based design can achieve higher collection efficiencies with significantly lower water-to-air flow rate ratios. The present study demonstrates a string-based counterflow collector with a superior performance in various aspects, such as particle collection efficiency, water consumption, and collector volume for applications in WESPs to remove fine and ultrafine particles from a polluted air stream.

Chapter 6

Summary and future work recommendations

6.1 Summary

This dissertation presents a study of characteristics and applications of liquid films flowing down vertical fibers. We started this investigation with a combined experimental and numerical study of viscous flows down highly curved surfaces, focusing on the effect of nozzle geometry on the dynamics of the downstream flow, which has been largely overlooked in previous studies. We limited the experiments to the Rayleigh−Plateau (RP) instability regime, which generates uniformly-spaced liquid beads on vertical fibers. Our experimental and numerical results indicated that the nozzle geometry has a substantial effect on the pattern and characteristics of the downstream flow, such as size, spacing and traveling speed of the generated beads. We identified the thickness of the nearly flat region of the liquid flow after the nozzle, which is termed preinstablity thickness, as a critical parameter in governing the characteristics of the flow. We also developed semi-empirical models to accurately predict the liquid bead characteristics as a function of the preinstability thickness.

We then presented a theoretical model based on the lubrication theory that includes various curvature terms, slip boundary conditions and a newly defined film stabilization term, to better understand the effect of nozzle geometry on the flow regime. Our theoretical modeling results showed remarkable agreement with experiments in terms of bead spacing, bead traveling speed,

and film profile within the preinstability region. The effect of film stabilization term on the dynamics of the flow was also investigated.

We then extended our study of the instability in thin films flowing down vertical fibers from high-viscosity liquids to that of a high–surface energy low-viscosity liquid (i.e. water) along cotton threads. We demonstrated a first-ever stable flow of controllable water beads along a vertical cotton string. We then constructed a multi-string condenser, in which water beads on a massive array of cotton strings are used to capture water vapor from a counterflowing humid air stream. We then experimentally studied the effects of water flow rate, and air velocity on the condensation rates and air-stream pressure drops. This study shows that our multi-string dehumidifier can deliver condensation rates per volume of almost three times higher than the best reported values, while substantially reducing the air-stream pressure drop.

We finally adapted our multi-string water vapor capturing structure for particle collection purposes. In this new design, water beads on electrically grounded cotton strings are used for capturing the pre-charged particles in a counterflowing air stream. We constructed a cylindrical and a linear configuration collector. We also performed a combination of experimental and numerical investigation to optimize the design in terms of water flow rate. Our study demonstrates that our string-based counterflow particle collector exhibits comparable collection efficiencies compared to the previous studied designs at significantly lower water consumption rates.

6.2 Future work recommendations

The following are the recommendations for extending the fundamental studies and the application analysis in the present work for flow of various liquids along vertical fibers:

6.2.1 A comprehensive flow regime map

As discussed in chapter 2 and 3, we performed a combination of experimental, numerical and theoretical modeling study to study the effect of nozzle geometry on the pattern and characteristics of a liquid flow along a vertical fiber. However, a comprehensive flow regime map is still needed to predict the flow pattern based on the experimental conditions, such as liquid flow rate, liquid properties, fiber diameter, and nozzle geometry. The proposed flow regime map enables researchers in the field to better understand the flow of liquid along a vertical fiber. Also, a simplified physics-based theoretical model, capable of predicting the flow properties, such as bead spacing, size, traveling speed and frequency, is needed to help researchers efficiently optimize the multi-string design for various applications.

6.2.2 Designing a multi-extraction Humidification-Dehumidification desalination system using the multi-string configuration

As discussed in chapter 4 and in our previous work [85], our multi-string humidifier/dehumidifier configuration, compared to the existing designs, exhibits superior performance in terms of evaporation/condensation rates per volume of the device with significantly lower air-stream pressure drop. We propose a rigorous study of an integrated multi-string desalination system, where the humidified air from the outlet of our multi-string evaporator enters the multi-string dehumidifier to complete the fresh-water production cycle. This study would build upon this dissertation to experimentally examine the effect of air flow rate, water flow rate, inlet air and water temperatures, string pitch, and device height on the gained output ratio (GOR) of the desalination system. Previous studies suggested that by introducing extractions from the humidifier air stream, one can increase the HDH performance [79]. However, there is still lack

of a rigorous experimental study on the effect of single/multiple extraction on the GOR of HDH desalination system. Also, a systematic study on the nozzle size selection is required to help mitigate the nozzle clogging issue in the multi-string humidifier.

References

[1] Z. Zeng, G. Warrier, and Y. S. Ju, "Study of the Fluid Dynamics of Thin Liquid Films Flowing Down a Vertical String With Counterflow of Gas," p. V08BT10A054, Nov. 2015, doi: 10.1115/IMECE2015-53132.

[2] K. Hattori, M. Ishikawa, and Y. H. Mori, "Strings of liquid beads for gas-liquid contact operations," *AIChE J.*, vol. 40, no. 12, pp. 1983–1992, 1994, doi: 10.1002/aic.690401209.

[3] H. Chinju, K. Uchiyama, and Y. H. Mori, "'String-of-beads' flow of liquids on vertical wires for gas absorption," *AIChE J.*, vol. 46, no. 5, pp. 937–945, 2000.

[4] J. Grünig, E. Lyagin, S. Horn, T. Skale, and M. Kraume, "Mass transfer characteristics of liquid films flowing down a vertical wire in a counter current gas flow," *Chem. Eng. Sci.*, vol. 69, no. 1, pp. 329–339, Feb. 2012, doi: 10.1016/j.ces.2011.10.049.

[5] T. Nozaki, N. Kaji, and Y. H. Mod, "Heat Transfer to a Liquid Flowing Down Vertical Wires Hanging in a Hot Gas Stream: an Experimental Study of a New Means of Thermal Energy Recovery," *HEAT Transf.*, vol. 6, pp. 63–68, 1998.

[6] K. Uchiyama, H. Migita, R. Ohmura, and Y. H. Mori, "Gas absorption into 'string-of-beads' liquid flow with chemical reaction: application to carbon dioxide separation," *Int. J. Heat Mass Transf.*, vol. 46, no. 3, pp. 457–468, Jan. 2003, doi: 10.1016/S0017-9310(02)00301-0.

[7] H. Migita, K. Soga, and Y. H. Mori, "Gas absorption in a wetted-wire column," *AIChE J.*, vol. 51, no. 8, pp. 2190–2198, Aug. 2005, doi: 10.1002/aic.10483.

[8] S. G. Pakdehi and S. Taheri, "Separation of Hydrazine from Air by Wetted Wire Column," *Chem. Eng. Technol.*, vol. 33, no. 10, pp. 1687–1694, Oct. 2010, doi: 10.1002/ceat.201000070.

[9] S. M. Hosseini, R. Alizadeh, E. Fatehifar, and A. Alizadehdakhel, "Simulation of gas absorption into string-of-beads liquid flow with chemical reaction," *Heat Mass Transf.*, vol. 50, no. 10, pp. 1393–1403, Apr. 2014, doi: 10.1007/s00231-014-1343-z.

[10] Z. Zeng, G. Warrier, and Y. S. Ju, "Flow and Heat Transfer in Liquid Films Flowing Over Highly Curved Surfaces," p. V002T06A012, Jul. 2015, doi: 10.1115/IPACK2015-48149.

[11] Z. Zeng, A. Sadeghpour, G. Warrier, and Y. S. Ju, "Experimental study of heat transfer between thin liquid films flowing down a vertical string in the Rayleigh-Plateau instability regime and a counterflowing gas stream," *Int. J. Heat Mass Transf.*, vol. 108, Part A, pp. 830–840, May 2017, doi: 10.1016/j.ijheatmasstransfer.2016.12.066.

[12] J. W. Strutt and Lord Rayleigh, "On the instability of jets," *Proc Lond. Math Soc*, vol. 10, no. 4, 1878.

[13] G. Grabbert and G. Wünsch, "Zur Hydraulik stark gekrümmter Rieselfilme," *Freib. Forschungshefte A*, vol. 517, pp. 61–83, 1973.

[14] Yu. Ya. Trifonov, "Steady-state traveling waves on the surface of a viscous liquid film falling down on vertical wires and tubes," *AIChE J.*, vol. 38, no. 6, pp. 821–834, Jun. 1992, doi: 10.1002/aic.690380604.

[15] D. Quéré, "Thin Films Flowing on Vertical Fibers," *EPL Europhys. Lett.*, vol. 13, no. 8, p. 721, Dec. 1990, doi: 10.1209/0295-5075/13/8/009.

[16] D. Quéré, "Fluid Coating on a Fiber," *Annu. Rev. Fluid Mech.*, vol. 31, no. 1, pp. 347–384, 1999, doi: 10.1146/annurev.fluid.31.1.347.

[17] S. Kalliadasis and H.-C. Chang, "Drop formation during coating of vertical fibres," *J. Fluid Mech.*, vol. 261, pp. 135–168, Feb. 1994, doi: 10.1017/S0022112094000297.

[18] C. Duprat, C. Ruyer-Quil, and F. Giorgiutti-Dauphiné, "Spatial evolution of a film flowing down a fiber," *Phys. Fluids*, vol. 21, no. 4, p. 042109, Apr. 2009, doi: 10.1063/1.3119811.

[19] C. Ruyer-Quil, P. Treveleyan, F. Giorgiutti-Dauphiné, C. Duprat, and S. Kalliadasis, "Modelling film flows down a fibre," *J. Fluid Mech.*, vol. 603, pp. 431–462, 2008, doi: 10.1017/S0022112008001225.

[20] M. M. Mekonnen and A. Y. Hoekstra, "Four billion people facing severe water scarcity," *Sci. Adv.*, vol. 2, no. 2, p. e1500323, Feb. 2016, doi: 10.1126/sciadv.1500323.

[21] A. R. Parker and C. R. Lawrence, "Water capture by a desert beetle," *Nature*, vol. 414, pp. 33–34, Nov. 2001, doi: 10.1038/35102108.

[22] F. Fathieh, M. J. Kalmutzki, E. A. Kapustin, P. J. Waller, J. Yang, and O. M. Yaghi, "Practical water production from desert air," *Sci. Adv.*, vol. 4, no. 6, p. eaat3198, Jun. 2018, doi: 10.1126/sciadv.aat3198.

[23] M. Damak and K. K. Varanasi, "Electrostatically driven fog collection using space charge injection," *Sci. Adv.*, vol. 4, no. 6, p. eaao5323, Jun. 2018, doi: 10.1126/sciadv.aao5323.

[24] A. Giwa, N. Akther, A. A. Housani, S. Haris, and S. W. Hasan, "Recent advances in humidification dehumidification (HDH) desalination processes: Improved designs and productivity," *Renew. Sustain. Energy Rev.*, vol. 57, pp. 929–944, May 2016, doi: 10.1016/j.rser.2015.12.108.

[25] Z. Zeng, A. Sadeghpour, and Y. S. Ju, "Thermohydraulic characteristics of a multi-string direct-contact heat exchanger," *Int. J. Heat Mass Transf.*, vol. 126, pp. 536–544, Nov. 2018, doi: 10.1016/j.ijheatmasstransfer.2018.05.060.

[26] R. Prasad and V. R. Bella, "A Review on Diesel Soot Emission, its Effect and Control," *Bull. Chem. React. Eng. Catal.*, vol. 5, no. 2, pp. 69–86, Jan. 2011, doi: 10.9767/bcrec.5.2.794.69-86.

[27] T. W. Hesterberg, C. M. Long, W. B. Bunn, S. N. Sax, C. A. Lapin, and P. A. Valberg, "Non-cancer health effects of diesel exhaust: a critical assessment of recent human and animal toxicological literature," *Crit. Rev. Toxicol.*, vol. 39, no. 3, pp. 195–227, 2009, doi: 10.1080/10408440802220603.

[28] J. Lewtas, "Air pollution combustion emissions: characterization of causative agents and mechanisms associated with cancer, reproductive, and cardiovascular effects," *Mutat. Res.*, vol. 636, no. 1–3, pp. 95–133, Dec. 2007, doi: 10.1016/j.mrrev.2007.08.003.

[29] A. Karanasiou, M. Viana, X. Querol, T. Moreno, and F. de Leeuw, "Assessment of personal exposure to particulate air pollution during commuting in European cities—Recommendations and policy implications," *Sci. Total Environ.*, vol. 490, pp. 785–797, Aug. 2014, doi: 10.1016/j.scitotenv.2014.05.036.

[30] P. Pant, G. Habib, J. D. Marshall, and R. E. Peltier, "PM2.5 exposure in highly polluted cities: A case study from New Delhi, India," *Environ. Res.*, vol. 156, pp. 167–174, Jul. 2017, doi: 10.1016/j.envres.2017.03.024.

[31] D. Y. H. Pui, S.-C. Chen, and Z. Zuo, "PM2.5 in China: Measurements, sources, visibility and health effects, and mitigation," *Particuology*, vol. 13, pp. 1–26, Apr. 2014, doi: 10.1016/j.partic.2013.11.001.

[32] Z. D. Ristovski *et al.*, "Respiratory health effects of diesel particulate matter," *Respirol. Carlton Vic*, vol. 17, no. 2, pp. 201–212, Feb. 2012, doi: 10.1111/j.1440-1843.2011.02109.x.

[33] M. Fiebig, A. Wiartalla, B. Holderbaum, and S. Kiesow, "Particulate emissions from diesel engines: correlation between engine technology and emissions," *J. Occup. Med. Toxicol. Lond. Engl.*, vol. 9, p. 6, Mar. 2014, doi: 10.1186/1745-6673-9-6.

[34] M. M. Maricq, "On the electrical charge of motor vehicle exhaust particles," *J. Aerosol Sci.*, vol. 37, no. 7, pp. 858–874, Jul. 2006, doi: 10.1016/j.jaerosci.2005.08.003.

[35] C. Carotenuto, F. Di Natale, and A. Lancia, "Wet electrostatic scrubbers for the abatement of submicronic particulate," *Chem. Eng. J.*, vol. 165, no. 1, pp. 35–45, Nov. 2010, doi: 10.1016/j.cej.2010.08.049.

[36] C. A. Pope *et al.*, "Lung cancer, cardiopulmonary mortality, and long-term exposure to fine particulate air pollution," *JAMA*, vol. 287, no. 9, pp. 1132–1141, Mar. 2002, doi: 10.1001/jama.287.9.1132.

[37] Z. Yang *et al.*, "Fine particle migration and collection in a wet electrostatic precipitator," *J. Air Waste Manag. Assoc.*, vol. 67, no. 4, pp. 498–506, Apr. 2017, doi: 10.1080/10962247.2016.1260074.

[38] D. W. Dockery *et al.*, "An association between air pollution and mortality in six U.S. cities," *N. Engl. J. Med.*, vol. 329, no. 24, pp. 1753–1759, Dec. 1993, doi: 10.1056/NEJM199312093292401.

[39] Z. Ning, C. S. Cheung, and S. X. Liu, "Experimental investigation of the effect of exhaust gas cooling on diesel particulate," 2004, doi: 10.1016/j.jaerosci.2003.10.001.

[40] K.-H. Kim, E. Kabir, and S. Kabir, "A review on the human health impact of airborne particulate matter," *Environ. Int.*, vol. 74, pp. 136–143, Jan. 2015, doi: 10.1016/j.envint.2014.10.005.

[41] HEI, "Understanding the health effects of ambient ultrafine particles," Health Effects Institute, Boston, MA, HEI Perspectives 3, 2013.

[42] S. Ohlwein, R. Kappeler, M. Kutlar Joss, N. Künzli, and B. Hoffmann, "Health effects of ultrafine particles: a systematic literature review update of epidemiological evidence," *Int. J. Public Health*, vol. 64, no. 4, pp. 547–559, May 2019, doi: 10.1007/s00038-019-01202-7.

[43] K. J. Lane *et al.*, "Association of modeled long-term personal exposure to ultrafine particles with inflammatory and coagulation biomarkers," *Environ. Int.*, vol. 92–93, pp. 173–182, Aug. 2016, doi: 10.1016/j.envint.2016.03.013.

[44] B. G. Miller, "8 - Particulate Formation and Control Technologies," in *Clean Coal Engineering Technology (Second Edition)*, B. G. Miller, Ed. Butterworth-Heinemann, 2017, pp. 419–465.

[45] A. Mizuno, "Electrostatic precipitation," *IEEE Trans. Dielectr. Electr. Insul.*, vol. 7, no. 5, pp. 615–624, Oct. 2000, doi: 10.1109/94.879357.

[46] A. Jaworek, A. Marchewicz, A. T. Sobczyk, A. Krupa, and T. Czech, "Two-stage electrostatic precipitators for the reduction of PM2.5 particle emission," *Prog. Energy Combust. Sci.*, vol. 67, pp. 206–233, Jul. 2018, doi: 10.1016/j.pecs.2018.03.003.

[47] A. Zukeran *et al.*, "Two-stage-type electrostatic precipitator re-entrainment phenomena under diesel flue gases," *IEEE Trans. Ind. Appl.*, vol. 35, no. 2, pp. 346–351, Mar. 1999, doi: 10.1109/28.753627.

[48] S. L. Goren, "The instability of an annular thread of fluid," *J. Fluid Mech.*, vol. 12, no. 2, pp. 309–319, Feb. 1962, doi: 10.1017/S002211206200021X.

[49] I. L. Kliakhandler, S. H. Davis, and S. G. Bankoff, "Viscous beads on vertical fibre," *J. Fluid Mech.*, vol. 429, pp. 381–390, 2001.

[50] S. P. Lin and W. C. Liu, "Instability of film coating of wires and tubes," *AIChE J.*, vol. 21, no. 4, pp. 775–782, Jul. 1975, doi: 10.1002/aic.690210420.

[51] R. V. Craster and O. K. Matar, "On viscous beads flowing down a vertical fibre," *J. Fluid Mech.*, vol. 553, pp. 85–105, 2006.

[52] G. D. Wehinger, J. Peeters, S. Muzaferija, T. Eppinger, and M. Kraume, "Numerical simulation of vertical liquid-film wave dynamics," *Chem. Eng. Sci.*, vol. 104, pp. 934–944, Dec. 2013, doi: 10.1016/j.ces.2013.10.027.

[53] J. Grünig, T. Skale, and M. Kraume, "Liquid flow on a vertical wire in a countercurrent gas flow," *Chem. Eng. J.*, vol. 164, no. 1, pp. 121–131, Oct. 2010, doi: 10.1016/j.cej.2010.08.040.

[54] C. Ruyer-Quil and S. Kalliadasis, "Wavy regimes of film flow down a fiber," *Phys. Rev. E*, vol. 85, no. 4, p. 046302, Apr. 2012, doi: 10.1103/PhysRevE.85.046302.

[55] C. Duprat, C. Ruyer-Quil, and F. Giorgiutti-Dauphiné, "Experimental study of the instability of a film flowing down a vertical fiber," *Eur. Phys. J. Spec. Top.*, vol. 166, no. 1, pp. 63–66, Jan. 2009, doi: 10.1140/epjst/e2009-00879-9.

[56] C. Duprat, C. Ruyer-Quil, S. Kalliadasis, and F. Giorgiutti-Dauphiné, "Absolute and Convective Instabilities of a Viscous Film Flowing Down a Vertical Fiber," *Phys. Rev. Lett.*, vol. 98, no. 24, p. 244502, Jun. 2007, doi: 10.1103/PhysRevLett.98.244502.

[57] R. Mead-Hunter, A. J. C. King, and B. J. Mullins, "Plateau Rayleigh Instability Simulation," *Langmuir*, vol. 28, no. 17, pp. 6731–6735, May 2012, doi: 10.1021/la300622h.

[58] J. U. Brackbill, D. B. Kothe, and C. Zemach, “A continuum method for modeling surface tension,” *J. Comput. Phys.*, vol. 100, no. 2, pp. 335–354, Jun. 1992, doi: 10.1016/0021-9991(92)90240-Y.

[59] T. D. Blake, “The physics of moving wetting lines,” *J. Colloid Interface Sci.*, vol. 299, no. 1, pp. 1–13, Jul. 2006, doi: 10.1016/j.jcis.2006.03.051.

[60] C. W. Hirt and B. D. Nichols, “Volume of fluid (VOF) method for the dynamics of free boundaries,” *J. Comput. Phys.*, vol. 39, no. 1, pp. 201–225, Jan. 1981, doi: 10.1016/0021-9991(81)90145-5.

[61] A. Kazemzadeh, P. Ganesan, F. Ibrahim, S. He, and M. J. Madou, “The Effect of Contact Angles and Capillary Dimensions on the Burst Frequency of Super Hydrophilic and Hydrophilic Centrifugal Microfluidic Platforms, a CFD Study,” *PLoS ONE*, vol. 8, no. 9, Sep. 2013, doi: 10.1371/journal.pone.0073002.

[62] L. R. S. R.S, “XVI. On the instability of a cylinder of viscous liquid under capillary force,” *Philos. Mag. Ser. 5*, vol. 34, no. 207, pp. 145–154, Aug. 1892, doi: 10.1080/14786449208620301.

[63] S. Kalliadasis, C. Ruyer-Quil, B. Scheid, and M. G. Velarde, *Falling Liquid Films*. Springer Science & Business Media, 2011.

[64] C. Ruyer-Quil, S. P. M. J. Trevelyan, F. Giorgiutti-Dauphiné, C. Duprat, and S. Kalliadasis, “Film flows down a fiber: Modeling and influence of streamwise viscous diffusion,” *Eur. Phys. J. Spec. Top.*, vol. 166, no. 1, pp. 89–92, Jan. 2009, doi: 10.1140/epjst/e2009-00884-0.

[65] A. Sadeghpour, Z. Zeng, and Y. S. Ju, "Effects of Nozzle Geometry on the Fluid Dynamics of Thin Liquid Films Flowing down Vertical Strings in the Rayleigh–Plateau Regime," *Langmuir*, vol. 33, no. 25, pp. 6292–6299, Jun. 2017, doi: 10.1021/acs.langmuir.7b01277.

[66] "Nonlinear Theory of Strongly Undulating Thin Films Flowing Down Vertical Cylinders - IOPscience." [Online]. Available: https://iopscience.iop.org/article/10.1209/0295-5075/18/7/003. [Accessed: 25-Jan-2020].

[67] H. CHANG and E. DEMEKHIN, "Mechanism for drop formation on a coated vertical fibre," *J. Fluid Mech.*, vol. 380, pp. 233–255, 1999, doi: 10.1017/S0022112098003632.

[68] R. V. Craster and O. K. Matar, "Dynamics and stability of thin liquid films," *Rev. Mod. Phys.*, vol. 81, no. 3, pp. 1131–1198, 2009, doi: 10.1103/RevModPhys.81.1131.

[69] H. Ji, C. Falcon, A. Sadeghpour, Z. Zeng, Y. S. Ju, and A. L. Bertozzi, "Dynamics of thin liquid films on vertical cylindrical fibres," *J. Fluid Mech.*, vol. 865, pp. 303–327, Apr. 2019, doi: 10.1017/jfm.2019.33.

[70] V. Y. Shkadov, "Wave flow regimes of a thin layer of viscous fluid subject to gravity," *Fluid Dyn.*, vol. 2, no. 1, pp. 29–34, Jan. 1967.

[71] A. Münch, B. A. Wagner, and T. P. Witelski, "Lubrication Models with Small to Large Slip Lengths," *J. Eng. Math.*, vol. 53, no. 3, pp. 359–383, Dec. 2005.

[72] S. Haefner *et al.*, "Influence of slip on the Plateau–Rayleigh instability on a fibre," *Nat. Commun.*, vol. 6, no. 1, p. 7409, Jun. 2015, doi: 10.1038/ncomms8409.

[73] D. Halpern and H.-H. Wei, "Slip-enhanced drop formation in a liquid falling down a vertical fibre," *J. Fluid Mech.*, vol. 820, pp. 42–60, 2017, doi: 10.1017/jfm.2017.202.

[74] B. Reisfeld and S. G. Bankoff, "Non-isothermal flow of a liquid film on a horizontal cylinder," *J. Fluid Mech.*, vol. 236, pp. 167–196, 1992, doi: 10.1017/S0022112092001381.

[75] S. Parekh, M. M. Farid, J. R. Selman, and S. Al-Hallaj, "Solar desalination with a humidification-dehumidification technique—a comprehensive technical review," *Desalination*, vol. 160, no. 2, pp. 167–186, 2004.

[76] G. Prakash Narayan, J. H. Lienhard, and S. M. Zubair, "Entropy generation minimization of combined heat and mass transfer devices," *Int. J. Therm. Sci.*, vol. 49, no. 10, pp. 2057–2066, Oct. 2010, doi: 10.1016/j.ijthermalsci.2010.04.024.

[77] G. Prakash Narayan, M. G. St. John, S. M. Zubair, and J. H. Lienhard V, "Thermal design of the humidification dehumidification desalination system: An experimental investigation," *Int. J. Heat Mass Transf.*, vol. 58, no. 1–2, pp. 740–748, Mar. 2013, doi: 10.1016/j.ijheatmasstransfer.2012.11.035.

[78] K. M. Chehayeb, G. P. Narayan, S. M. Zubair, and J. H. Lienhard V, "Thermodynamic balancing of a fixed-size two-stage humidification dehumidification desalination system," *Desalination*, vol. 369, pp. 125–139, Aug. 2015, doi: 10.1016/j.desal.2015.04.021.

[79] K. M. Chehayeb, G. Prakash Narayan, S. M. Zubair, and J. H. Lienhard V, "Use of multiple extractions and injections to thermodynamically balance the humidification dehumidification desalination system," *Int. J. Heat Mass Transf.*, vol. 68, pp. 422–434, Jan. 2014, doi: 10.1016/j.ijheatmasstransfer.2013.09.025.

[80] W. M. Rohsenow and J. P. (eds) Hartnett, "Handbook of heat transfer," McGraw-Hill Book Company, New York, Jan. 1973.

[81] J. Huang, J. Zhang, and L. Wang, "Review of vapor condensation heat and mass transfer in the presence of non-condensable gas," *Appl. Therm. Eng.*, vol. 89, pp. 469–484, Oct. 2015, doi: 10.1016/j.applthermaleng.2015.06.040.

[82] T. D. Karapantsios and A. J. Karabelas, “Direct-contact condensation in the presence of noncondensables over free-falling films with intermittent liquid feed,” *Int. J. Heat Mass Transf.*, vol. 38, no. 5, pp. 795–805, Mar. 1995, doi: 10.1016/0017-9310(94)00214-G.

[83] M. K. Bologa, I. K. Savin, and A. B. Didkovsky, “Electric-field-induced enhancement of vapour condensation heat transfer in the presence of a non-condensable gas,” *Int. J. Heat Mass Transf.*, vol. 30, no. 8, pp. 1577–1585, Aug. 1987, doi: 10.1016/0017-9310(87)90302-4.

[84] G. P. Narayan, M. H. Sharqawy, S. Lam, S. K. Das, and J. H. Lienhard, “Bubble columns for condensation at high concentrations of noncondensable gas: Heat-transfer model and experiments,” *AIChE J.*, vol. 59, no. 5, pp. 1780–1790, May 2013, doi: 10.1002/aic.13944.

[85] Z. Zeng, A. Sadeghpour, and Y. S. Ju, “A highly effective multi-string humidifier with a low gas stream pressure drop for desalination,” *Desalination*, vol. 449, pp. 92–100, Jan. 2019, doi: 10.1016/j.desal.2018.10.017.

[86] C. Duprat, D. Tseluiko, S. Saprykin, S. Kalliadasis, and F. Giorgiutti-Dauphiné, “Wave interactions on a viscous film coating a vertical fibre: Formation of bound states,” *Chem. Eng. Process. Process Intensif.*, vol. 50, no. 5–6, pp. 519–524, May 2011, doi: 10.1016/j.cep.2010.10.004.

[87] M. J. Miksis and S. H. Davis, “Slip over rough and coated surfaces,” *J. Fluid Mech.*, vol. 273, pp. 125–139, Aug. 1994, doi: 10.1017/S0022112094001874.

[88] F. J. Solorio and M. Sen, “Linear stability of a cylindrical falling film,” *J. Fluid Mech.*, vol. 183, pp. 365–377, Oct. 1987, doi: 10.1017/S0022112087002672.

[89] S. Whitaker, "Forced convection heat transfer correlations for flow in pipes, past flat plates, single cylinders, single spheres, and for flow in packed beds and tube bundles.," *AIChE J.*, vol. 18, pp. 361–371, 1972.

[90] A. Mills, *Heat and Mass Transfer*. CRC Press, 1995.

[91] K.-C. Park *et al.*, "Condensation on slippery asymmetric bumps," *Nature*, vol. 531, no. 7592, p. 78, 2016.

[92] E. M. Sparrow and A. L. Loeffler, "Longitudinal laminar flow between cylinders arranged in regular array," *AIChE J.*, vol. 5, no. 3, pp. 325–330, Sep. 1959, doi: 10.1002/aic.690050315.

[93] K. Rehme, "Pressure drop performance of rod bundles in hexagonal arrangements," *Int. J. Heat Mass Transf.*, vol. 15, no. 12, pp. 2499–2517, 1972.

[94] K. Rehme and G. Trippe, "Pressure drop and velocity distribution in rod bundles with spacer grids," *Nucl. Eng. Des.*, vol. 62, no. 1–3, pp. 349–359, 1980.

[95] M. Sievers and J. H. L. V, "Design of Flat-Plate Dehumidifiers for Humidification–Dehumidification Desalination Systems," *Heat Transf. Eng.*, vol. 34, no. 7, pp. 543–561, Jan. 2013, doi: 10.1080/01457632.2013.730355.

[96] E. W. Tow and J. H. Lienhard V, "Experiments and modeling of bubble column dehumidifier performance," *Int. J. Therm. Sci.*, vol. 80, pp. 65–75, Jun. 2014, doi: 10.1016/j.ijthermalsci.2014.01.018.

[97] M. M. Farid, S. Parekh, J. R. Selman, and S. Al-Hallaj, "Solar desalination with a humidification-dehumidification cycle: mathematical modeling of the unit," *Desalination*, vol. 151, no. 2, pp. 153–164, Jan. 2003, doi: 10.1016/S0011-9164(02)00994-3.

[98] Z. Chang, H. Zheng, Y. Yang, Y. Su, and Z. Duan, "Experimental investigation of a novel multi-effect solar desalination system based on humidification–dehumidification process," *Renew. Energy*, vol. 69, pp. 253–259, Sep. 2014, doi: 10.1016/j.renene.2014.03.048.

[99] D. M. Warsinger, K. H. Mistry, K. G. Nayar, H. W. Chung, and J. H. Lienhard V, "Entropy Generation of Desalination Powered by Variable Temperature Waste Heat," *Entropy*, vol. 17, no. 11, pp. 7530–7566, Oct. 2015, doi: 10.3390/e17117530.

[100] G. P. Narayan, K. H. Mistry, M. H. Sharqawy, S. M. Zubair, and J. H. Lienhard, "Energy effectiveness of simultaneous heat and mass exchange devices," *Glob. Digit. Cent.*, 2010.

[101] A. Wexler and R. W. Hyland, "Formulations for the Thermodynamic Properties of Dry Air from 173.15 K to 473.15 K, and of Saturated Moist Air from 173.15 K to 372.15 K, at Pressures to 5 MPa," *Final Rep. ASHRAE Proj. RP216*, 1980.

[102] D. J. Bayless, M. K. Alam, R. Radcliff, and J. Caine, "Membrane-based wet electrostatic precipitation," *Fuel Process. Technol.*, vol. 85, no. 6, pp. 781–798, Jun. 2004, doi: 10.1016/j.fuproc.2003.11.025.

[103] H. Pasic, M. K. Alam, and D. J. Bayless, "Membrane electrostatic precipitator," US6231643B1, 15-May-2001.

[104] H. Pasic, J. Caine, and H. Shah, "MWESP: Membrane tubular wet electrostatic precipitators," *Filtr. Sep.*, vol. 43, no. 9, pp. 16–18, Nov. 2006, doi: 10.1016/S0015-1882(06)71003-5.

[105] C. Huang, X. Ma, M. Wang, Y. Sun, C. Zhang, and H. Tong, "Property of the PVC Dust Collecting Plate Used in Wet Membrane Electrostatic Precipitator," *IEEE Trans. Plasma Sci.*, vol. 42, no. 11, pp. 3520–3528, Nov. 2014, doi: 10.1109/TPS.2014.2359973.

[106] M. Ali *et al.*, "Experimental study of cross-flow wet electrostatic precipitator," *J. Air Waste Manag. Assoc. 1995*, vol. 66, no. 12, pp. 1237–1244, 2016, doi: 10.1080/10962247.2016.1209258.

[107] P. Saiyasitpanich, T. C. Keener, M. Lu, S.-J. Khang, and D. E. Evans, "Collection of Ultrafine Diesel Particulate Matter (DPM) in Cylindrical Single-Stage Wet Electrostatic Precipitators," *Environ. Sci. Technol.*, vol. 40, no. 24, pp. 7890–7895, Dec. 2006, doi: 10.1021/es060887k.

[108] A. Sadeghpour, Z. Zeng, H. Ji, N. D. Ebrahimi, A. L. Bertozzi, and Y. S. Ju, "Water vapor capturing using an array of traveling liquid beads for desalination and water treatment," *Sci. Adv.*, vol. 5, no. 4, p. eaav7662, Apr. 2019, doi: 10.1126/sciadv.aav7662.

[109] P. A. Lawless, "Particle charging bounds, symmetry relations, and an analytic charging rate model for the continuum regime," *J. Aerosol Sci.*, vol. 27, no. 2, pp. 191–215, Mar. 1996, doi: 10.1016/0021-8502(95)00541-2.

[110] B. Y. H. Liu and A. Kapadia, "Combined field and diffusion charging of aerosol particles in the continuum regime," *J. Aerosol Sci.*, vol. 9, no. 3, pp. 227–242, Jan. 1978, doi: 10.1016/0021-8502(78)90045-9.

[111] B. Y. H. Liu and H. Yeh, "On the Theory of Charging of Aerosol Particles in an Electric Field," *J. Appl. Phys.*, vol. 39, no. 3, pp. 1396–1402, Feb. 1968, doi: 10.1063/1.1656368.

[112] H. Bai, C. Lu, and C. L. Chang, "A Model to Predict the System Performance of an Electrostatic Precipitator for Collecting Polydisperse Particles," *J. Air Waste Manag. Assoc.*, vol. 45, no. 11, pp. 908–916, Nov. 1995, doi: 10.1080/10473289.1995.10467423.

[113] J.-H. Park and C.-H. Chun, "An improved modelling for prediction of grade efficiency of electrostatic precipitators with negative corona," *J. Aerosol Sci.*, vol. 33, no. 4, pp. 673–694, Apr. 2002, doi: 10.1016/S0021-8502(01)00205-1.

[114] R. L. Cochet, "Charge des Fines Particules (Submicroniques) Etudes The´oretiques-Controles Re´cents Spectre de Particules," *J. Aerosol Sci.*, no. 102, pp. 331–338, 1961.

[115] C. Riehle and F. Löfer, "Grade efficiency and Eddy diffusivity models," *J. Electrost.*, vol. 34, no. 4, pp. 401–413, May 1995, doi: 10.1016/0304-3886(94)00024-Q.

[116] P. Cooperman, "A new theory of precipitator efficiency," *Atmospheric Environ. 1967*, vol. 5, no. 7, pp. 541–551, Jul. 1971, doi: 10.1016/0004-6981(71)90064-3.

[117] Z. Zhibin and Z. Guoquan, "Investigations of the Collection Efficiency of an Electrostatic Precipitator with Turbulent Effects," *Aerosol Sci. Technol.*, vol. 20, no. 2, pp. 169–176, Jan. 1994, doi: 10.1080/02786829408959674.

[118] W. Deutsch, "Bewegung und Ladung der Elektrizitätsträger im Zylinderkondensator," *Ann. Phys.*, vol. 373, no. 12, pp. 335–344, 1922, doi: 10.1002/andp.19223731203.

[119] R. C. Flagan and J. H. Seinfeld, *Fundamentals of air pollution engineering*. Englewood Cliffs, New Jersey: Prentice-Hall, Inc., 1988.

[120] "COMSOL Multiphysics® Modeling Software." [Online]. Available: https://www.comsol.com/. [Accessed: 10-Jan-2020].

[121] N. E. Jewell-Larsen, S. V. Karpov, I. A. Krichtafovitch, V. Jayanty, C.-P. Hsu, and A. V. Mamishev, "Modeling of corona-induced electrohydrodynamic flow with COMSOL multiphysics," in *Proceedings ESA Annual Meeting on Electrostatics, Minneapolis, Minnesota*, 2008, pp. 17–19.

[122] K. Adamiak, "Numerical models in simulating wire-plate electrostatic precipitators: A review," *J. Electrost.*, vol. 71, no. 4, pp. 673–680, Aug. 2013, doi: 10.1016/j.elstat.2013.03.001.

[123] Q. Liu, S. Zhang, and J. Chen, "Numerical analysis of charged particle collection in wire-plate ESP," *J. Electrost.*, vol. 74, pp. 56–65, Apr. 2015, doi: 10.1016/j.elstat.2014.11.007.

[124] F. Kherbouche, Y. Benmimoun, A. Tilmatine, A. Zouaghi, and N. Zouzou, "Study of a new electrostatic precipitator with asymmetrical wire-to-cylinder configuration for cement particles collection," *J. Electrost.*, vol. 83, pp. 7–15, Oct. 2016, doi: 10.1016/j.elstat.2016.07.001.

[125] K. R. Parker, Ed., *Applied Electrostatic Precipitation*. Springer Netherlands, 1997.

[126] A. Haider and O. Levenspiel, "Drag coefficient and terminal velocity of spherical and nonspherical particles," *Powder Technol.*, vol. 58, no. 1, pp. 63–70, May 1989, doi: 10.1016/0032-5910(89)80008-7.

[127] S. A. Morsi and A. J. Alexander, "An investigation of particle trajectories in two-phase flow systems," *J. Fluid Mech.*, vol. 55, no. 2, pp. 193–208, Sep. 1972, doi: 10.1017/S0022112072001806.

[128] M. J. Pilat, "Collection of Aerosol Particles by Electrostatic Droplet Spray Scrubbers," *J. Air Pollut. Control Assoc.*, vol. 25, no. 2, pp. 176–178, Feb. 1975, doi: 10.1080/00022470.1975.10470070.

[129] H.-J. Kim *et al.*, "Fine particle removal performance of a two-stage wet electrostatic precipitator using a nonmetallic pre-charger," *J. Air Waste Manag. Assoc. 1995*, vol. 61, no. 12, pp. 1334–1343, Dec. 2011, doi: 10.1080/10473289.2011.603994.

[130] H.-G. Kim, H.-J. Kim, M.-H. Lee, and J.-H. Kim, "Experimental Study on the Enhancement of Particle Removal Efficiency in Spray Tower Scrubber Using Electrospray," *Asian J. Atmospheric Environ.*, vol. 8, no. 2, pp. 89–95, 2014, doi: 10.5572/ajae.2014.8.2.089.

[131] L. Su *et al.*, "Purification characteristics of fine particulate matter treated by a self-flushing wet electrostatic precipitator equipped with a flexible electrode," *J. Air Waste Manag. Assoc. 1995*, vol. 68, no. 7, pp. 725–736, 2018, doi: 10.1080/10962247.2018.1460635.

[132] K. H. Yoo, J. S. Lee, and M. D. Oh, "Charging and Collection of Submicron Particles in Two-Stage Parallel-Plate Electrostatic Precipitators," *Aerosol Sci. Technol.*, vol. 27, no. 3, pp. 308–323, Sep. 1997, doi: 10.1080/02786829708965476.

[133] M. Li and P. D. Christofides, "Collection Efficiency of Nanosize Particles in a Two-Stage Electrostatic Precipitator," *Ind. Eng. Chem. Res.*, vol. 45, no. 25, pp. 8484–8491, Dec. 2006, doi: 10.1021/ie060101r.

[134] Y. Zhuang, Y. Jin Kim, T. Gyu Lee, and P. Biswas, "Experimental and theoretical studies of ultra-fine particle behavior in electrostatic precipitators," *J. Electrost.*, vol. 48, no. 3, pp. 245–260, Mar. 2000, doi: 10.1016/S0304-3886(99)00072-8.

[135] S.-H. Huang and C.-C. Chen, "Ultrafine Aerosol Penetration through Electrostatic Precipitators," *Environ. Sci. Technol.*, vol. 36, no. 21, pp. 4625–4632, Nov. 2002, doi: 10.1021/es011157+.

[136] M. Adachi, Y. Kousaka, and K. Okuyama, "Unipolar and bipolar diffusion charging of ultrafine aerosol particles," *J. Aerosol Sci.*, vol. 16, no. 2, pp. 109–123, Jan. 1985, doi: 10.1016/0021-8502(85)90079-5.